2012

Design of a vortex induced vibration based marine hydro-kinetic energy system

Varun Michael Lobo

Department:

DESIGN OF A VORTEX INDUCED VIBRATION BASED MARINE HYDRO – KINETIC ENERGY SYSTEM

by

VARUN MICHAEL LOBO

A THESIS

Presented to the Faculty of the Graduate School of the

Missouri University of Science and Technology

In partial Fulfillment of the Requirements for the Degree

MASTER OF SCIENCE IN MECHANICAL ENGINEERING

2012

Approved by

Arindam Banerjee, Advisor
Jonathan Kimball
K.Chandrashekhara

ABSTRACT

Hydrokinetic energy harvesting based on vortex induced vibration (VIV) of a bluff body is discussed. VIV is defined as the vibration incurred on a bluff body due to an external fluid flowing over it. These vibrations are the results of boundary layer separation from the surface of the body. An optimized VIV generator has been developed, that utilizes a non-contact type linear magnetic device for generation of energy. The cylinder was chosen such that at the mass ratio (m^*) was always lower than the critical mass ($m^*_{critical} = 0.52$). The studies were based on two complementary techniques: (a) computational fluid dynamics study to derive the initial design guidelines of our laboratory prototype; and, (b) experimental study to identify optimized design parameters that would allow such a device to maximize the net energy production.

A detailed two-dimensional CFD study was performed at laminar and turbulent flow regimes ($45 < Re < 3.2\times10^4$). A k-ω Shear Stress Transport turbulence model was chosen in the present study. The results obtained from the laminar flow ($Re < 200$) suggest a maximum attainable amplitude of ~0.6D.The maximum amplitude was found to be a constant even for the case where the overall mass damping of the system was reduced to zero. Also as seen in experiments, the present numerical study depicted an absence of the upper branch at low values of Reynolds number. For the turbulent flow case ($1\times10^4 < Re < 3.2\times10^4$), our numerical simulations accurately predicts the appearance of the 2S mode in the initial branch followed by a 2P mode in the upper and lower branches. However, at higher Re, the flow is expected to become three-dimensional (as observed in experiments) and our two-dimensional simulations were unable to predict the amplitudes in the upper branch that were obtained from experiments done in-house. The effect of mass ratio on VIV was studied experimentally for seven different cylinders with varying diameters having mass ratios (m^*) from 10.75 to 0.47. Regimes of operation that would maximize the energy harvested from our VIV based generated are identified. Finally, a power take-off system (PTO) based on a Tubular Linear Interior Permanent Magnet (TL-IPM) is proposed and various preliminary design parameters for such a system is discussed.

ACKNOWLEDGMENTS

I would like to express my sincere appreciation and deep-felt gratitude to my advisor Prof. Arindam Banerjee who has always patiently guided me throughout this project. He has always been a great source of help and motivation for my work. Without his invaluable suggestions, encouragement and financial support this project would have never been possible. I wish to express my sincere gratitude to my committee member- Prof. Jonathan Kimball for his constant help and guidance about various issues with the power-take-off unit. The discussions with Dr. Kimball and Brad during our bi-weekly meetings have helped me tremendously to understand the engineering approach of integrating the mechanical and electrical sub-systems. I am also grateful to Prof. K. Chandrashekhara for his valuable guidance during the project. Special thanks to Prof. Mariesa Crow (ECE) for providing us with a seed grant from the Energy Research and Development Center (ERDC).

I would also like to thank the Senior Laboratory Mechanic Robert (Bob) Hribar and George Green with all the help I needed with the fabrication of my experiment. Most importantly I would like to thank my fellow lab members: Pam, Aaron, Tim, Mohammed, Taylor, Raghu, Suchi, Nitin, Rahul and Ashwin for all the help and also for always being a great source of inspiration. Special thanks to Cajon with who I have always had fruitful discussions about my research. I would especially like to thank my friends Pam, Sachin, Shreya, Ketan and everyone else in Rolla for all their love and constant support. Special thanks to the IT helpdesk especially Connie and her team of IT experts. I would also like to acknowledge the help of Kathy Wagner and Cathy Williams with the immense secretarial help they have provided me with during my M.S. program.

I am deeply and forever indebted to my Dad, Mom, Brother, Sister-in-law and all my relatives and friends back home (in India) for their love, support and encouragement throughout my life; without them this would have never been possible.

TABLE OF CONTENTS

Page

LIST OF ILLUSTRATIONS

Page

LIST OF TABLES

Page

1. INTRODUCTION

1.1 NEED FOR RENEWABLE ENERGY

In recent times, many scientific studies [1, 2] have pointed out to the effects of global warming and climate changes caused by the greenhouse gasses, there is an increasing need for environmentally friendly, low cost renewable energy technology to help reduce these emissions resulting from fossil fuel consumption. At present, 72% of the total amount of usable energy is obtained by coal, oil and natural gas respectively [3]. With only 4.7% of the world's population, the United States itself consumed approximately 25% of the total fossil fuel used each year at an annual cost of $65 billion [4]. A recent study estimated [5], the current fossil fuel reserves to be depleted by 2042, presented an urgent need to develop and validate an alternate form of energy which has low life cycle cost and as a result is environmentally friendly. The challenge of meeting the demands of fossil fuels due to its heavy consumption has now been the focus of many large corporations, state and federal governments as well as federal research agencies. The three commonly known resources of alternate energy are solar, wind and biomass. According to the power projections by Annual Energy Outlook 2011 [6] early release overview, the primary energy production from hydropower, biomass and other renewable energy sources accounts for 15.2 (quadrillion Btu) in the year 2035 which shows promising contribution to the energy needs of the future. But however, according to the Annual Energy Outlook 2011 [3], the total US energy consumption was 94.6 quadrillion Btu out of which only 8% was based on renewable energy. As shown in Figure 1.1, fuels obtained from fossils e.g. petroleum, coal and natural gas accounted for a total of 83% of the total energy usage [3]. Even though petroleum (37%) and coal (21%) remain the main source of power supply in the United States, the projections over the next 24 years show an increase in the usage of renewable energy to ~ 10% (see Figure 1.2). However, total coal consumption, which was 22.7 quadrillion Btu in 2007, increases from 19.7 quadrillion Btu (1,000 million short tons) in 2009 to 25.2 quadrillion Btu (1,302 million short tons) in 2035 [3]. Also the total net generation in 2009 was 3,953 billion kWh out of which ~ 70% of energy is obtained from fossil based fuels. This shows huge dependency on fossil reserves for our energy need. According to Electric Power Research

Institute (EPRI), wave and current energy in the US have the potential to meet nearly 10% of the national demand which estimates to nearly 55GW of renewable energy in US by the year 2020 [7]. Although there is a rapid growth of renewable energy, fossil fuel would still provide 78% of the U.S energy use in 2035. Hence to further decrease the dependence on fossil fuels, new and improved technologies have to be introduced to augment the present technologies so that the energy needs of the future are met without excess dependence on fossil fuels. Figure 1.1 shows the present U.S Energy supply, while Figure 1.2 shows the future U.S primary energy consumption.

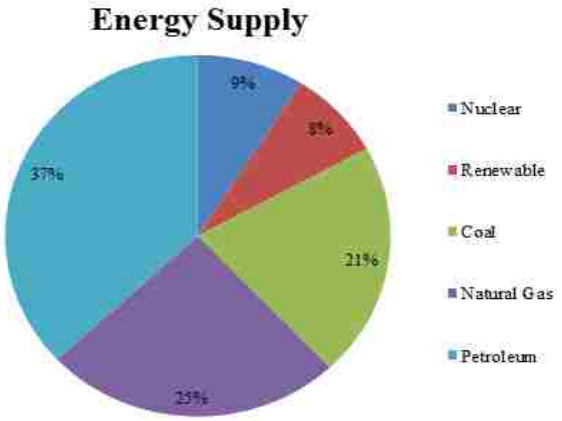

Figure 1.1. Current U.S energy supply [3]

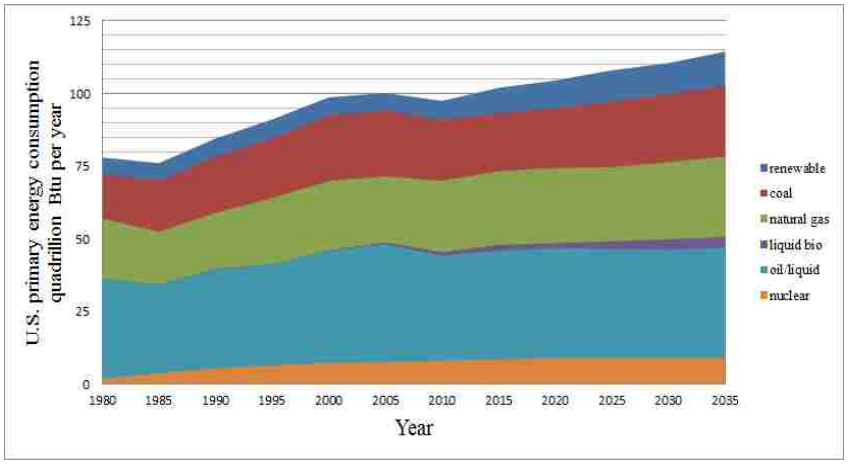

Figure 1.2. U.S. primary energy consumption [3]

1.2 AN INTRODUCTION TO MARINE HYDROKINETIC ENERGY SYSTEMS

Energy harnessed from the kinetic energy of flowing water is called as hydrokinetic energy and the device used to extract it is called as a hydro-kinetic generator. It is an important form of renewable energy abundantly available in nature. Power from rivers, oceans and streams provides around ~ 70% of the renewable energy in the United States [3]. It has the potential to generate ~ 2 GW of energy with minimal impact on the climate [8]. Currently water is a leading renewable energy source used to generate electric power, however there are many advantages and disadvantages associated with the generation of power from traditional hydro energy sources like dams. The main advantage is that power obtain from dams is low cost in addition to no pollution, but like all other power plants, power generated from water has its own set of limitations also. The dams built for these purpose can significantly affect the lives of the eco system thriving there. Furthermore, the construction of huge dams/reservoirs and power grids have substantial environmental impact. Due to the serious challenges faced in obtaining power from dams and reservoirs, the focus has now shifted to the exploitation of various marine and hydro-kinetic systems, which possesses various operational, economic and environmental advantages as compared to building of a dam or a reservoir. New technologies are now being constantly developed to overcome the disadvantages associated with the energy obtained from the traditional dams and reservoirs. These new technologies use either the waves at the surface or the currents in flowing water sources like the rivers, rather than storing or blocking the flow of water like in dams to generate energy. They can be categorized as marine systems and hydrokinetic systems. A marine system utilizes the wave motion at the surface to harness energy while a hydro kinetic system utilizes the kinetic energy from flowing water to harness energy. A few examples of marine systems for energy generation are the Pelamis, OPT power buoy, oscillating water column etc while marine current turbines (MCT), the VIVACE (Vortex Induced Vibrations Aquatic Clean Energy) etc are examples of hydrokinetic systems. The marine systems and the hydrokinetic systems can be further classified as rotary and non-rotary type. The following is a brief description on the working of marine and hydrokinetic energy harvesting systems.

1.3 MARINE SYSTEMS

Depending on the type of operation, the marine systems are further classified as rotary and non-rotary types. A marine system utilizes the motion of the waves to generate energy. The following is a brief description of various types of marine systems

- **Oscillating water column (OWC).** This is a partially submerged body which contains air in an air chamber. As the waves enter and exit the system, the air in the air chamber gets compressed and decompressed by the motion of the waves. This air acts like a piston and is pushed through a high velocity exit blow hole connected to a turbine. This turbine is connected to an electric generator to produce electricity. An oscillating water column is shown in Figure 1.3

Figure 1.3. Energytech's Oscillating Water Column [9]

- **Overtopping device.** This type of energy generator shown in Figure 1.4 is like a floating reservoir which gets filled up when the waves break over the walls of the device. This reservoir creates a head and water is allowed to pass through the turbine to generate energy. The water in the reservoir is at a head above the surface of the water. This head creates sufficient pressure to drive the hydro turbine as the water flows back into the ocean. Figure 1.4 shows the schematic of a overtopping device.

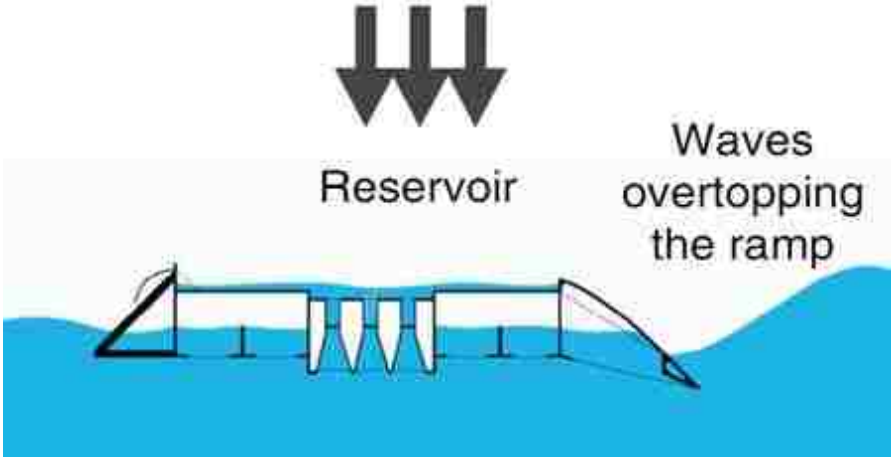

Figure 1.4. An overtopping wave energy converter [10]

- **Pelamis.** The pelamis is a semi-submerged wave energy converter technology (see Figure 1.5 and 1.6) that uses the motion of the waves on the surface of the ocean to produce energy and consists of three power modules joined together by tubular parts/sections. The waves cause relative motion between the modules and the tubular section of the pelamis. The power modules consist of hydraulic rams that push the high pressure oil through hydraulic motors. The hydraulic motors are then used to drive the electrical generators to produce electricity. Figure 1.5 and 1.6 shows the schematic which highlights the working principle of the pelamis wave energy converter. *Pelamis wave power (PWP),* established in 1998 designs and manufactures the pelamis wave energy converter. PWP's full scale prototype machine was tested at the European Marine Energy Centre between 2004 and 2007 and was the world's first commercial scale wave energy converter to generate electricity to a national grid from offshore waves [11]. It is know that under good wave resource, the pelamis will have an energy payback period of less than 20 months [11]. Under these conditions a Pelamis machine will offset the production of approximately 2,000 tons of *CO2* from a conventional combined cycle gas power station each year [11].

Figure 1.5. Pelamis, the floating wave energy extractor [11]

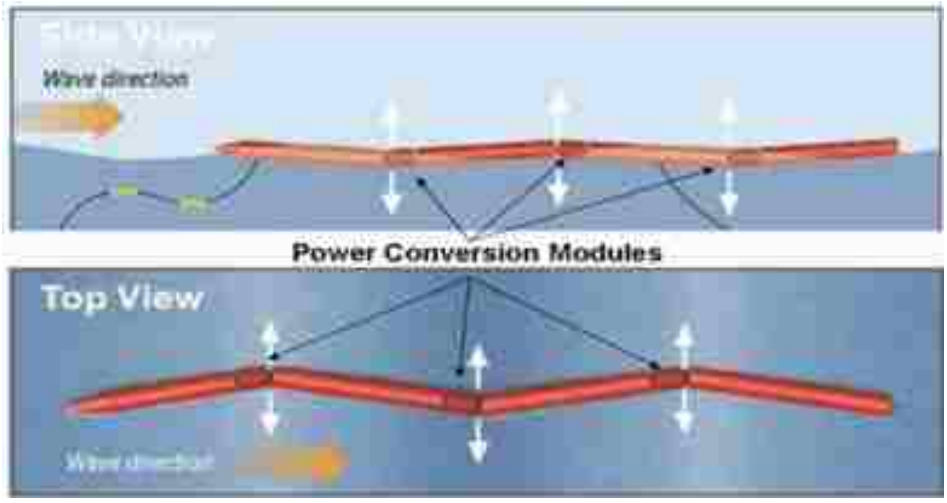

Figure 1.6. Schematic figure of the Pelamis wave energy converter [11]

- **OPT's PowerBuoy.** The PowerBuoy designed by Ocean Power Technologies (OPT's) is also a power generator that extracts the energy from the ocean waves (see Figure 1.7 (a). It is a wave energy generator that is submerged more than a meter below the water's surface, the rising and falling of the waves off shore causes the buoy to move freely up and down. The harvester consists of a piston like structure that moves linearly with the waves. This movement drives the generator that is situated at the ocean bed to produce electricity, which is then sent to the shores by underwater cables (see Figure 1.7

(b)). The total operating cost of generating power from an OPT wave power station is projected to be only (US) 3-4¢/ kWh for 100MW systems and (US) 7-10¢/kWh for 1MW plants, including maintenance and operating expenses, as well as the capital cost of the equipment [12]. It is estimated that a 10-MW OPT power station would occupy only approximately 30 acres (0.125 square kilometers) of ocean space [12].

Compact and modular in design, the PowerBuoy (Model-PB40) is less than 12 feet in diameter and 55 feet long. It is based on OPT's proprietary design which is primarily below the sea surface when deployed, with minimal visual impact. The PowerBuoy was deployed on 2009 approximately three-quarters of a mile off the coast of Oahu, Hawaii at a water depth of 100 feet. To date, the PowerBuoy has operated and produced power from over 4.8 million power take-off cycles and 7,350 hours of operation [12].

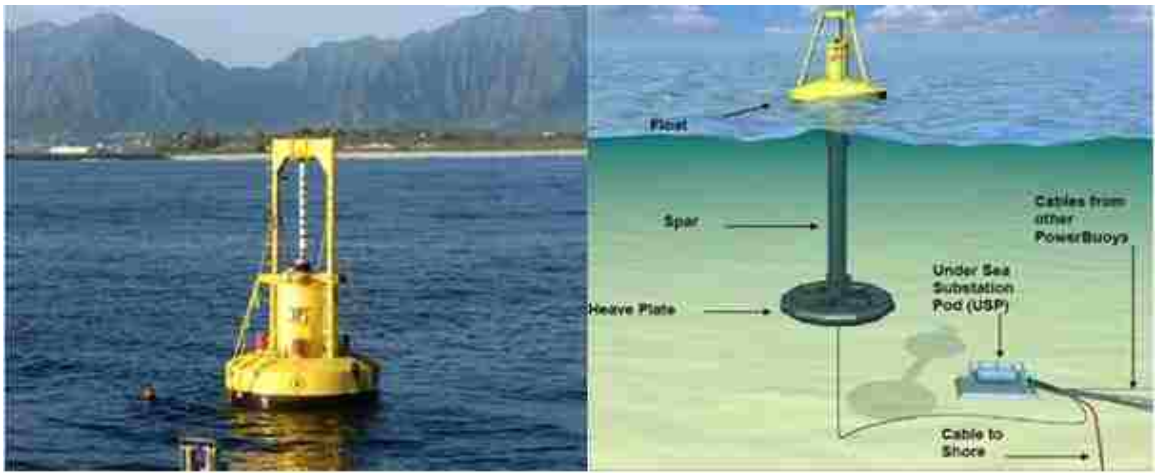

Figure 1.7. OPT's PowerBuoy (a) OPT's PowerBuoy deployed in the ocean (b) Schematic diagram of a PowerBuoy [12]

- **Point Absorber.** This is a bottom mounted floating device which has the capability to absorb power in all direction. The power taking device position may depend upon the configuration of the displacers. The following figure shows a buoy floating at the top. This floating buoy is set into vertical displacements due to the motion of the wave. This vertical displacement is converted into power using a generator connected at

the base. The power is then transmitted to the shores through underground cables as seen in the Figure 1.8

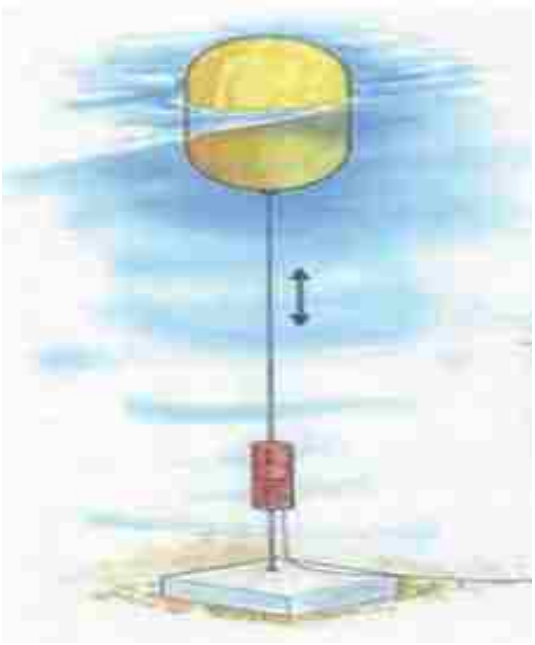

Figure 1.8. Floating Buoy point absorber [10]

- **Floating wave energy extractor.** It consists of a huge mass body connected to large number of piston shafts. This huge mass body is floated on these air columns that are provided on the bottom of the supporting piston shafts. The entire system is anchored to the sea bed. It consists of two openings at the top of the cylinder/air column. One leads to a high-pressure pipe while the other one to a low pressure pipe. When the piston is pushed up by the crest of a wave, the high pressure fluid is pushed to the turbine. As the turbines rotate, the generator coupled to a turbine generates electricity. During trough period, there is low pressure being created in the cylinder due to suction. Due to this, the low pressure fluid from the turbine enters the cylinder or air column to be ready for the next compression cycle. Figure 1.9 show the oscillating water column and the floating wave energy extractor [13].

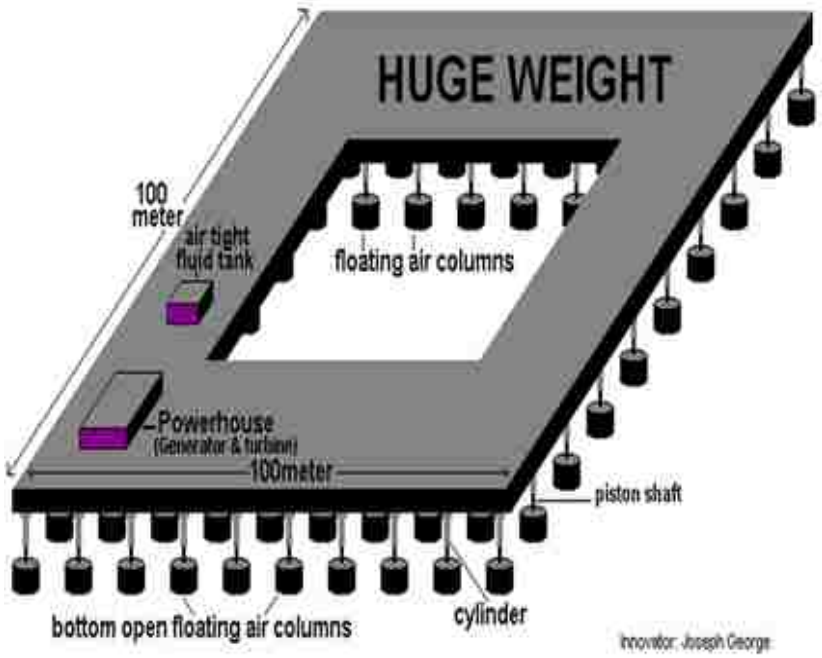

Figure 1.9. Floating wave energy extractor [13]

1.4 HYDROKINETIC SYSTEMS. Systems that utilize the kinetic energy from flowing waters to generate energy are called as hydrokinetic systems. Like marine systems hydrokinetic systems are also classified as rotary and non-rotary type. The examples of rotary type hydrokinetic systems would be the Rotech tidal turbine (RTT), Marine current turbine (MCT) etc while VIVACE (Vortex Induced Vibration Aquatic Clean Energy) is an example of non-rotary type hydrokinetic system. A brief description of each type of hydrokinetic system is mentioned below.

- **Rotech tidal turbine.** These are renewable energy generating device which is positioned at the bed of the ocean thus being unobtrusive, environmental friendly and invisible from the coast. It is a device that uses the Rotech Tidal Turbine (RTT) technology to produces low cost electricity by harnessing tidal power from the earth's tidal system. The RTT is a bi-directional horizontal axis turbine housed in a symmetrical venturi duct. The duct is used to accelerate the fluid towards the rotor even if the flow is at an angle with the axis of the turbine. Thus the flow is always perpendicular to the blades, maximizing its efficiency. This duct draws the existing ocean currents into the RTT in order to capture and convert energy into electricity. It consisted of gravity ducts

which allow the generator to be deployed easily on the ocean bed without extensive sea bed preparation. Figure 1.10 shows a schematic of the lunar power turbine.

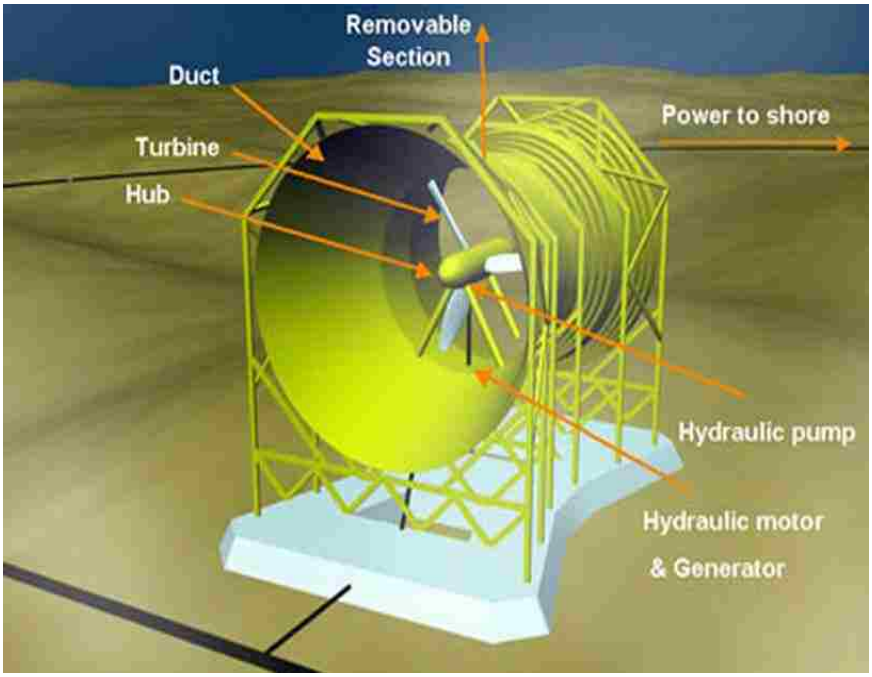

Figure 1.10. Lunar energy, Rotech Tidal turbine [14]

- **Horizontal axis turbine.** Verdant power uses a three blade horizontal-axis turbine to convert the K.E of flowing rivers into useful electrical energy. This system is installed completely submerged under water. They are similar in design to wind turbines, modular in design and scalable and can be designed and scaled to produce cost effective system. Also with fewer moving parts, the operation and maintenance cost is lowered considerably. The first project was initiated in 2002 in New York City's East River and consisted of 3 stages, prototype testing, demonstration and MW-scale build-out. This Project demonstration system stands as the world's first grid-connected array of tidal turbines. Figure 1.11 shows a verdant horizontal axis turbine.

Figure 1.11. Three blade horizontal axis turbine by Verdant Power [15]

- **Seagen.** The tidal turbines that are manufactured by Marine Current Turbines (MCT) are very much similar to windmills but submerged in water. These turbines are run with the help of tidal currents rather than wind. The commercial system of MCT called as *SeaGen* has the capability to generate 10MWh per tide [16]. SeaGen uses the axial flow pitch controlled rotors which is widely used in the wind farm industry. The efficiency achieved by the rotors of SeaGen is over 48%. Currently the prototype is operational in Strangford Narrows, Northern Ireland and has the capability to develop 1.2MW of power at 2.4m/s. A S*eaGen* twin rotor turbine is shown in Figure 1.12

Figure 1.12. ‘Seagen” twin rotor turbine in Strangford Lough [17]

- **VIVACE.** VIVACE (Vortex Induced Vibration Aquatic Clean Energy) is a linear hydro energy generator based on the concept of vortex shedding from the surface of a cylinder. This generator derives the energy from the alternate vortex that is shed from bluff bodies. Leonardo da Vinci was the first to notice vibrations due to vortex shedding which was then called the 'Aeolian Tones'. Over a period of years, it has been known that vortex shedding from the surface can cause catastrophic damage to civil structures and buildings. "The VIVACE converter design is based on the very simple idea of enhancing rather than spoiling vortex shedding and maximizing under significant damping rather than suppressing vortex induced vibrations" [18]. This vortex to energy converter was invented by Bernitsas and Raghavan and patented through the University of Michigan [19, 20]. Figure 1.13 is a schematic diagram of the VIVACE generator with multiple cylinder arrangement. The system mainly consists of a cylinder, springs and electric motor. The advantage of using a vortex based generator is that for a flow over a cylinder, the vibrations at resonance can occur over a broad range of Reynolds number which is denoted by the upper branch in the amplitude versus velocity plots. More details on the different response branch and modes of vortex shedding will be described in Section 2. Due to this reason, a large amount of power can be extracted even at low velocities. A VIVACE converter have high energy density, is unobtrusive, have low maintenance, is robust, modular and has a life cycle of 10-20 years [21].

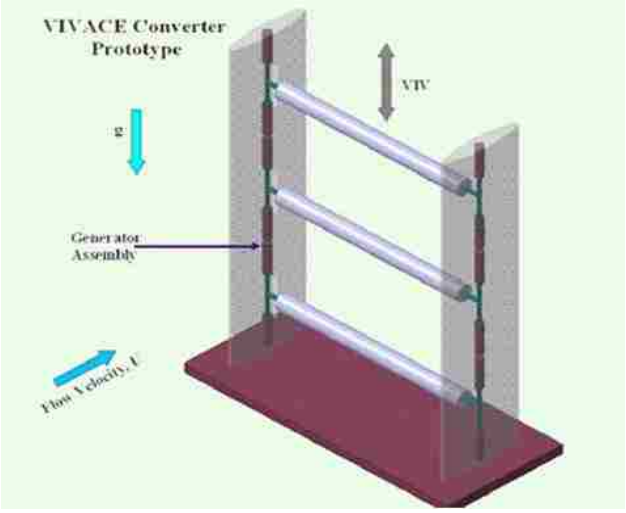

Figure 1.13. VIVACE multi-cylinder arrangement [22]

1.5 THESIS OVERVIEW

The current work aims at a detailed study of the flow over a cylinder allowed to vibrate transverse to the flow using experiments as well as commercial CFD software called ANSYS CFX. The numerical study of the displacements of the cylinder in a cross flow is studied using the fluid structure-interaction capabilities of ANSYS-CFX. In all the simulations, the cylinder is a rigid body with the ends being flexible such that the cylinder is free to vibrate in the direction transverse to the flow. Simulations were carried on for a Reynolds number of 100 to compare our results with the experimental results of Anagnostopoulos and Bearman [23]. The results from the present numerical study were compared with the numerical study of [24] and [25]. Simulations were also carried out for a higher *Re* ($1\times10^4 < Re < 3.2\times10^4$) and compared with current experimental findings. The overall purpose of this thesis is to study the phenomenon of VIV numerically as well as by using experiments; to design a very improved and efficient VIV based hydro-kinetic energy harvesting system. It is found that for a system with mass ratio (m^*) below the critical mass ratio ($m^*= 0.54$), the system always vibrates in the upper branch with high amplitudes and frequency. Thus for such a system, the power generated would not be limited to a specified velocity range but rather an infinite range of reduced velocities. Also by using non-contact type generators, the mechanical mating parts would reduce considerably, reducing structural damping and increasing the overall efficiency of the system. The structure of this thesis is as follows: Section 1 consists of an introduction to the present energy scenario in the United States, followed by an overview of the different types of hydrokinetic energy capturing device that is being used and the motivation for the present numerical study. Section 2 consists of literature review on VIV of flow over circular stationary cylinders as well as with cylinders having 1-DOF motion. Section 3 consists of the details of numerical modeling of the present study on the proposed VIV generator. Section 4 consists of a detailed explanation of the experimental facility used for the current VIV studies, a design of the used experimental set-up and the various diagnostics that were used. The results from the experiment, the simulation and its comparison with other studies are made in Section 5. Finally the conclusion of our present study, summary of current study and discussion on future work is given in Section 6.

2. VORTEX INDUCED VIBRATIONS OF CIRCULAR CYLINDERS

2.1 SIGNIFICANCE OF VIV OF A CIRCULAR CYLINDER

The study of Vortex Induced Vibrations (VIV) can be attributed to a large number of real-life scenarios such as the fluid flow in a heat exchanger, the vibration of structures, the vibrations of both riser pipes and offshore structures, and more. In the past the effects of VIV have always proved detrimental. An example of this is the collapse of the Tacoma Narrows Bridge in Washington in 1940. When a fluid flows over a bluff body, like a cylinder, due to viscous effects, a separation of fluid from the surface takes place. This separation of fluid causes an alternate shedding of vortices in the downstream region of the bluff body. These shedding of vortices cause alternate forces to develop on the surface. These forces can be large enough for the structures to vibrate, ultimately resulting in failure. As a result, understanding the fundamental nature of VIV, from a design point of view, to avoid engineering failures has become very important. Many researchers [26-30] have thus tried to reduce the VIV of structures, specifically VIV for a flow over circular cylinders. This study of the complex fluid-structure interaction has been a topic of interest for many researchers for decades. In this present study, we tried to enhance our knowledge of the VIV of circular cylinders, using the disastrous forces causing vibrations to our advantage by converting them into useful energy.

2.2 FLOW OVER STATIONARY CYLINDERS

A bluff body is defined as an object that causes a separation of flow from the surface, resulting in unsteady vortices in the wake region. The best example for a flow over a bluff body in the context of the present study is the flow over a circular cylinder. As the Reynolds (*Re*) number increases over 40, the wake region consists of alternate vortices that are shed from the surface. At this *Re*, the flow in the wake is still both laminar and unstable. As the velocity is increased, the vortex shed in the wake region goes from being laminar to turbulent. Thus, this phenomenon of vortex shedding from the surface of a circular cylinder is a function of the *Re*. The *Re* number is defined as

$$\mathrm{Re} = \frac{UD}{\upsilon} : \tag{2.1}$$

where U is the free stream velocity, D is the diameter of the cylinder and v is the kinematic viscosity of the fluid. Figure 2.1 gives the dependency of vortex shedding on the Reynolds number.

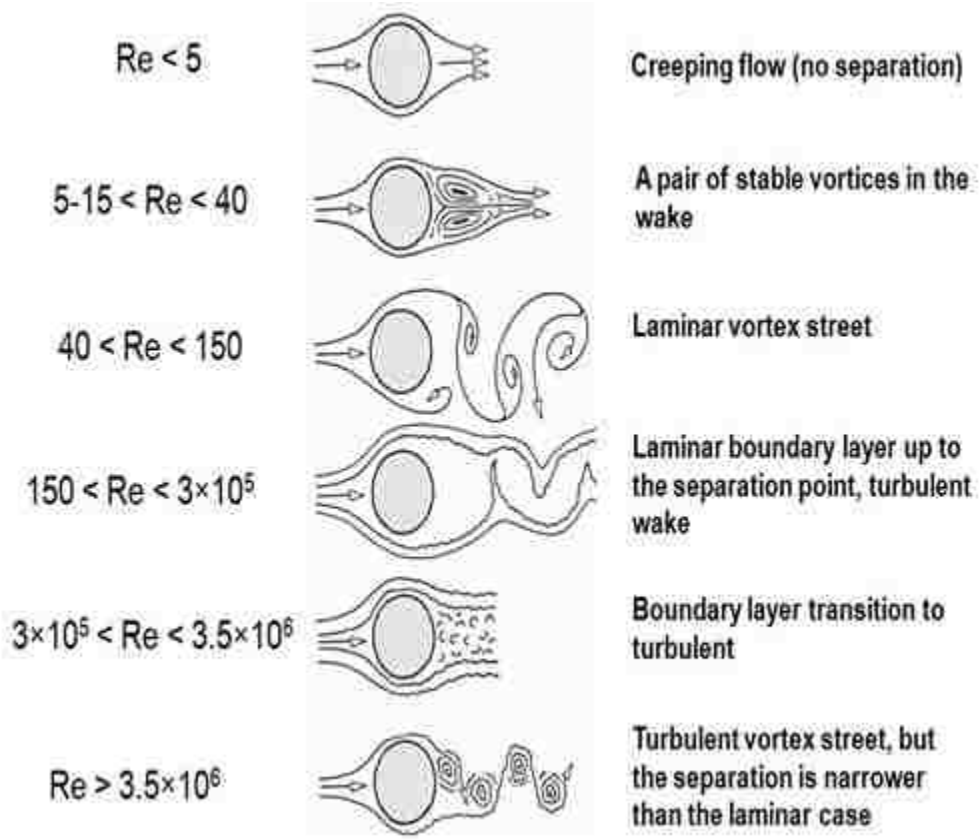

Figure 2.1. Flow over a circular cylinder at different Reynolds number [31].

As seen in Figure 2.1, for an $Re < 5$, there is no separation i.e. the fluid follows along the surface path of the cylinder. For an $Re < 40$, two stable pair of vortices are observed close to the cylinder. In the range of $40 < Re < 150$, the vortex shed are alternate. The flow in the wake region is however still laminar. For an Re above 150, the flow up to the point of separation is laminar. After the separation, it becomes turbulent. As the Re becomes greater than 200, the vortex shedding from the surface becomes 3-D [32]. The Re in the range of 300 - 1.5×10^5 is called subcritical while, in the range of

$1.5\times10^5 < \mathrm{Re} < 3.5\times10^6$ is called as transitional range. Thus, both the downstream turbulence and the nature of vortex shedding are clearly a function of the *Re*.

The frequency of vortex shedding from the surface of a cylinder is defined by the Strouhal number (*St*). The *St* is a non-dimensional frequency given by the following expression,

$$St = \frac{f_{vo} D}{U} : \tag{2.2}$$

Here f_{vo} is the vortex shedding frequency in Hz, *D* is the diameter of the cylinder in *meters*, and *U* is the free stream velocity in *m/s.* The dependence of *St* on the *Re* is shown in Figure 2.2, taken from Norberg [33].

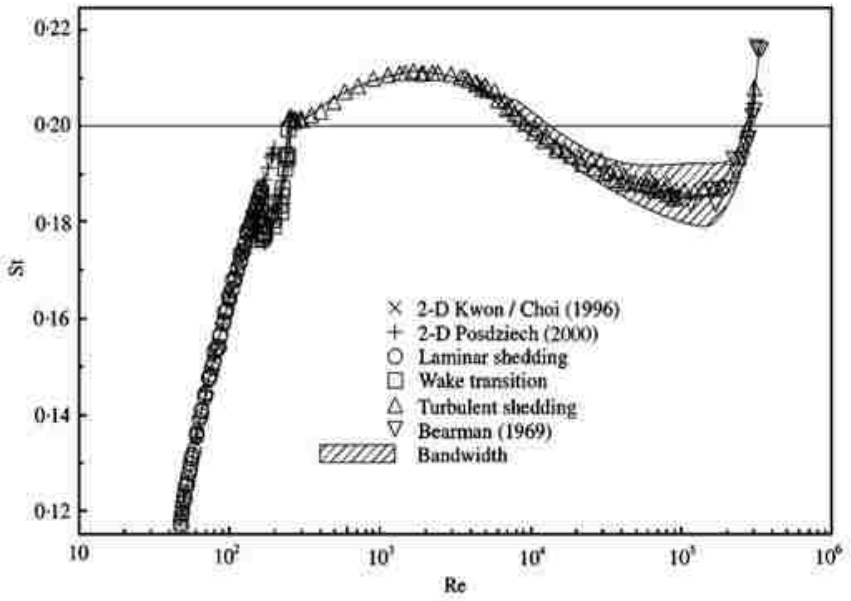

Figure 2.2. Dependency of Strouhal (*St*) on the Reynolds number (*Re*) [33]

2.3 MODES OF VORTEX SHEDDING

As the *Re* increases beyond 40, the unstable pair of vortices begins to shed in the downstream part of the cylinder. These structures in the wake region are known as the von Karman vortex street. These structures travel in the downstream region along the

flow of free stream, getting dissipated away. Both the frequency and the three dimensionalities of the vortex shedding depend upon the free stream velocity. If the cylinder, however is oscillating transverse to the flow, then the pattern in which the vortices shed from the surface are different from the traditional von Karman street. The various patterns in which the vortices shed by a transversely moving cylinder were studied in detail by [34] using a forced vibration of the cylinder. The Williamson-Roshko map is shown in Figure 2.3.

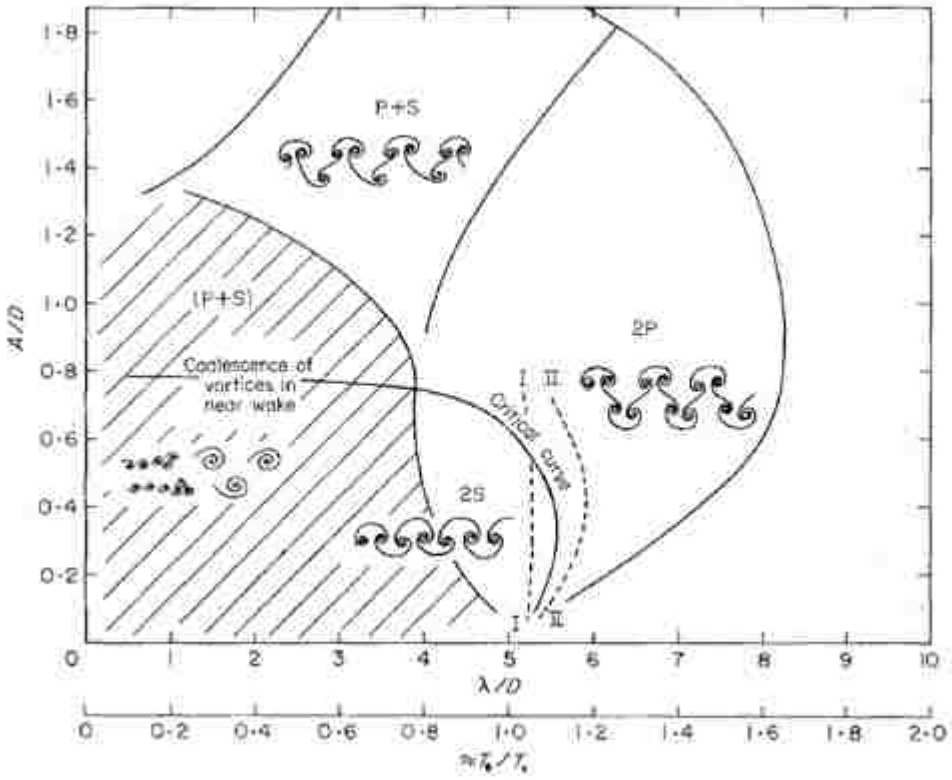

Figure 2.3. Vortex synchronization patterns at fundamental lock-in region [34]

As seen in the Figure 2.3, the critical curve marks the transition from one mode of vortex shedding to another. The labeling on the map depends on the type of wake structures being shed. The dominant patterns of vortex near the fundamental lock-in are the 2P, 2S and P+S, where 2P vortex shedding denotes 2 pair (total 4) of vortex being shed per cycle of oscillation while 2S denotes 2 single vortex being shed per cycle, similarly P+S denote a pair and a single vortex being shed per cycle. Additional patterns

also exist, such as C(P+S), C(2S), 2P+2S, and C. The initial branch has been observed numerically as well as experimentally to be associated with the 2S mode; the upper branch is associated with the 2P mode. Both forced vibrations as well as free vibrations experiments over a period of years have suggested the same. Figure 2.4 is a sketch of the different patterns of vortex shedding as denoted in the W-R Map [34].

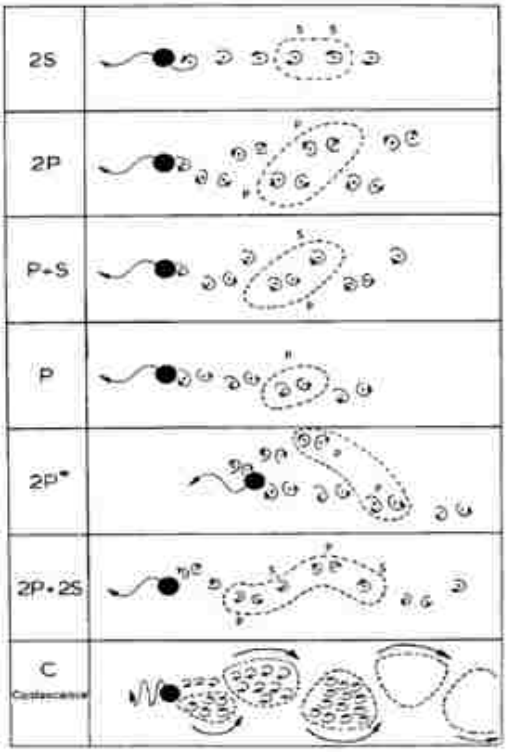

Figure 2.4. Sketch of the different patterns of vortex shedding [34]

2.4 NON-DIMENSIONAL PARAMETERS

The mass damping parameter ($m^*\zeta$) can reasonably capture the peak amplitude data. This use of the mass-damping parameter has been used by many researchers in the past to represent their peak amplitude data. One study plotted the peak amplitude response of flexible cantilevers with the *stability parameter* given by $k_s = \pi^2\left(m^*\zeta\right)$. Scruton in his experiments used another parameter called as the *Scruton number* given by $S_c = \frac{\pi}{2}\left(m*\zeta\right)$, which is also a function of the mass-damping parameter. Another non

dimensional term derived by Skop and Griffin called as the *Skop-Griffin* parameter given by $S_c = 2\pi^3 S^2\left(m^*\zeta\right)$. Table 2.1 lists additional non-dimensional parameters [35].

Table 2.1. Traditional non-dimensional parameters [35]

Mass Ratio	*m**	$\frac{m}{\pi\rho D^2 L/4}$
Damping Ratio	ζ	$\frac{c}{2\sqrt{k\left(m+m_a\right)}}$
Velocity Ratio	*U**	$\frac{U}{f_n D}$
Amplitude Ratio	*A**	$\frac{y}{D}$
Frequency Ratio	*f**	$\frac{f}{f_n}$
Streamwise force coeff	C_x	$\frac{F_x}{\frac{1}{2}\rho U^2 DL}$
Transverse force coeff	C_y	$\frac{F_y}{\frac{1}{2}\rho U^2 DL}$
Reynolds number	*Re*	$\frac{UD}{\upsilon}$

Variable *f* is the frequency of vibration, f_n is the natural frequency in water given by $f_n = \frac{1}{2\pi}\sqrt{\frac{k}{m+m_a}}$ where *k* is the effective stiffness, *m* is the total mass including the effective mass of the spring, and m_a is the added mass given by $m_a = C_a m_d$, where $m_d = \pi\rho D^2 L/4$ is the mass of fluid displaced. For a circular cylinder, C_a = 1.0, F_x and F_y

are the forces in *Newtons* acting on the surface of the cylinder in the streamwise and the transverse direction respectively, *C* is the damping constant in N-s/m, *D* and *L* are the diameter and the length of the cylinder respectively while *v* is the kinematic viscosity of the working fluid. A group at Caltech has created a unique, single-parameter formulation. This formulation allows one to set the values of mass, damping, stiffness, or any combination of the above, to zero [36-39]. This parameter is known as the "effective stiffness". The effective stiffness is given by the following equation,

$$k_{eff}^{*} = k^{*} - 4\pi^{2} f^{*2} m^{*} \tag{2.3}$$

Using this type of formulation, both the mass and the spring stiffness could all be combined to one single parameter. Thus the equation of motion can now be defined in its non-dimensional form:

$$m^{*}\ddot{y}^{*} + b^{*}\dot{y}^{*} + k^{*}y^{*} = C_{y}\left(t^{*}\right) \tag{2.4}$$

Where $y^{*} = \frac{y}{D}$, $t^{*} = t\frac{U_{\infty}}{D}$, $m^{*} = \frac{m}{\frac{1}{2}\rho D^{2}}$, $b^{*} = \frac{b}{\frac{1}{2}\rho U_{\infty} D}$ and $k^{*} = \frac{k}{\frac{1}{2}\rho U_{\infty}^{2}}$.

The cylinder response is now a function of *m**, *b**, and *k** instead of mass, damping and spring stiffness. Using such renewed non-dimensional parameters, it was possible to numerically simulate the VIV of circular cylinders in a cross flow at zero spring stiffness, damping and mass [37].

2.5 PREVIOUS EXPERIMENTS ON VIV OF CIRCULAR CYLINDER

A large amount of literature on VIV has been documented in various reviews provided by Sarpkaya [26], Griffin and Ramberg [27] , Bearman [28], Parkinson [40] and Williamson and Govardhan [30]. Both extensive experimental as well as numerical work on the VIV of rigid cylinders has provided a broad insight into the understanding of this phenomenon. Most previous studies on the VIV of a cylinder in a cross flow were performed at a high mass ratio (*m**=mass/displaced fluid mass). The working fluid used in most of the earlier experiments was air. Hence, the system had both greater mass ratio and smaller displacements. For free vibration of a circular cylinder undergoing VIV, the

at least two types of responses have been documented. Feng [41] observed a two-branch response for a high mass-damping system. Khalak and Williamson [42] reported a three-branch response for a low mass-damping system. In studies on the VIV on elastic cylinders [35, 42-44], the mass-damping parameter (m^*-ζ) was low because the working fluid used was water, as compared to air used in Feng's study. As the mass ratio was reduced, the width of the upper branch was extended. This explains the collapse of the upper branch in Feng's experiment. In his experiment, due to the usage of air as the working medium, only the initial and the lower branch, with the absence of the upper branch existed (see Figure 2.5). When the non-dimensional velocity $U^* \sim 1/S$ where S is the Strouhal number, there is a sudden increase in amplitude of the cylinder from the initial branch to the upper branch. This jump was hysteretic, accompanied by a change in both phase and in mode. The jump from the upper branch to the lower branch was accompanied by a change in vortex mode only. Figure 2.5 illustrates the two branch response observed in Feng's experiment [41] for a high mass-damping system and a three branch response observed by Khalak and Williamson [42] for low mass-damping system.

Through the method of flow visualizations using dyes, smoke, PIV etc it has been observed that the initial and the upper branch were associated with different modes of vortex shedding. Williamson and Roshko (1988) [34] in their study revealed that the initial branch was associated with the 2S mode (2 single vortices shed per cycle) while the lower branch was associated with the 2P mode (2 pair of vortex shed per cycle).

Brika and Laneville [45, 46] were the first to show the existence of the 2P vortex mode. They used smoke visualization of a free vibrating flexible cylinder in a wind tunnel to show the same modes. Figure 2.5 shows the response curve for a system with low and high mass ratios. For low mass ratios system a three branch response is observed while for high mass ratio system, a two branch response system is observed as seen in Figure 2.5 below.

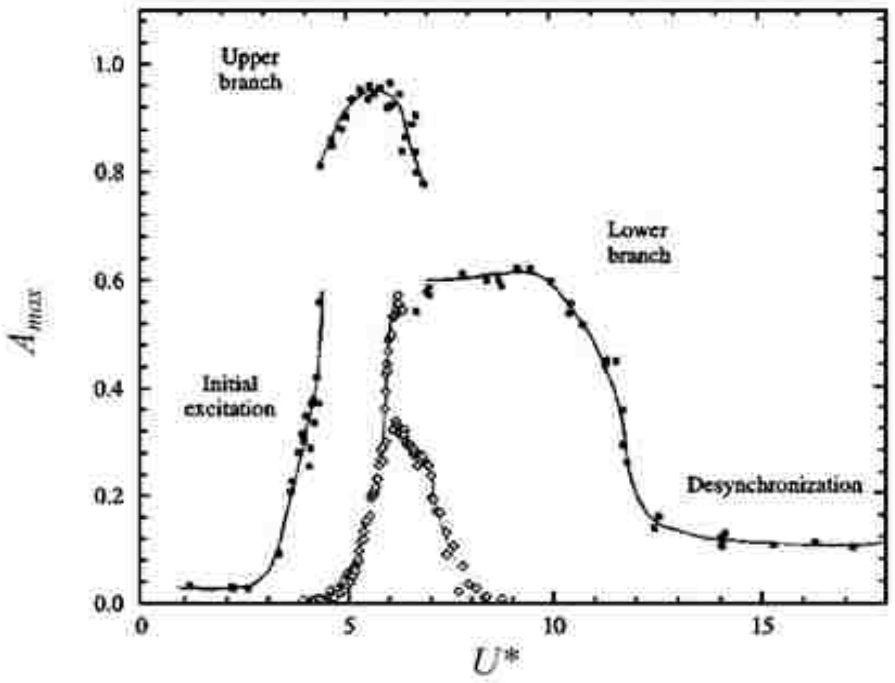

Figure 2.5. Response curve comparison for a high and low mass ratio systems [42]

2.5.1 Effect of Damping on VIV of Circular Cylinders. In the past, researchers have also studied the response of damping on the response curve of a system undergoing VIV. Scruton [47] used three different values of damping to plot a response curve. Vickery and Watkins [48] reported the effect of a mass-damping parameter on the peak amplitudes in both air and water. Feng [41] conducted an extensive study on the effect of both damping and frequencies on peak amplitudes. In this study, the working medium used was air, thus the mass-damping was very high as previously mentioned. He used the electromagnetic damper which was designed by Smith [49] to study variable mode damping response of a system. More recently, J. Klamo [39] used a controlled magnetic eddy current damping system, to study both the maximum amplitude and the effects of damping on the VIV of a cylinder in a cross flow, but using water as the working medium. Thus the mass-damping parameter used by J. Klamo was an order of magnitude lower than that used by Feng (1968). Also Feng's study was restrained to small amplitudes and two branch response due to high mass-damping. For a low mass-damping system Khalak and Williamson [44] have also looked at the effect of damping

on an entire range of response curve but only at four different damping values and 3 system masses. Very few researchers have actually studied the effect of damping for a large number of values.

2.5.2 VIV of Circular Cylinder Using Forced Oscillation. Many researchers in the past tried to solve the VIV response of a cylinder in a slightly different approach. In this approach, the cylinder was forced to vibrate at both a fixed amplitude and a predetermined frequency to study the force response of a system undergoing VIV. Using forced vibrations, parameters such as phase difference, lift and drag coefficient and modes of vortex shed from the cylinder is studied. Bishop and Hassan [50] were the first researchers to study fluctuating lift and drag using a forced vibration system. Sarpkaya [51], using forced vibrations, studied the effect of Reynolds number for a wide range of velocities. Both Koopmann [52] and Griffin [53] also performed forced vibration experiments but at low Reynolds number. Some of the most recent studies on forced vibrations were performed by Morse and Williamson [54-56]. They measured forces and phase difference on a vertically suspended cylinder using forced vibrations and compared their results to those with free vibrations. The configurations used in both the cases were precisely the same. They managed to obtain results that were very close to the experimental data, as compared to previous studies that have not been uniformly close. They have also studied both the transient and the unsteady nature of a cylinder undergoing VIV using forced vibrations. They tried to replicate a free response behavior by running a forced vibration experiment at 2 different stages, one at the lower branch where beat frequencies are observed and the other at the upper branch. It was then realized that the forces on a free vibrating cylinder can be measured using forced vibrations but only by conducting two separate forced vibration experiments.

2.5.3 Effect of Critical Mass on VIV of Circular Cylinders. One of the most significant discoveries in recent time was the existence of a critical mass for low mass-damping systems. Recent studies by Govardhan and Williamson have revealed the existence of critical mass through a series of experiments [57-60]. It has been shown that as the mass ratio m^* is reduced below 0.54, the lower branch ceases to exist and the system always vibrates in the upper branch. To prove the existence of critical mass in VIV of a circular cylinder, it was necessary to show that the body vibrated always in the

upper branch even at infinite velocities. This was achieved by removing the springs, such that the natural frequency $\left(f_n = \sqrt{k/m} \right)$ would become zero. As the system did not contain any stiffness, the non-dimensional free-stream velocity which is given by $U_n = u/f_n d$ becomes infinite. Govardhan and Williamson performed experiments at m^* values of 1.67 and 0.45 only to realize that as the mass ratio is reduced from 1.67 to 0.45, there was a sudden increase in the vibration of the system. This demonstrated for the first time that there exists a critical mass below which a system shows drastic changes in its vibrational behavior. It was observed that at infinite velocities, the cylinder would always vibrate with an *A/d* ratio of ~ 0.7. Also the ratio of the vortex shedding frequency (f_{v0}) to the frequency of the body vibrating (f) is always a constant. Thus, plotting the non-dimensional amplitude (A^*) versus f_{vo}/f gives a single point for a particular mass ratio. This point is known as the operating point. Morse and Williamson, using both free and forced vibrations, also studied the effect of Reynolds on the critical mass phenomenon [60]. They discovered that, for every body that undergoes VIV, a critical mass exists. Thus, the existence of critical mass for a body undergoing VIV is a generic phenomenon. For a circular cylinder that value was 0.54 ± 0.02 while for a tethered sphere system the critical mass was found to be ~ 0.30 [61], ~ 0.50 for a pivoted cylinder [62] and ~ 0.52 for an elastically mounted cylinder in two degrees of freedom [63]. This intriguing discovery of the existence of critical mass leads us to our present study. Figure 2.6 illustrates the existence of critical mass [58].

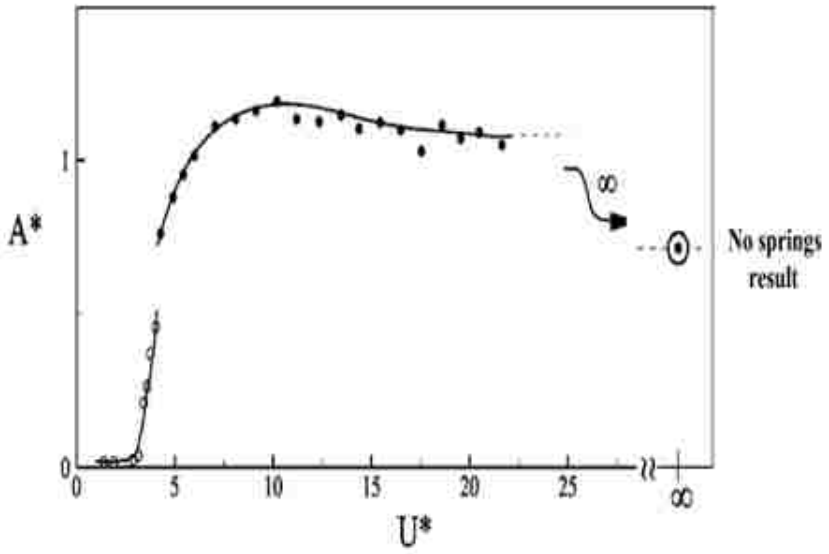

Figure 2.6. Response curve for m^* below $m^*_{critical}$ [58]

2.6 NUMERICAL STUDY ON VIV OF CIRCULAR CYLINDERS

A large number of numerical studies (both 2D as well as 3D) have also been performed to study the response characteristics of VIV for a flow over a cylinder. The amount of numerical work in this field of fluid structure interaction, at a greater Reynolds number (*Re),* is very limited. One of the difficulties of solving such a coupled fluid flow problem at a high *Re* is that the flow field in the upstream of the cylinder is very much different from the downstream side of the cylinder. For a Reynolds number (*Re*) in the range of $150 < Re < 3\times10^5$ [31], the flow is laminar up to the point of separation while it becomes turbulent in the wake region. In addition it becomes extremely difficult to predict the entire range of response curve for a cylinder undergoing VIV due to the loss of span wise correlation [64], prediction of separation point and the random disturbances due to 3D wake characteristics. The numerical complexity involved in such coupled fluid flow problem makes testing new numerical techniques interesting to many researchers. In an effort to understand such phenomena, various numerical methods have been used by researchers in the past. Zhou *et al* [65] numerically studied the flow past an elastic circular cylinder using the discrete vortex method-VIC at *Re*=200, Anagnostopoulos along with other researchers [17, 66-70] used finite element techniques to study the VIV of a cylinder in a cross flow. Reynolds Averaged Navier-Stokes (RANS) method has also

been used in the past. Guilmineau and Queutey [71] used a 2-D finite volume code (1-DOF) of the oscillation of cylinder for a Reynolds number range of 900-15000. Z.Y.Pan *et al* [64] also used a RANS code equipped with $k-\omega$ turbulence model. Al-Jamal and Dalton [72] performed a 2-D LES study of the VIV response of a circular cylinder at Re=8000 while Tutar and Holdo [73] used LES (Large Eddy Simulation) to study the forced oscillation of a cylinder at $\mathrm{Re} = 2.4\times10^{4}$. Two and three dimensional DNS (Direct Numerical Study) have also been carried out by researchers [74-77] to study VIV in a cross flow. Although it is know that DNS can accurately capture the entire turbulent characteristics for a flow over a cylinder, the constraint lies with the computational resources associated with a DNS. Neither LES nor any other turbulence model is capable of capturing the turbulence characteristics of a flow past an oscillating cylinder [72]. We however, would like to obtain a reasonable, accurate estimate of the response characteristics due to the intrigue nature and numerical complexity of such a phenomenon, when the mass ratio falls below its critical value of 0.54. It was interesting to find, using $k-\omega$ SST if the frequency response curve (f^{*} *vs U*)* behaves in a similar manner as seen in experiments.

3. NUMERICAL METHOD

3.1 COMPUTATIONAL FLUID DYNAMICS (CFD)

The solution for the flow over a cylinder as a bluff body requires a complete three-dimensional model. This model must take into account the end effects as well as the parallel versus the oblique vortex shedding from the surface. However to gain a complete understanding of the effects of various system parameters (mass, stiffness and damping) on the response of a cylinder in a cross flow, a two dimensional (2-D) study was conducted and analyzed. A 2-D study made possible the validation of the numerical study with other experiments. It also helped in greatly reducing the total computational cost when compared to a 3-D numerical simulation. A complete analysis of the given problem was possible with the help of Computational Fluid Dynamics (CFD).

CFD is a branch of fluid mechanics that uses various numerical techniques and algorithms to solve various governing equations. The conservation of mass, momentum and energy form the basis for any fluid flow problem. These governing equations were incorporated in the commercial CFD code, ANSYS CFX which was used to solve the present problem. This section introduces both the equations solved in CFD and the numerical methods used by ANSYS CFX, the Finite Volume Method.

3.1.1 Conservation Equations. The study of a flow over either a bluff or a streamlined body, like all other physical models, follows the conservation of mass, momentum and energy. The conservation of momentum equation forms the basis for the Navier Stokes Equation. The Navier Stokes Equation is a set of non-linear partial differential equations. Its conservation is an application of Newton's second law. The transient scheme used in all of the simulations was a second order backward Euler method. The advection scheme used was high resolution.

- **Conservation of mass.** The law of conservation of mass implies that the mass of an enclosed system does not change; it cannot be created or destroyed although it can be rearranged in space or even change its state into a different type. The mass of the reactants must equal the mass of the products. In vector notations, it can be written as

$$\frac{\partial \rho}{\partial t} + \nabla \bullet (\rho U) = 0 \tag{3.1}$$

Here $\partial\rho/\partial t$ is the rate of change of density, ρ is the density, *u*, *v* and *w* are the velocities in the *x*, *y* and *z* direction respectively, while $\nabla \bullet (\rho U)$ is the change in the flow velocity through the element boundaries.

- **Conservation of momentum.** The conservation of momentum equation, or the Navier-Stokes, can be expressed as

$$\rho \frac{\partial u_i}{\partial t} + \rho u_j \frac{\partial u_i}{\partial x_j} = -\frac{\partial p}{\partial x_i} + \frac{\partial \tau_{ij}}{\partial x_j} \tag{3.2}$$

Here p is the pressure, ρ is the density of the fluid and τ_{ij} is the viscous stress tensor defined by:

$$\tau_{ij} = 2\mu S_{ij}; S_{ij} \frac{1}{2}\left(\frac{\partial u_i}{\partial x_j} + \frac{\partial u_j}{\partial x_i} \right) \tag{3.3}$$

Here, μ is the effective molecular viscosity and S_{ij} is the strain rate tensor. Similar to conservation of mass, the rate of change of linear momentum of the system is equal to the rate of change of the control volume plus the net rate of flow through the control volume. Both pressure and viscous forces acting on the body were calculated with the help of the Navier-Stokes equation.

3.1.2 Turbulence Modeling. When the flow over a cylinder exceeds a *Re* of ~ 150, the flow in the wake region becomes turbulent [31]. A turbulent flow consists of fluctuations in the flow field in both time and space. Such flows consist of smaller scales (which cause energy dissipation) when compared to a flow which is laminar. Thus, a turbulent flow is a complex process when compared to a laminar flow, primarily due to its unsteady, fluctuating nature. The time dependent solutions of the Navier-Stokes however require the smaller eddies in a turbulent flow for a given domain to be resolved. Resolving all of the small scales in a turbulent flow requires extremely large computational power which is practically not feasible. Most of the complex flows may, at

times, contain eddies smaller than the smallest mesh size in a domain. For this purpose, different models have been developed using the Reynolds Averaged Navier Stokes (RANS) Scheme to model the smaller scales in a flow. The RANS approach is used to both solve for the large scale eddies and model the smaller non-dominant scales thus allowing the use of coarser grids. This leads to a reduction in computational time, giving a fairly acceptable solution for a complex flow at a much affordable price. The turbulent fluctuations in a flow are averaged out using a RANS approach. This modeling approach is used in most of the practical applications in engineering.

A large variety of different turbulence models are available in ANSYS-CFX which include Spalart Allmaras, *k*-ε (ε is the dissipation), Renormalization group (RNG) *k*-ε, *k*-ω and its variants such as the Baseline *k*-*ω* model and shear stress model (*SST*) and the Reynolds stress model (RSM). All of these models have their own advantages and disadvantages. These turbulence models have been used in many engineering applications depending upon the nature of the problem. However the turbulence model used in the present study is the *k*-*ω* Shear Stress Transport (SST).

- ***k*-ω SST (Shear Stress Transport) model.** The *k*-ω based SST model accounts for the turbulent shear stress transport and gives highly accurate predictions of the onset and the amount of flow separation under adverse pressure gradients. Also this model performs well in free shear flow, flat plate boundary layer flows and separated flows. The SST model is recommended for high accuracy boundary layer simulations. The *k*-ω SST model is such that it uses *k*-ω in the near wall region and *k*-ε in the far field region using a blending function [78-80]. The accuracy of a model in predicting flow separation in flows with adverse pressure gradients is determined by the level of eddy viscosity. Since it is know that the pressure induced separation cannot be predicted well by the standard *k*-ω model, the model is reconstructed using the observation that turbulent shear stress is proportional to the turbulent kinetic energy in the wake region of the boundary layer [79]. The governing equations for *k*-*ω* SST model are given as follows:

$$\frac{\partial(\rho k)}{\partial t}+\nabla\bullet(\rho Uk)=\nabla\left[\left(\mu+\frac{\mu_t}{\sigma_{k3}}\right)\nabla k\right]+P_k+P_{kb}-\beta'\rho k\omega \tag{3.4}$$

$$\frac{\partial(\rho\omega)}{\partial t}+\nabla\cdot(\rho U\omega)=\nabla\cdot\left(\left(\mu+\frac{\mu_t}{\sigma_{\omega 3}}\right)\nabla\omega\right)+(1-F_1)2\rho\frac{1}{\sigma_{\omega 2}\omega}\nabla k\nabla\omega+a_3\frac{\omega}{k}P_k+P_{\omega b}-\beta_3\rho\omega^2 \tag{3.5}$$

Here k is the turbulent kinetic energy, ω is the turbulent frequency, P_k is the production rate of turbulence and F_1 is called as the blending function. The traditional Wilcox k-ω model is multiplied by the function F_1 and the transformed k-ε equation is multiplied by (1- F_1). The blending function is used in the above equations in such a manner that inside the viscous sub-layer, F_1 assumes the value of unity such that the equation takes the form of the original k-ω model. Away from the wall, the blending function assumes the value of zero where the k-ε model is activated. The coefficients of this new model are a linear combination of the above mentioned model given by the following equation.

$$\psi=F_1\psi_1+(1-F_1)\psi_2 \tag{3.6}$$

Here ψ is the constant for the k-ω SST model with ψ_1 being the model constant for k-ω and ψ_2 is the model constant for the k-ε model. The values of all the coefficients are given as follows [81]:

$$\beta'=0.09, a_1=5/9, \beta_1=0.075, \sigma_{k1}=2, \sigma_{\omega 1}=2, \alpha_2=0.44, \beta_2=0.0828, \sigma_{k2}=1, \sigma_{\omega 2}=1/0.856 \tag{3.7}$$

A proper transport behavior can be obtained by the limiter to the formulation of eddy-viscosity, given by:

$$\nu_t = \frac{a_1 k}{\max(a_1 \omega, SF_2)} \tag{3.8}$$

F_2 is also a blending function and S is an invariant measure of the strain rate. The blending functions are very important to the functioning of the *SST* model. The formulation is based on the distance from the surface under consideration and the flow variables. The following are the blending functions used in the *k*- ω *SST* model.

$$F_1 = Tanh(\arg_1^4) \tag{3.9}$$

With,

$$\arg_1 = \min\left(\max\left(\frac{\sqrt{k}}{\beta' \omega y^2}, \frac{500\upsilon}{y^2 \omega} \right), \frac{4\rho k}{CD_{k\omega} \sigma_{\omega 2} y^2} \right) \tag{3.10}$$

Where y is the distance to the nearest wall, ν is the kinematic viscosity and

$$CD_{k\omega} = \max\left(2\rho \frac{1}{\sigma_{\omega 2} \omega} \nabla k \nabla \omega, 1.0 \times 10^{-10} \right) \tag{3.11}$$

$$F_2 = Tanh(\arg_2^2) \tag{3.12}$$

With,
$$\arg_2 = \max\left(\frac{2\sqrt{k}}{\beta' \omega y}, \frac{500\upsilon}{y^2 \omega} \right) \tag{3.13}$$

CD_{kw} is the positive portion of the cross-diffusion term that appeared while transforming the *k*-ε model into the *k*-ω model for the region in the domain away from the walls. These features of the SST model to predict the onset of flow separation from smooth surfaces make *k*-ω *SST* the most preferred choice for our simulations.

3.1.3 Finite Volume Method. The finite volume method is one of the ways used as a discretization technique by most of the commercial CFD software's. Using a finite volume method, it is possible to convert the rate of change of any extensive property of a

system to an equivalent formulation for use with a control volume (CV) technique. In this technique, the region of interest is divided into finite control volumes using a mesh (described later), where each mesh element is considered to be a controlled volume. The CV properties such as the mass, energy and momentum are calculated at the center of each of the CV created by the mesh. The governing equations describing the fluid flow can be solved using the control volume method by rewriting the equations as a surface integral using the divergence theorem. ANSYS CFX uses an element-based finite volume method, which first involves discretizing the entire domain using a mesh. Figure 3.1 shows a typical two dimensional mesh, where each element of a mesh is used to conserve relevant quantities such as mass, moment and energy.

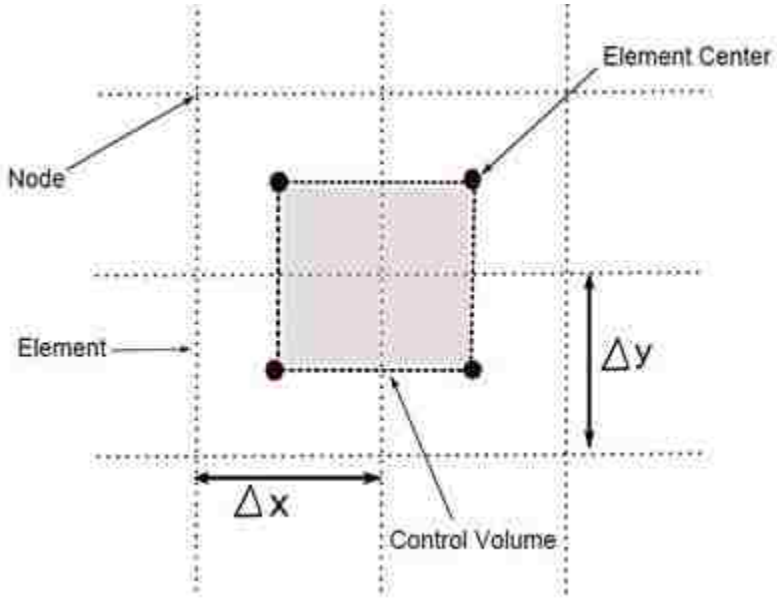

Figure 3.1. Control volume within the computational domain

To illustrate further, let us consider the conservation equations of both mass and momentum expressed in the Cartesian coordinate.

$$\frac{\partial \rho}{\partial t} + \frac{\partial}{\partial x_j}\left(\rho U_j\right) = 0 \tag{3.14}$$

$$\frac{\partial}{\partial t}(\rho U_i)+\frac{\partial}{\partial x_j}(\rho U_j U_i)=-\frac{\partial P}{\partial x_i}+\frac{\partial}{\partial x_j}\left(\mu_{eff}\left(\frac{\partial U_i}{\partial x_j}+\frac{\partial U_j}{\partial x_i}\right)\right) \tag{3.15}$$

These equations are integrated over each control volume and then the Gauss Divergence theorem is applied to convert the volume integrals into surface integrals. The following equations are obtained after control volume formulation:

$$\frac{d}{dt}\int_V \rho dV+\int_S \rho U_j dn_j=0 \tag{3.16}$$

$$\frac{d}{dt}\int_V \rho U_i dV+\int_S \rho U_j U_i dn_j=-\int_S P dn_j+\int_S \mu_{eff}\left(\frac{\partial U_i}{\partial x_j}+\frac{\partial U_j}{\partial x_i}\right)dn_j+\int_V S_{U_i} dV \tag{3.17}$$

Where V and S denote the surface integral region and dn_j denotes the differential outward normal vector. For more detailed description, the reader is referred to the book titled "An introduction to Computational Fluid Dynamics: The Finite Volume Method" [82].

3.1.4 Second Order Backward Euler. The transient schemes used in all the simulations were Second Order Backward Euler. It is an implicit time stepping scheme which is robust, implicit, time-step independent and second order accurate. The general approximation for a transient term for the nth time step is as follows

$$\frac{\partial}{\partial t}\int_V \rho\Phi dV \approx V\frac{(\rho\Phi)^{n+\frac{1}{2}}-(\rho\Phi)^{n-\frac{1}{2}}}{\Delta t} \tag{3.18}$$

Where $n+\frac{1}{2}$ and $n-\frac{1}{2}$ denote the start and end of a time step and ϕ is the respective shape function. After the approximation of the start and end values, the resulting discretization take the form:

$$\frac{\partial}{\partial t}\int_V \rho\phi dV \approx V\frac{1}{\Delta t}\left(\frac{3}{2}(\rho\phi)-2(\rho\phi)^0+\frac{1}{2}(\rho\phi)^{00}\right) \tag{3.19}$$

Since the displacement of the cylinder is highly dependent on the solution of the flow near the boundaries, a second order backward Euler is always recommended.

3.1.5 Moving Boundary and Mesh Deformation. Mesh deformation was an important part of the present study. In the present simulations, the motion of the cylinder was governed by the forces acting on it due to the periodic shedding of the vortices from the surface. Hence the motion was not known a priori. These forces were due to both the viscous as well as the pressure force on the body of the cylinder. During the simulation, at each time-step, the mesh displacement equations were solved up to a specified convergence. The body position was then updated depending on the converged solution. The displacement of the cylinder was calculated using both a FORTRAN sub-routine and the CFX Expression Language (CEL) which is explained in the later section. The motion of all nodes on a body surface was determined by the mesh motion model called Displacement Diffusion incorporated in CFX. With this model, the displacement of nodes on the boundaries was calculated using

$$\nabla \bullet \left(\Gamma_{disp} \nabla \delta \right) = 0 \tag{3.20}$$

Where, δ is the displacement relative to the previous position of the mesh and Γ is the mesh stiffness. Because the flow near the cylinder walls was of prime importance as compared to other regions in the domain, the meshes were made stiff closer to the walls, thus preserving the boundary layer. The following relation was used to determine the stiffness of the mesh near the wall boundaries in the displacement diffusion equation:

$$\Gamma_{disp} = \left(\frac{1}{d} \right)^{C_{stiff}} \tag{3.21}$$

Where d is the distance from the nearest wall and C_{stiff} is the stiffness model exponent that determines how quickly the stiffness increases.

3.1.6 Numerical Integration of 2nd Order ODE. The motion of the cylinder is governed by the following 2nd order Ordinary Differential Equation (ODE) given as,

$$m\ddot{y} + c\dot{y} + ky = F(t) \tag{3.22}$$

where m, c and k are the total mass, damping constant and the spring stiffness of the system, y is the displacement of the cylinder in the direction transverse to the flow

and $F(t)$ is the resultant of the forces in the vertical direction. Using numerical integration schemes like the Euler's forward approximation and the Runge-Kutta 4th order scheme, the above equation was solved for *y* to determine the position of the cylinder at the next time-step. The initial conditions used for the above single-degree-of-freedom system are as follows,

$$y(0) = 0 \tag{3.23}$$

$$\dot{y}(0) = 0 \tag{3.24}$$

Here $y(0)$ is the initial displacement and $\dot{y}(0)$ is the initial velocity at time t=0. For all the simulation it was assumed that the cylinder starts from rest. Hence the above initial conditions.

We used two different numerical schemes to solve for the above ODE, the First order Forward Euler's method and the Runge-Kutta 4th order scheme and compared the results for both. The following is a brief description of both methods.

- **Euler's method**. The definition of a derivative of $y(t)$ at $t = t_i$ is given by

$$\frac{dy(t_i)}{dt} = \lim_{\Delta t \to 0} \frac{y(t_{i+1}) - y(t_i)}{\Delta t} \tag{3.25}$$

Where $t_{i+1} = t_i + \Delta t$, Δt being the time-step size and $x(t)$ is continuous. The Euler's formulation proceeds from the definition of slope form of the derivative given above. The 2nd order ODE given above can be discretized in a similar way using the Euler's method,

$$\frac{d\dot{y}}{dt} = \ddot{y} = \frac{\dot{y}(t_{i+1}) - \dot{y}(t_i)}{\Delta t} \tag{3.26}$$

$$\frac{dy}{dt} = \dot{y} = \frac{y(t_{i+1}) - y(t_i)}{\Delta t} \tag{3.27}$$

Substituting the above discretized form in the ODE yields the following final equation for the new cylinder position.

The following is a derivation of the new discretized equation using the Euler's method.

$$Bodyforce + dampingforce + springforce = f(t) \tag{3.28}$$

$$mass \times acceleration = F_{total} \tag{3.29}$$

Where,

$$F_{total} = F(t) - springforce - dampingforce \tag{3.30}$$

$$springforce = k \times y(t_i) \tag{3.31}$$

$$dampingforce = c \times \dot{y}(t_i) \tag{3.32}$$

$$m\left[\frac{\dot{y}(t_{i+1}) - \dot{y}(t_i)}{\Delta t}\right] = F_{total} \tag{3.33}$$

$$\dot{y}(t_{i+1}) = \frac{\Delta t}{m} F_{total} + \dot{y}(t_i) \tag{3.34}$$

$$\frac{y(t_{i+1}) - y(t_i)}{\Delta t} = \frac{\Delta t}{m} F_{total} + \dot{y}(t_i) \tag{3.35}$$

$$y(t_{i+1}) = \Delta t\left(\frac{\Delta t}{m} F_{total} + \dot{y}(t_i)\right) + y(t_i) \tag{3.36}$$

Where, the terms with suffix *i+1* denote the value at the new time-step while the ones with *i* denote the previous time step values.

- **Runge-Kutta 4th order accurate numerical scheme**. Runge-Kutta 4th order scheme, also known as RK4, has the ability to acquire the accuracy of the Taylor series approach without the need for higher derivative calculation. This numerical scheme agrees with the Taylor polynomial of degree four. The generalized equation for a RK4 procedure to solve a 2nd order ODE is given as follows.

$$y_{n+1} = y_n + \frac{\Delta t}{6}\left(m_1 + 2m_2 + 2m_3 + m_4\right) \tag{3.37}$$

$$u_{n+1} = u_n + \frac{\Delta t}{6}\left(k_1 + 2k_2 + 2k_3 + k_4\right) \tag{3.38}$$

Where,

Thus using these coupled equations and set of constants, it is possible to find the next position of the cylinder with the help of the *RK4* method with accuracy higher than the Euler's method.

3.1.7 Modeling Techniques. The different numerical modeling techniques such as mesh type and convergence criteria for mesh and time-step independence is discussed in this section.

- **Mesh generation.** For the present numerical study, two types of mesh were created, the tetrahedral mesh and the structured hexahedral mesh with a structured O-grid at the region surrounding the cylinder. It was noticed that the tetrahedral mesh gave the same results as the hexahedral mesh for a stationary cylinder but were subjected to mesh folding and element distortions at the region around the cylinder. This was not the case for a domain with hexahedral mesh. For a hexahedral mesh, a better quality of the elements was always maintained. During a simulation, CFX has the ability to monitor the orthogonality, the expansion ratio and the aspect ratio of the elements in a domain. This feature is very important for a domain with moving walls, just like the present study. Special care was taken to make sure that the time-steps were small enough so that the displacement of the cylinder at every time-step increased gradually, thus avoiding errors due to negative volume or mesh folding. Figure 3.2 shows the mesh used in the present study.

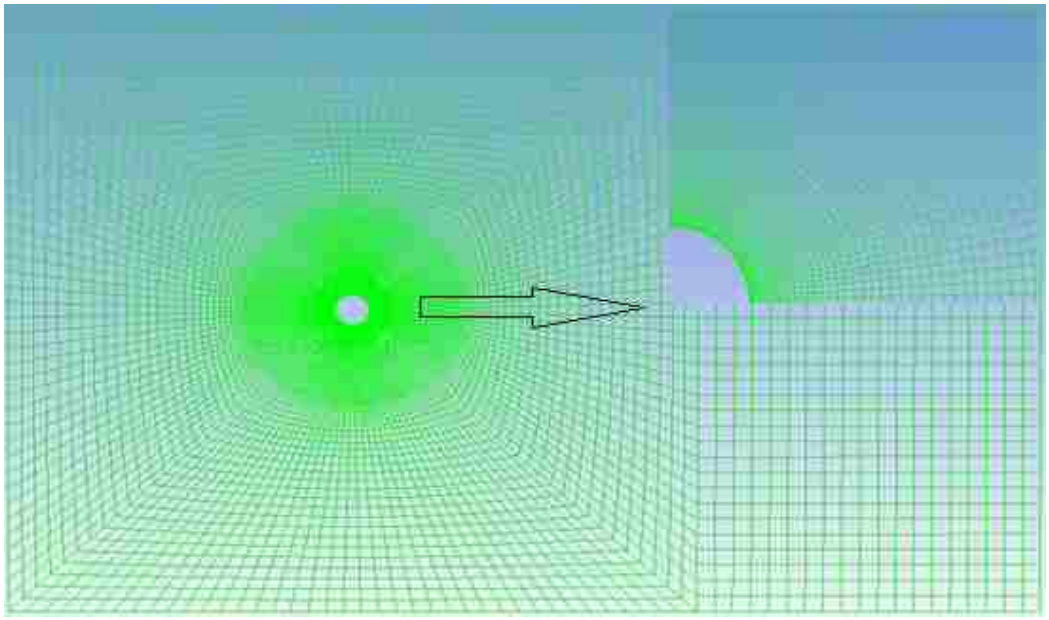

Figure 3.2. Computational mesh used in the present study

The nodes on the two horizontal boundaries were kept stationary while the movements of the mesh nodes on the vertical boundaries were unspecified, this allowed for the nodes on the boundaries to move with the elements near the cylinder thus maintaining a better quality of the mesh. The computational domain shown in the figure is very similar to the simulations performed by other researchers [83]. It can be seen that the boundaries of the domain are sufficiently far enough from the cylinder, the main reason for this being that the solution on the surface should not influence the solution on the cylinder surface. It has been noted that the artificial boundary conditions have a tendency to influence the result if not far enough [83]. It has been reported that for the given domain selected, the aspect ratio H/d should not be less than 22 and that for $L_2/d \geq 34$ [84]. For all our simulations we have used the following dimensions given in Figure 3.3.

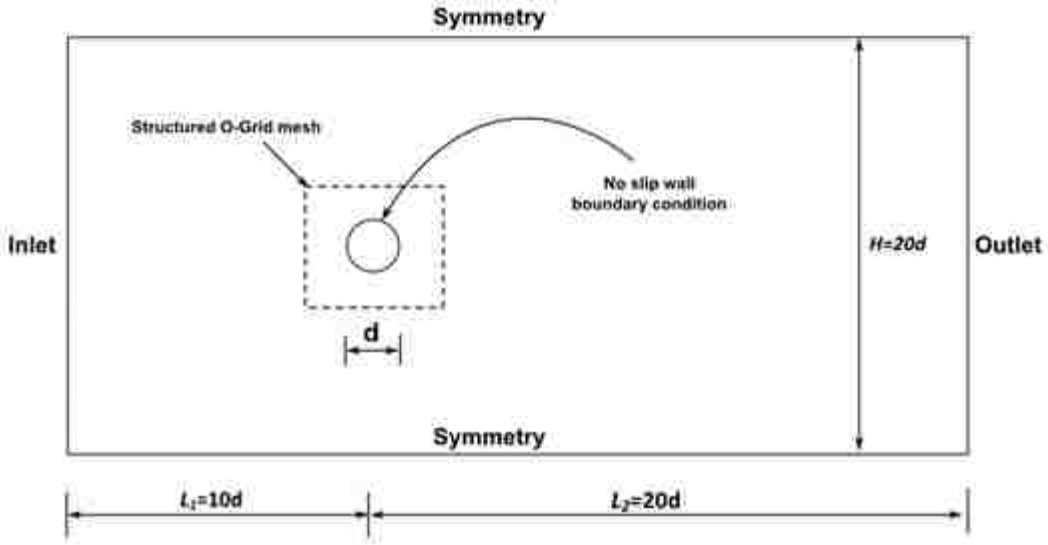

Figure 3.3. Boundary conditions and domain size used in the present study

The configuration shown in the Figure 3.3 has however given acceptable results. The mesh presented in the figure is a blocked structured O-grid mesh at the square region around the cylinder and hexahedral mesh in other parts of the domain. For grid independence, the total number of nodes on the surface of the cylinder and the total number of nodes in the O-grid region of the domain were increased. The patterns for blocking used for creating structured mesh were the same for all the meshes.

- **Grid convergence.** The determination of discretization error in a CFD simulation is conventionally achieved by examination of spatial convergence also known as grid convergence. This method involves performing CFD simulations over two or more successively finer meshes. A simulation is said to have attained grid convergence when the values of parameters important to the study does not change or is in very close agreement with each other. As the grid is refined i.e. as the number of nodes/elements in a domain is increased, the spatial discretization errors approaches zero. A normal technique to obtain grid convergence is to create two mesh one being coarser than the other, and then to check for the results. If the results are not in acceptable range, then the refinement is continued until the simulation results are within a level of tolerance accepted by the user. For grid independence study, a total of 5 meshes were created. The

total number of elements in the mesh ranged from 3068 to 35096. To check for grid independence, simulations were run for a stationary cylinder at a *Re*=100. Values of lift coefficient and *St* obtained from five different meshes M1 to M5 are given in Table 3.1.

Table 3.1. RMS lift coefficient and *St* obtained from grid convergence study

Grid/Mesh	**Total number of elements**	***Cl* (rms)**	***St***
M1	3068	0.258156	0.1562
M2	6955	0.282941	0.1707
M3	12646	0.282478	0.1719
M4	27076	0.281483	0.1719
M5	35096	0.282693	0.1719

At this Reynolds number lift coefficient C_l, drag coefficient C_d and the non-dimensional frequency i.e. the Strouhal number S_t were compared. All the elements were of high quality and the results obtained were grid independent as seen in the graphs. The graph shown in Figure 3.4 and Figure 3.5 below shows the convergence for RMS lift coefficient (*Cl*) and the non-dimensional frequency (*St*) for different grid sizes.

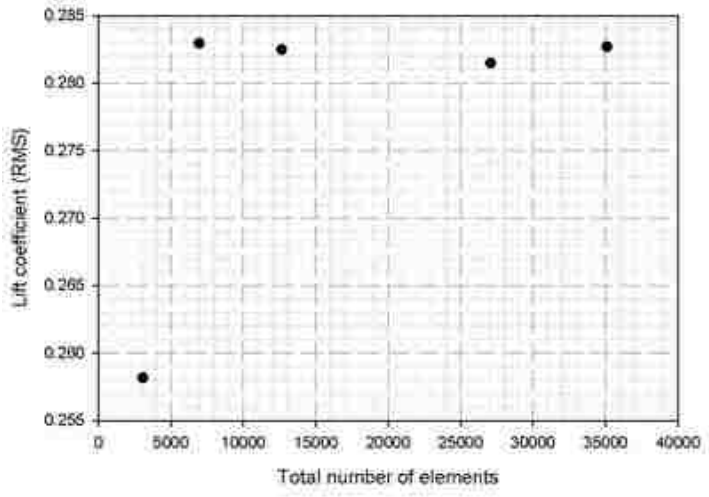

Figure 3.4. Grid convergence study using Lift coefficient (RMS) values at *Re*=100

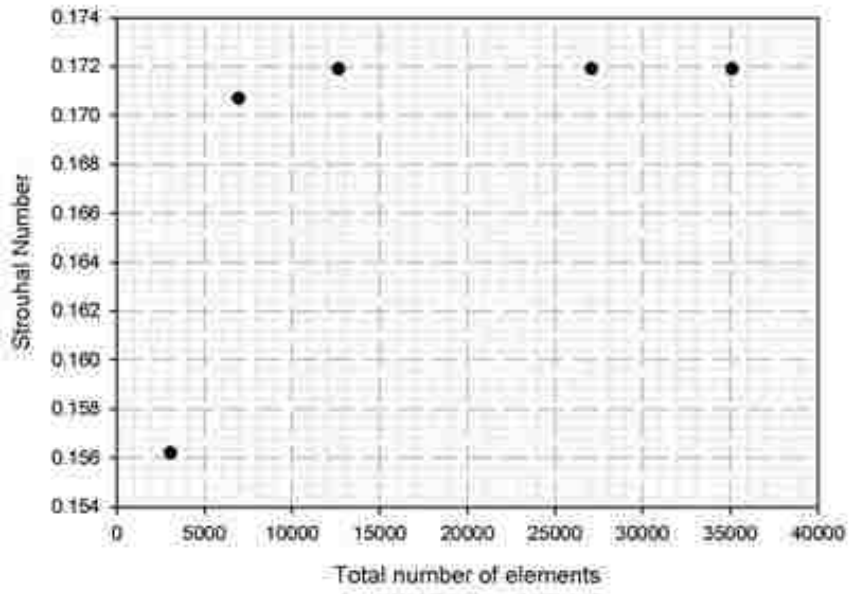

Figure 3.5. Grid convergence study using Strouhal number (*St*) values at *Re*=100

- **Time-step and residual convergence.** A very similar approach is applied to eliminate the discretization error in the time domain. Once the grid obtained is independent in space, the time-step is further reduced to check if the solution is independent in time. If the values in a simulation under scrutiny does not change or is in the acceptable tolerance limit, the solution is said to be converged in time. CFX has the option of running a simulation with either a constant time-step value or an adaptive time-stepping system. In adaptive time-stepping the time-step size keeps changing in order to satisfy a given condition. For e.g. the time-step can be chosen adaptively based on the max and min limits of the courant number specified or even the coefficient loops. The selection of time-step size was greatly influenced by the *St*. The time step size was chosen small enough to capture the vortex shedding phenomenon accurately. Values of lift coefficient and *St* obtained for five time step size are given in Table 3.2.

Table 3.2. RMS lift coefficient and *St* obtained for five different time-step sizes

Time Step	***C_l (rms)***	***St***
0.001	0.281764	0.1719
0.005	0.282693	0.1719
0.01	0.282132	0.1718
0.05	0.278162	0.1717
0.1	0.275238	0.1716

For all the simulations, the time step size was chosen to be close to 1% of the vortex shedding frequency. In the present study the RMS of the courant number was ~ 0.23. To check for time-step convergence, simulations were run at 5 different time-step values. The following graphs in Figure 3.6 and 3.7 show convergence obtained at time-step $\Delta t = 0.005$. Henceforth all simulations were performed at this value of time-step.

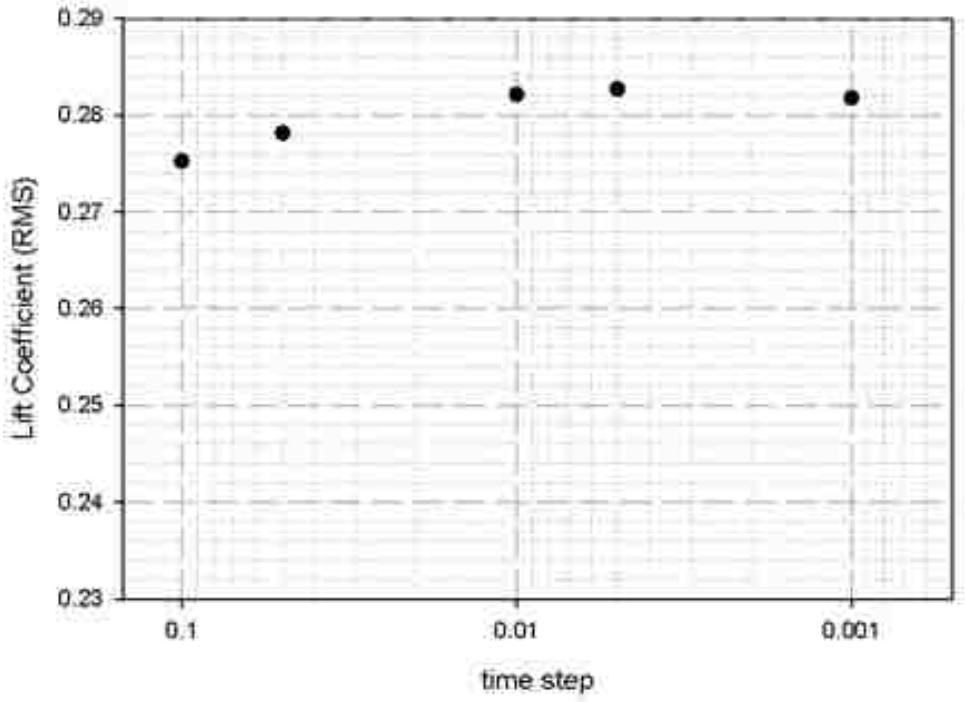

Figure 3.6. Time step convergence study using lift coefficient (RMS) values

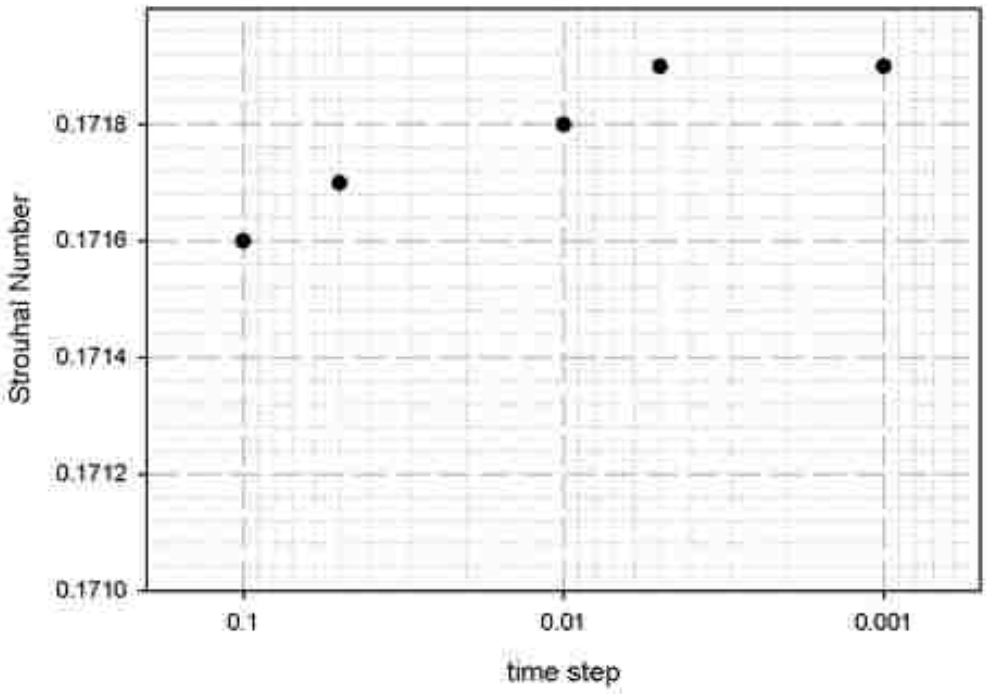

Figure 3.7. Time step convergence study using Strouhal number (*St*) values

Due to transient nature of the present study, the time step, the grid size and the number of coefficient loops were carefully selected. For every decrease in the residual value, the simulation time would increase greatly. Reducing the time-step helped reducing the number of coefficient loops but greatly increased the computation time. A time-step size of 0.01 would be able to accurately capture the vortex shedding phenomena but when the cylinder vibrates at resonance, the quality of mesh elements is affected thus making convergence difficult. A time-step value of 0.005 was selected for all the numerical study. This value gave good residual convergence up to 10^{-5}. Convergence as low as 10^{-6} was also achieved with this time-step by increasing the number of coefficient loops.

- **Boundary condition selection.** The boundary conditions adopted in the present numerical study have been shown in the Figure 3.3. A total of four different types of boundary conditions were used in the present numerical study.

  ○ **Inlet.** The left extreme vertical boundary is the Inlet where the free stream velocity of the system is specified. The free stream velocity used in all the simulations

was dependent on the Reynolds number *(Re)* which is given by the expression $\mathrm{Re} = ud/\upsilon$, where *u* is the free stream velocity, *d* is the diameter and υ is the kinematic viscosity of the fluid. The velocity is specified in its local Cartesian coordinate system which is in the form $\vec{U} = U_x\hat{i} + U_y\hat{j} + U_z\hat{k}$ where U_x, U_y and U_z are the magnitude of velocity in the *x*, *y* and *z* direction respectively. For the present numerical study the velocity was specified only in the *x*-direction while the *y* and *z* component of velocity was given a value of zero.

- **Outlet.** This boundary condition is to the far down stream side of the domain where the relative pressure is specified over the entire boundary. In all the simulations, the relative pressure at the outlet is specified as zero.

- **Symmetry**. Since the entire simulation is a 2-D simulation with its depth in the *z* direction being infinity, the front and the back sides of the domain were set to symmetry boundary condition as CFX is not capable of solving actual 2-D geometries.

- **Wall.** Wall boundary condition is a very commonly used boundary condition used to separate the fluid region from the solid region. In the present study a no slip wall boundary condition has been enforced on the walls of the cylinder. In this boundary condition, the velocity of the fluid at the wall surface is always zero *i.e.* $U_{wall} = 0$

4. VIV EXPERIMENTAL FACILITY

This section provides an overview of the experimental facility used for the current VIV studies, a design of the used experimental set-up and the various diagnostics that were used.

4.1 WATER TUNNEL FACILITY

The Missouri S&T water tunnel used for the present experiment is housed in a Hydrodynamics Laboratory (Toomey Hall) and consists of a free surface test section that is 0.381 meters (15 inches) wide, 0.508 meters (20 inches) deep and 1.524 meters (60 inches) long and has an overall volumetric capacity of ~1000 gallons. The test section is made of tempered glass and allows views from all the three sides. The maximum velocity attained by the flow in the test section is ~ 0.91 m/s (36 inch/sec) but for all the test case that was run in this water tunnel, the flow velocity never exceeded 0.5842 m/s (23 inch/sec). A layout of the water tunnel used in the present study is shown below in Figure 4.1

Figure 4.1. Water tunnel facility at the Hydrodynamics Laboratory (Toomey Hall) in Missouri University of Science and Technology

The test section velocity was calculated at 9 different pump frequencies using a laser strobe and a graph of pump frequency versus the test section velocity was provided. Using a 6^{th} degree polynomial curve fitting approach, the velocities were obtained for the entire range of fluid flow inside the test section. The velocities considered during the experimental run were all obtained from this 6^{th} degree polynomial curve fit. The velocity in the test section was changed by varying the pump frequency. A speed controller attached to the tunnel was used to vary the pump frequency. The free stream velocities at different pump frequencies are listed and plotted in Table 4.1 and Figure 4.2 respectively.

Table 4.1. Free stream velocity at different pump frequencies

Hz	**m/sec**
0	0
2.5	0.056921
5	0.11237
10	0.222123
15	0.31181
20	0.422351
25	0.520294
30	0.635889
35	0.753212
40	0.956488

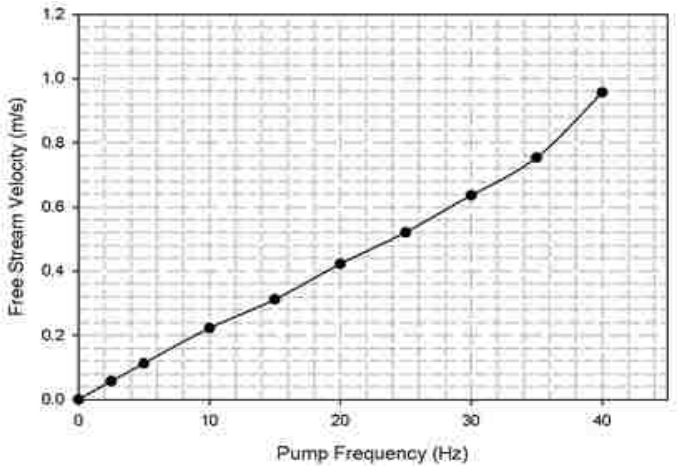

Figure 4.2. Free stream tunnel velocity plotted at different pump frequencies

4.2 DESIGN OF EXPERIMENTAL SET-UP

The experimental set-up consist of air bearings, mounting blocks, end mounts, stainless steel rods, traversing plate, indicator pin, an aluminum frame, perforated 90 degree angle bends and custom made extension springs. The air bearings (#S301201) were purchased from Newway air bearings, while the extension springs were purchased from W. B. Jones Spring Co., Inc. Figure 4.3 below shows the entire experimental set-up placed on the top of the water tunnel test section with Figure 4.4 showing the cross sectional schematic of the set-up.

Figure 4.3. Experimental set-up placed on the top of the water tunnel test section

The traversing plate as seen in the schematic above consists of a cylinder attached to it mounted vertically into the water. The traversing plate is made from plexi-glass, as it offers clear visibility, easy machinability and low weight which are important for the design of the experiment. The cylinders used in the experiments were made either of acrylic rods or PVC pipes with acrylic end caps that would press fit into the two ends of the PVC pipe. Figure 4.4 shows the cross sectional schematic of the experimental set-up.

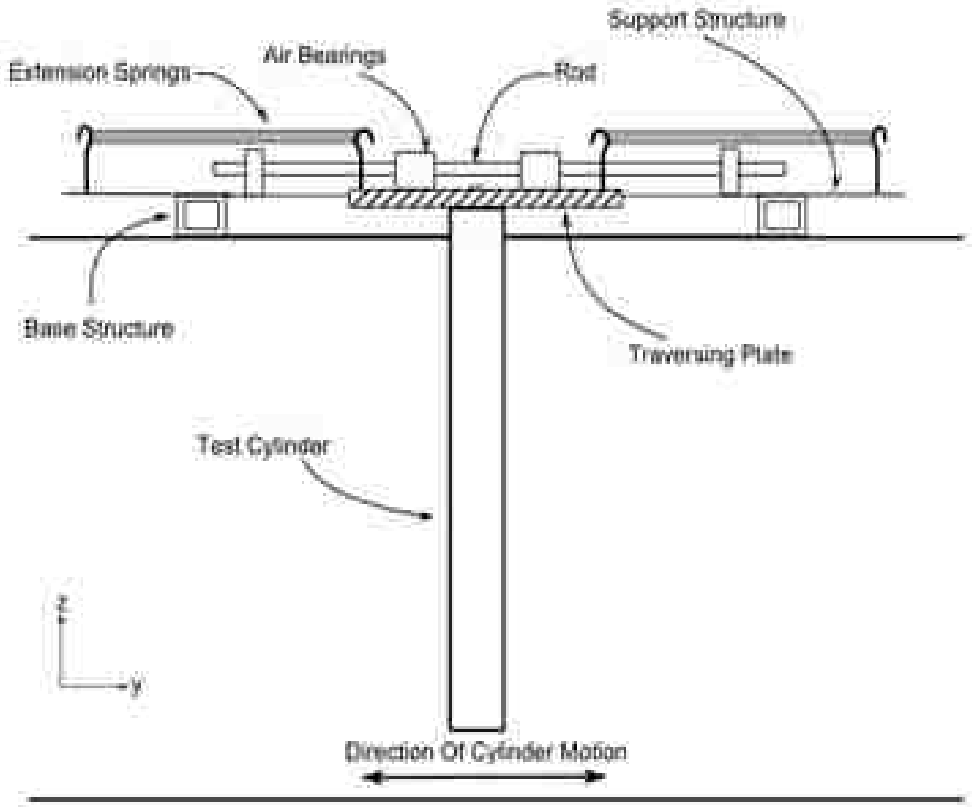

Figure 4.4. Schematic of the Experimental set-up used in the present study (flow of water into the *y*-*z* plane)

The main reason for using an acrylic rod and PVC pipes is that the acrylic rods can be machined very easily. In addition the PVC pipes have a low density that helps in reducing the overall mass of the system. The end of the pipe that is above the surface of the water and connected to the traversing plate have a 9.525 mm (3/8”) threading. A 9.525 mm (3/8”) bolt was used to fasten the cylinder to the traversing plate using these threads. This simple system of using a bolt made it convenient to replace the system with different diameter cylinders as and when required. Figure 4.5 below shows the different diameter cylinders used for the present study.

Figure 4.5. Different diameter cylinders used in the experiment

Four air bearings each having an inner diameter of 0.0127 m (½ inch) was used in this experiment. The choice of air bearings over other bearing types was made to minimize frictional damping (almost zero for the air bearings) and also ensure one dimensional transverse motion of the cylinder. The air bearings were housed in a mounting block that was machined in house to which a compressed air line was attached. The operating pressure to the air-bearings during the various experimental runs was held constant at 80 psig. Each bearing had a maximum radial load capacity of 10 lbs and a maximum pitch moment of 7.5 lbs-in.

The springs used in the experiment were extension springs custom made of music wire having an outer diameter of 0.012 m (0.4725 inch) and an overall length of 0.508 m (20 inch). Both the ends of the spring were hooked to a 6.35 mm (¼ inch) screw-in hook, where one hook was connected to the traversing plate while the other connected to a 90 degree bend perforated plate. The holes in the perforated plate were used to adjust the extension of the springs. The elasticity of the system was varied by using different springs connected in parallel as seen in the figure. Since the springs were connected in parallel, the total spring stiffness was calculated by adding the spring stiffness together. The rods on which the air bearing slides were made of stainless steel having a diameter tolerance of -0.0005” to -0.001”. The frame, the end mounts and the mounting blocks were made of general purpose 6061 aluminum alloy. All the material for the design of the

set up except the springs and the bearings were purchased from McMaster-Carr. The housings for the bearings and the traversing plates were machined in-house.

The indicator pin having a diameter of 1.55 mm (0.061 inch) as seen in Figure 4.3 is mounted on the traversing plate, which is used as a tracker. A MATLAB script (see appendix A) is used to track the movement of the pin thus providing us with the displacement versus time history of the oscillating part of the set-up. Behind the pin is a white screen which contains line markings with each line being $1/10^{th}$ of an inch apart. These markings were made accurately using InkScape. These markings are used by the MATLAB script to find the relative position of the pin indicator from one frame to another.

4.3 DAMPING TEST

Before any test procedures were carried out in the test section of the water tunnel, free damping test was performed to obtain the damping constant (c) and the damping ratio (ζ) for a given cylinder. In this test, the traversing plate with the cylinder attached to it was given an initial displacement from the mean zero position. This is performed when the velocity of water in the test section is zero. Due to the viscous damping provided by the water in the tunnel, the vibrating cylinder would eventually come to rest back at its mean position. As soon as the cylinder is displaced, the high speed camera was used to capture the position of the cylinder at different time intervals. The images were then read by a MATLAB script to track the pin which is placed on the traversing plate to give displacement versus time values of the oscillating cylinder.

Two methods were used to find out the damping values of the system. In the first method a MATLAB script was used to calculate all the peak to peak displacement values at every cycle of the oscillation. Using these data and the set of equations given below, the damping constant (c) and the damping ratio (ζ) is calculated for the system.

$$\delta = \frac{1}{n} \ln \frac{x_0}{x_n} \tag{4.1}$$

$$\zeta = \frac{\delta}{\sqrt{4\pi^2 + \delta^2}} \tag{4.2}$$

$$\zeta = \frac{c}{2\sqrt{km}} \tag{4.3}$$

where δ is called as the logarithmic decrement, ζ is the damping ratio, x is the peak displacement from the mean, k is the total stiffness of the spring in *N/m*, m is the system mass and c is the damping constant in *N-s/m*. For a single cylinder, five different damping tests were conducted independently. The values of damping constant (c) and damping ratio (ζ) are then averaged over the five run to obtain the final value of c and ζ. Also for every run, a MATLAB script is used to calculate the values of damping constant after every cycle. The damping values used from each run is then averaged. The average of all the values obtained from the damping test is used for all future tests. Figure 4.6 shows the displacement versus time plot for the damping test conducted in a water medium for a system having a cylinder with a diameter (D) 0.04826 m (1.9 inch) attached to the traversing plate.

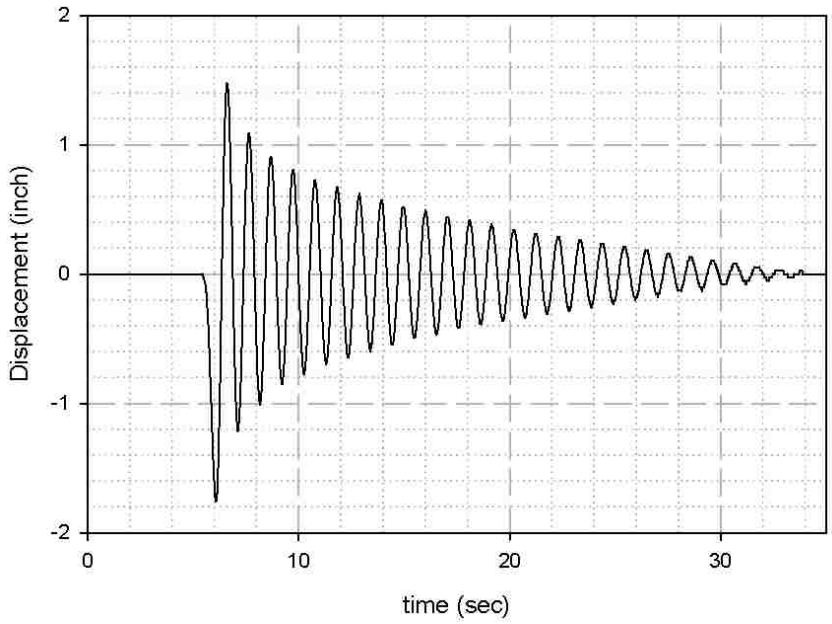

Figure 4.6. Displacement versus time record for a damping test with cylinder (D= 0.04826 m) in water

In the second method, the damping constants were found out using the slope of the peak displacements. The damped single-DOF mass-spring-damper system was reduced to the following quadratic equation shown in Eq (4.4) called as the *characteristic equation* by the method of substitution.

$$m\lambda^2 + c\lambda + k = 0 \tag{4.4}$$

The equation above is solved using the quadratic formula to give the following roots of the equation,

$$\lambda_{1,2} = -\frac{c}{2m} \pm \frac{1}{2m}\sqrt{c^2 - 4km} \tag{4.5}$$

Rewriting the roots given in equation (4.5) yields,

$$\lambda_{1,2} = -\zeta\omega_n \pm \omega_n\sqrt{\zeta^2 - 1} \tag{4.6}$$

Where ω_n is the natural frequency of the system, since the present motion of the system was under-damped *i.e.* $0 < \zeta < 1$ Eq (4.4) was reduced to the form,

$$y(t) = Ae^{-\zeta\omega_n t}\sin(\omega_d t + \phi) \tag{4.7}$$

Where A and ϕ are the constant of integration and ωd is called as the damped natural frequency given by,

$$\omega_d = \omega_n\sqrt{1-\zeta^2} \tag{4.8}$$

For a system governed by the Eq. (4.4), where the cylinder is given an initial displacement of Y0 at time t=0, the time decaying motion of the system is given by

$$y(t) = Y_0\sqrt{1+\zeta^2}e^{-\zeta\omega_n t} \tag{4.9}$$

Taking log on both sides we get,

$$\ln(y) = -\zeta\omega_n t + \ln(Y_0\sqrt{1+\zeta^2}) \tag{4.10}$$

Eq (4.10) is of the form $y = mx + c$, representing the equation of a straight line. Thus if the natural log value of the peak displacements is plotted against its time values, the intercept with the y axis would give the value of $-\zeta\omega_n$ from which the damping constant can be calculated. The figure below shows the natural log of peak displacements plotted against its respective time values for a cylinder having a diameter of 0.04826 m (1.9 inch). A linear curve fit in the form $y = mx + c$ is used to represent the data as seen in the Figure 4.7 below. It is seen that the values of displacement at the beginning of the curve fit deviates slightly away from the line given by $y = -0.016x - 3.0856$. This deviation is very little hence does not affect the slope of the line. The value of the damping constant obtained by this method of finding the slope is in good agreement to the value obtained by the previous method.

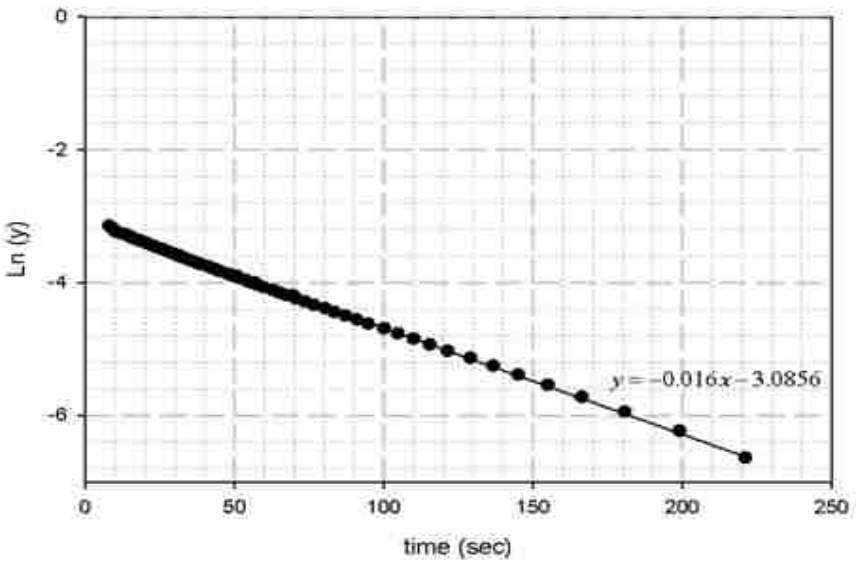

Figure 4.7. Peak amplitudes plotted along a linear curve fit.

However it was observed that for this method to work well, the number of peak displacements obtained by a damping test should be large enough to obtain an accurate curve fit with little error. The displacements in Figure 4.7 were obtained from a damping test conducted in air, thus having a damping constant value an order of magnitude lower than when in water.

4.4 IMAGE PROCESSING

A Photron FASTCAMX-1024 PCI high-speed camera was used to record the response behavior of the system. A script written in MATLAB was used to read all the images recorded by the high speed camera. The algorithm was developed using the image processing tool box in MATLAB. A pin having a diameter of 1.524 mm (0.06 inch) was mounted on the traversing plate which moved along with the system. The camera was used to capture the position of the pin at equal intervals of time. Behind the pin was a clear white frame background. The reason for using a long thin pin and a clear white background is that the MATLAB script can easily distinguish between the black pixels of the pin and other pixel values thus accurately finding the position of the cylinder for every image read. The brightness, contrast, aperture and focus of the lens of the camera were adjusted before the experiment to obtain a clear view of the indicator pin and the measurement lines on the screen behind the pin as seen in figure below. Figure 4.8 shows one of the images produced by the camera which is read by the MATLAB script to obtain the position of the pin as seen in Figure 4.8

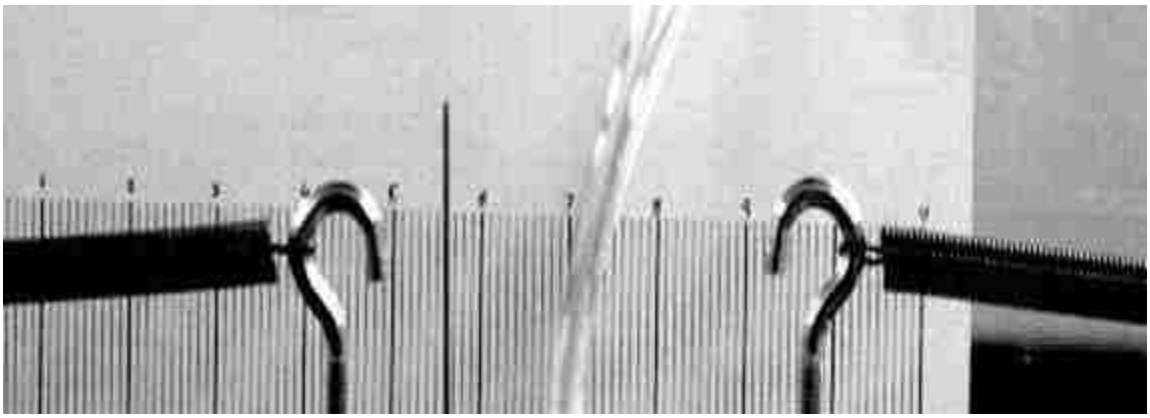

Figure 4.8. Intensity Image produced by the high speed camera

The images obtained were intensity images and hence black has the value of zero while white has the value of 1 and all other colors appear grey having value between zero and one. The size of the image is 512×128 and the number of frames/sec was kept at a

constant value of 60 fps. Thus the position of the pin in every successive frame is 1/60th of a second apart.

The MATLAB script reads the images as a 2-D array having values between 0 and 1. After all the images are read, the single 3-D array is used to save the values of all the images. An algorithm to find the least value in the image in the upper portion of the image is implemented where only the pixel containing the locator pin is black, rest all other pixels are either white or grey. The output of the script gives the displacement versus time plot. To obtain the frequency of oscillation, a FFT (Fast Fourier Transform) is performed on the displacement-time values. Figure 4.9 plots the displacement of the cylinder (D=0.04826 m) oscillating at resonance condition (frequency=0.9 Hz). Figure 4.10 is the frequency power spectrum for the experiment obtained using a FFT.

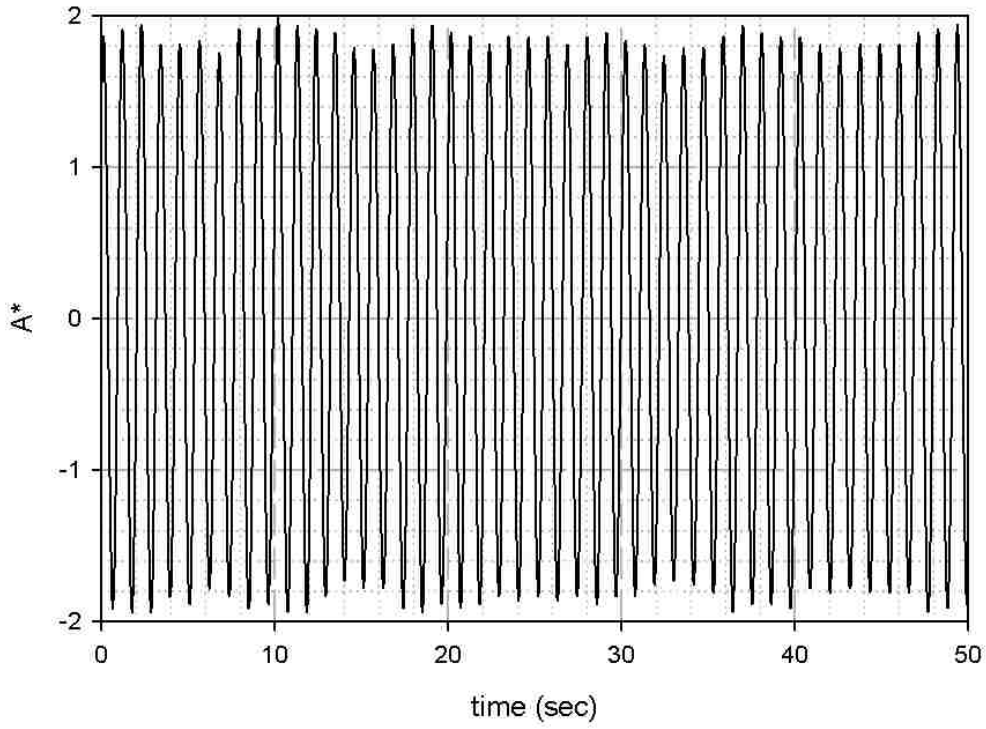

Figure 4.9. Displacement versus time plot for a cylinder (D=0.04826 m) at resonance (frequency= 0.9 Hz)

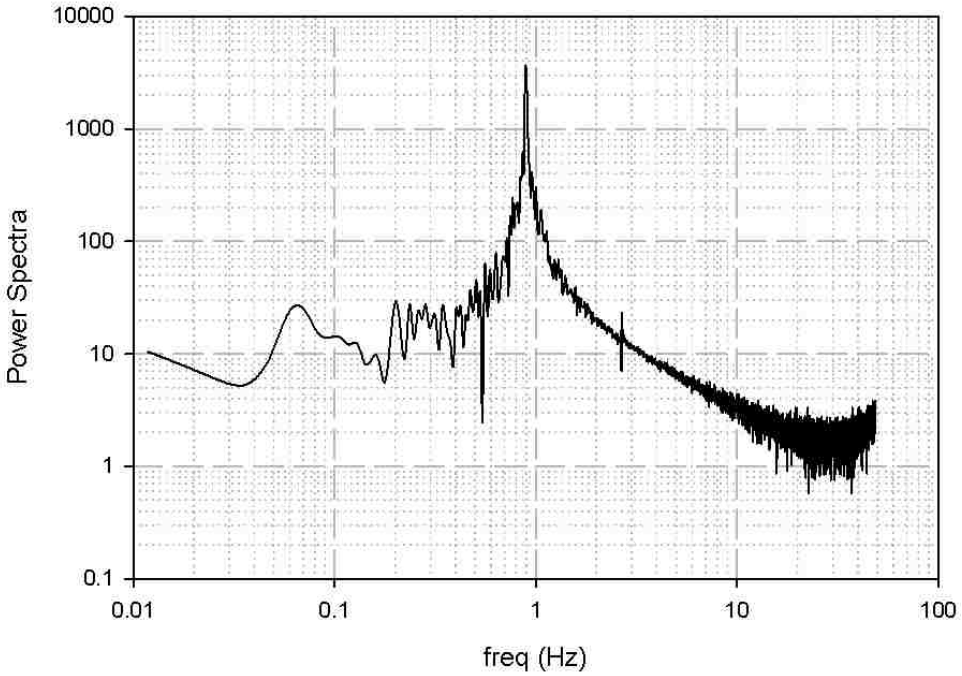

Figure 4.10. Power spectral sensities versus frequency

4.5 BOUNDARY LAYER AND END EFFECT CONSIDERATION

The experimental results were independent of end effects and boundary layer dependency. The experimental arrangement was placed very close to the camera hence the position of the set-up was at the extreme downstream side of the test section of the water tunnel. The total length of the test section is 1.524 m (60 inches) and the cylinder was placed at a distance of 0.1524 m (6 inch) from the downstream end. Thus the position of the cylinder from the upstream end was 1.3716 m (60”- 6”=54 inches). For a laminar flow over a flat plate, the boundary layer thickness is calculated using the equation given below.

$$\frac{\delta}{x} \approx \frac{4.99}{\sqrt{\mathrm{Re}_x}} \tag{4.11}$$

Where x is the distance from the leading edge (upstream) of the plate at which the boundary layer thickness δ is to be calculated. For every experimental run, the lowest velocity in the response curve (A/d versus U^*) was considered for the calculation of Re_x.

A total of 6 different cylinders have been used in the present study. Each of them has a diameter of 0.04826 m (1.9 inch), 0.0334 m (1.315 inch), 0.03175 m (1.25 inch), 0.0254 m (1 inch), 0.2223 m (0.875 inch) and 0.01905 m (0.75 inch) respectively. The Reynolds numbers at the start of the experiment when the system is in the lower branch are given in the Table 4.2 below.

Table 4.2. Boundary layer thickness (δ) for different *Re* number

Diameter	**Velocity**	$\boldsymbol{Re_D}$	$\boldsymbol{Re_X}$	**Displacement**
m	***m/s***			***m***
0.04826	0.33	17841.67	31432.5	0.038605
0.033401	0.277	10365.1	26384.25	0.042136
0.03175	0.22	7825.296	20955	0.047281
0.0254	0.195	5548.846	18573.75	0.05022
0.022225	0.24	5975.68	22860	0.045268
0.01905	0.19	4054.926	18097.5	0.050877

We consider the lowest value of the Reynolds number to check for interference. On substituting the values in the Eq. (11), we obtain a maximum value of δ=0.0508 m (2.0 inches). The distance between the ends of the cylinder and the bottom wall is 0.09525 m (3.75 inch) thus this makes it certain that for every case run, there was no interference of the ends of the cylinder with the bottom wall boundary layer. As the velocity is increased, the R.H.S of the above equation will keep on decreasing and the height of the boundary layer will keep on decreasing. Thus, it can be safely assumed that the end of the cylinder was far removed from the boundary layer.

5. RESULTS

To understand the physics involved in the VIV of elastically supported circular cylinders, numerical simulations as well as experiments were performed for a wide range of *Re*. To validate our numerical simulations, results were compared with the various experimental and numerical data sets available in the literature [24, 25]. For *Re* in the range 1×10^4-3.2×10^4, simulations were compared with the results obtained from our present experimental study. A detailed list of numerical simulations performed in the present study with their mass – damping parameter ($m^*\zeta$) is given in Table 5.1

Table 5.1. List of simulations performed in the present study

	Type	**Re**	**# of Simlns**	$m^*\zeta$
1	stationary	45 - 200	10	∞
2	moving	90 - 150	8	0.17892
3	moving	100	11	0
4	moving	1×10^4 - 3.2×10^4	9	0.0389
5	moving	<200	8	0.005 - 10

5.1 RESULTS FROM PRESENT NUMERICAL SIMULATIONS

Numerical simulations were performed for a flow over a stationary as well as an elastically mounted cylinder for a wide range of *Re*. The numerical model was first validated for a stationary cylinder in the laminar regime of *Re* ($50<Re<200$) using experimental and numerical results from [85-88];and next for an oscillating cylinder undergoing VIV. The oscillating cases were further subdivided into numerical experiments with and without mass damping and were validated in the laminar flow regime ($Re=100$). The results for VIV based motion with mass damping were compared with the experimental findings of Anagnostopoulos and Bearman [89]; while those without mass damping were compared with the numerical results of Shiels *et al* [24] and Placzek *et al* [88]. Simulations at the high *Re* ($1\times10^4<Re<3.2\times10^4$) flow were modeled using the *k-ω* SST turbulence model [79] and are validated with the experiments done in our laboratory.

5.1.1 Validation of Numerical Model for a Stationary Cylinder The forces (drag and lift) and *St* on a stationary cylinder in the laminar regime and up to a *Re*=200 is investigated. It is well know that as *Re*>~200, the shedding of vortex becomes three-dimensional [85] and it becomes fairly difficult to predict the frequency of vibration of a cylinder using two-dimensional simulations. Thus by investigating the flow over a cylinder at low Reynolds number we can verify the capability and accuracy of the present numerical study. In addition, for a stationary cylinder, there is no mesh motion and this allows us to check the validity of important parameters like the boundary conditions, domain size and type of mesh. For the laminar regime, all simulations were carried out over 50 <*Re*< 200. It was observed that as Re≥50, the vortex street in the wake become unstable with alternate pairs being shed from either side [31]. For the entire range under consideration (50<*Re*<200), we compare three different parameters mainly the coefficient of lift, drag and the Strouhal number (*St*). To validate our simulations these were plotted along the entire range of *Re* until the wake characteristics become three-dimensional. Figure 5.1 shows lift and drag coefficients values for *Re*=100 simulation. Values of 0.35 and 1.378 for lift and drag coefficients are obtained respectively and are in close agreement with the values obtained by Shiels *et al*, Zhou *et al* and Anagnostopoulos [37, 65, 66].

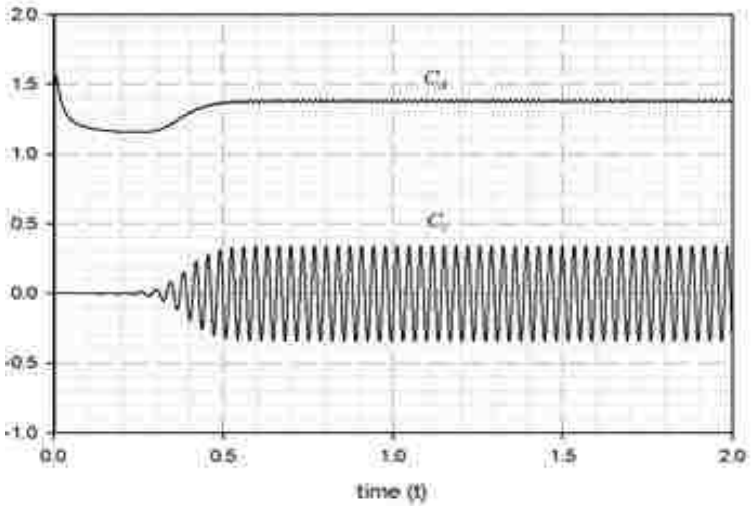

Figure 5.1. Drag and Lift coefficients for a flow over a stationary cylinder at *Re*=100

It is seen that after some initial time period until the flow is completely developed in the domain, the lift and the drag forces reach stable and regular periodic oscillations. This initial time period is required for a flow to completely develop inside the domain and also to trigger the vortex shedding around the cylinder. The frequency of the vortex shedding is calculated from the lift coefficients using a Fast Fourier Transform (FFT) and is shown in Figure 5.2. Table 5.2 gives the comparison of present results obtained for a stationary cylinder at *Re*=100.

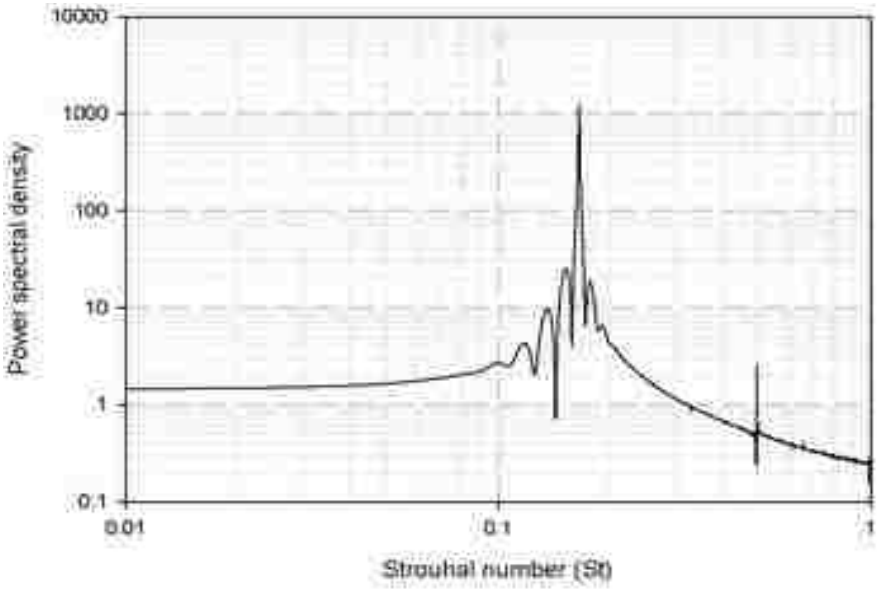

Figure 5.2. Fast Fourier Transform of the lift coefficient at *Re*=100

Table 5.2. Comparison of results for stationary cylinder at *Re*=100

	St	C_d	C_l
Stansby and Slaouti (1993)	0.166	1.32	0.35
Anagnostopoulos (1994)	0.167	1.2	0.27
Henderson (1995)	0.166	1.35	0.33
Zhou *et al* (1999)	0.162	1.48	0.31
Shiels *et al* (2001)	0.167	1.33	0.3
Present Study	0.166	1.378	0.35

The values of drag and lift coefficient along with the *St* is compared with previous numerical as well as experimental studies [85-88]. Figure 5.3 shows the St-Re curve where a comparison of our present numerical results is made with the universal *St* given by Roshko [85] and also with the new *St-Re* number relation given by Fey et al [87]. It is seen that the values of *St* are in very close agreement with the experimental results. However, as the flow approaches *Re*~200, the vortex shedding becomes 3-D and this leads to poor agreement with our computational results.

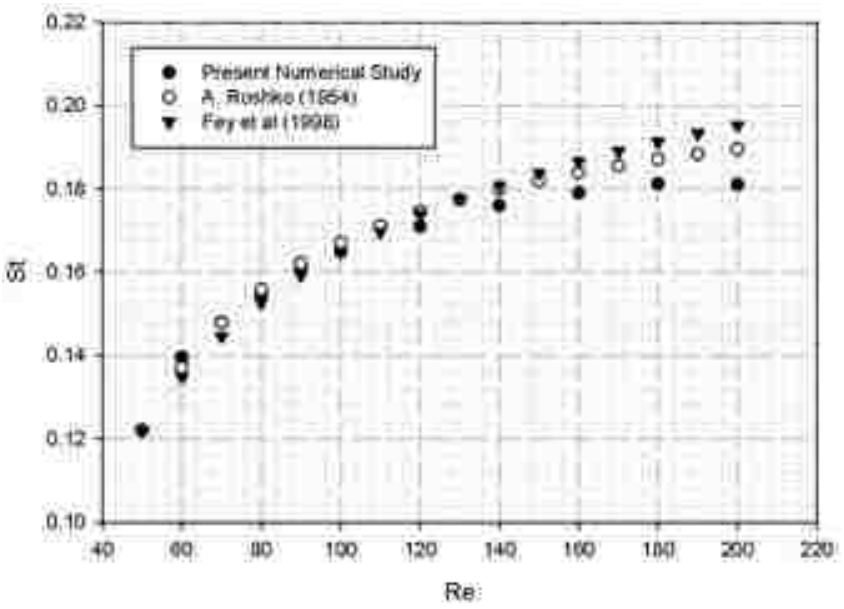

Figure 5.3. Comparison of obtained Strouhal number (*St*) with the *universal St* [85] and the new *St-Re* number relation [87]

The lift and drag coefficients are compared with results from Placzek *et al* [88] and Norberg [86]. It is seen that the mean drag coefficients decreases with *Re* while the RMS of the lift coefficient increase with *Re*. This is because at higher *Re,* the separation of boundary layer is less as compared to a laminar flow due to better adhesion. It is clear that our results are in very good agreement with previous studies [85, 87]. Figure 5.4 and Figure 5.5 show the average drag coefficient and the RMS of lift coefficient for different *Re* respectively-it is observed that our results match the data-sets of Placzek *et al* [25]

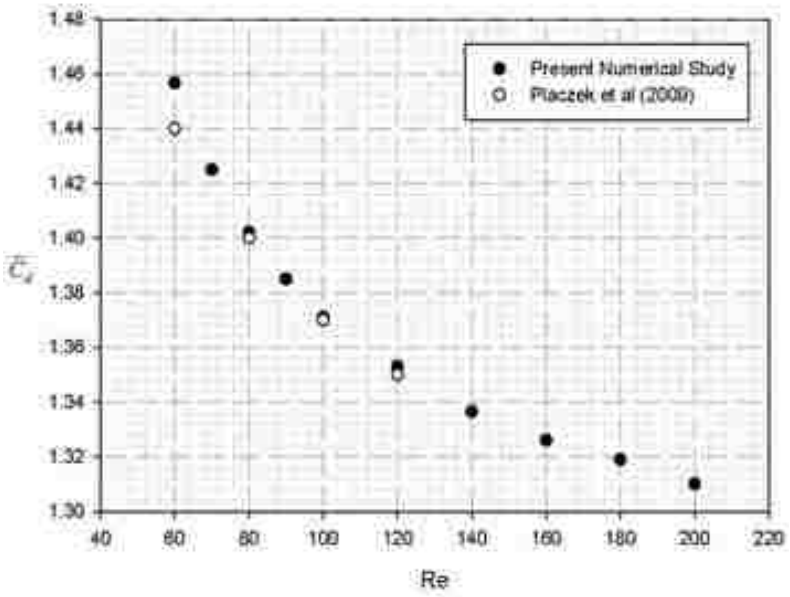

Figure 5.4. Average drag coefficients compared with numerical study [88]

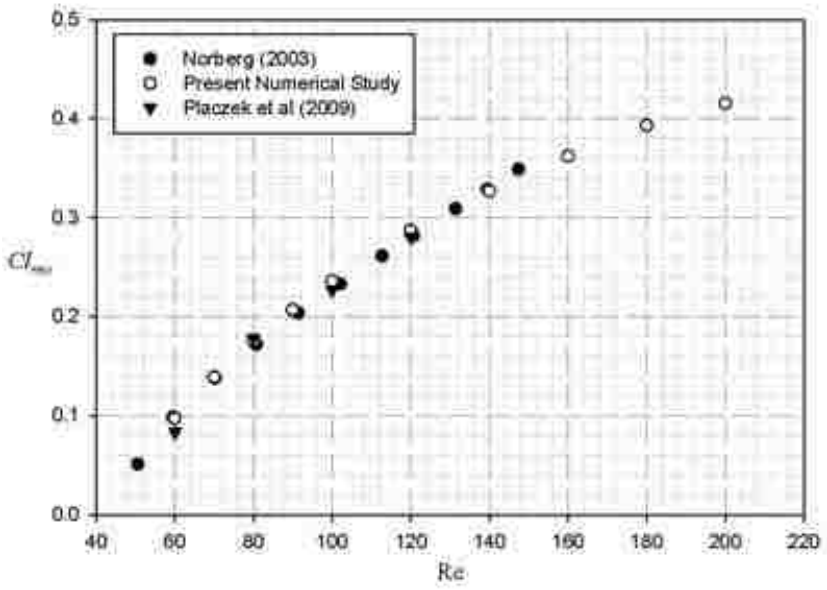

Figure 5.5. RMS of the lift coefficient compared with previous studies [88] and [86]

5.1.2 Validation of Numerical Simulation for a Moving Cylinder. An elastically mounted cylinder that is free to oscillate transverse to the flow is the most basic case for the subject of fluid-structure interaction (FSI) of bluff bodies. In this

section, we explore in depth the phenomenon of VIV and demonstrate the ability of our numerical scheme to simulate FSI. The cylinder is free to oscillate in the direction transverse to the flow, the amplitude and the frequency being an unknown unlike in forced vibration where the cylinder oscillates at predefined amplitudes and frequencies. Since the cylinder is constrained in the stream wise direction, the oscillating forces of lift causes it to vibrate in the transverse direction. This response (amplitude and frequency) of the system depends on the mass and the damping of the system given by the mass-damping parameter $\left(m^* + C_a\right)\zeta$. From previous studies [30] it has been seen that for a greater value of mass-damping, the response curve $\left(A^* vs U^*\right)$ obtained is restricted to a two-branch (see Figure 5.6) rather than a three-branch as seen in small mass-damping value systems. For a *Re* of 100, it is seen that the limiting amplitude reached for very low values of mass-damping is *A** ~ 0.6. Khalak and Williamson [44] in their experiments show that the maximum amplitude *A/D* reached is ~ 1.0 but at a higher *Re* in the range of 900-15000. This clearly demonstrates an effect of the *Re* on the amplitude of the system. It was also seen that for a *Re* as low as 100, the upper branch did not exist (see Figure 5.6). The low *Re* experiments from Anagnostopoulos were used as a validation case because the flow was inherently two-dimensional. It also seemed important to validate our case first at low *Re* before we proceed to higher *Re* flows. The physical parameters used in the simulations were selected to mimic experiments in Anagnostopoulos and Bearman [89]. The values used in the present simulations are listed in Table 5.3. Figure 5.6 shows comparison of present numerical simulation with the experiments of Anagnostopoulos [89].

Table 5.3. Parameters and corresponding values used in the present simulation

Parameters	**Units**	**Values**
Spring Stiffness (*k*)	*N/m*	69.48
mass (*m*)	*kg*	0.03575
Damping ratio ($\rho d^2 l/2m$)	-	0.00427
Reduced velocity (*U**)	-	5.0 - 8.0

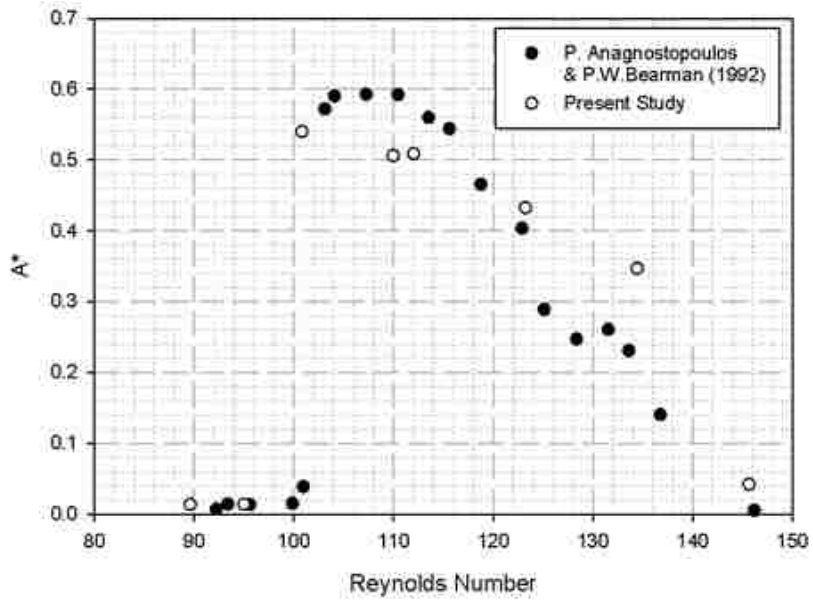

Figure 5.6. Comparison of experimental data [89] with numerical simulations

The simulation was initiated for a *Re*=90 and later the velocity was gradually increased to obtain higher *Re*. In a total, eight different simulations were run at different *Re* by varying the free stream velocity. The parameters for all the simulations were kept constant and given in Table 5.3. For *Re*=90 the vortex shedding frequency was lower than the natural shedding frequency i.e. the system is initially unlocked. As the *Re* was increased beyond 100, there was a sudden increase in the response of the cylinder (see Figure 5.6). This shows that the system is locked i.e. the vortex shedding frequency is equal to the natural frequency of the system. The amplitude of the system reached ~ 0.5 - 0.6 *d*. This buildup of the oscillations is seen in Figure 5.6 for both experiments performed by Anagnostopoulos [89] as well as the current numerical simulations. This lock-in exists until the *Re* ~ 125 after which there is a sudden drop in the amplitude. At this point the frequency of vortex shedding is greater than the natural frequency thus f^* is greater than unity. The phenomenon of lock-in is clearly seen in Figure 5.7. It can be seen that the frequency of vibration (f) and the vortex shedding frequency (f_{vo}) are in synchronization (i.e. $f/f_{vo} \sim 1$) between reduced velocities (U^*) of 5 to 7.

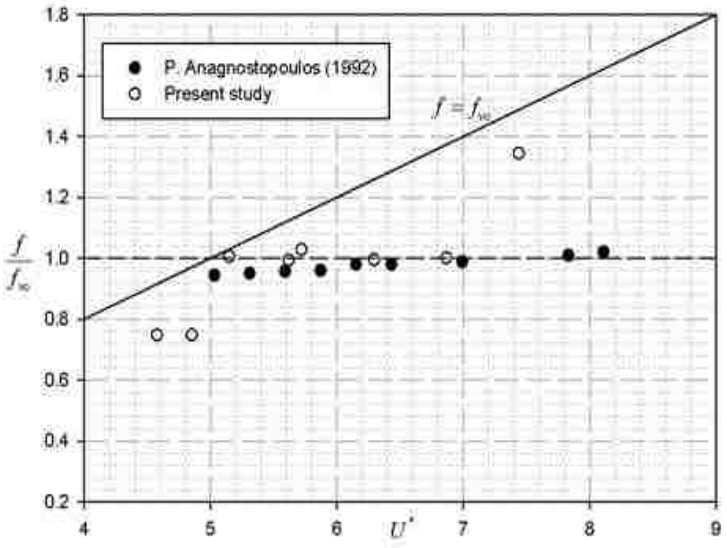

Figure 5.7. Frequency response from present experiments and numerical study

Vorticity contours were obtained at the maximum displacement corresponding to *Re* = 110. It is seen that the vortex obtained is in the 2S mode even when the amplitudes is at the max. This shows that the mode of vortex shedding in the upper branch is dependent on the *Re.* The 2*P* mode of vortex shedding is absent at lower *Re.* Figure 5.8 shows the presence of 2*S* mode at *Re* = 110.

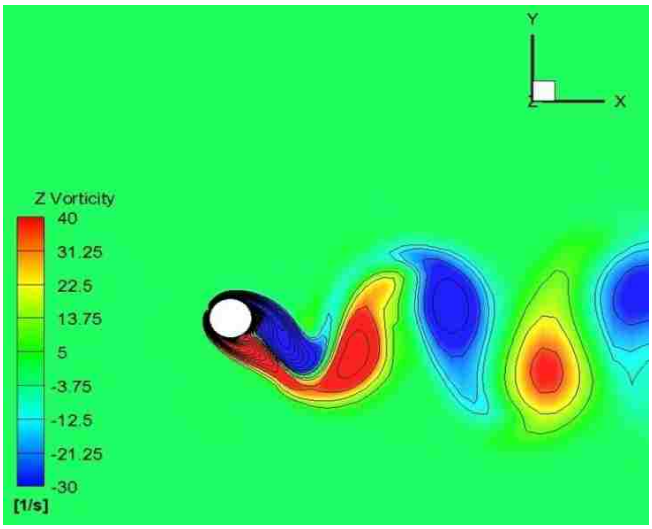

Figure 5.8. 2S mode of vortex shedding at *Re* = 110

In addition, our computational model was also tested for its accuracy and viability by eliminating the damping constant; the advantage being, governing equation contained only the mass and the spring stiffness term. This was done in order to study the behavior of the system in the absence of structural damping-a feature that is relevant to the VIV flow physics as the mechanical system is designed with low mass-damping. The effective spring stiffness plotted on the *x*-axis (see Figure 5.9 and Figure 5.10 below) is given by the Equation (5.1)

$$k_{eff}^{*} = k^{*} - 4\pi^{2} f^{*2} m^{*} \tag{5.1}$$

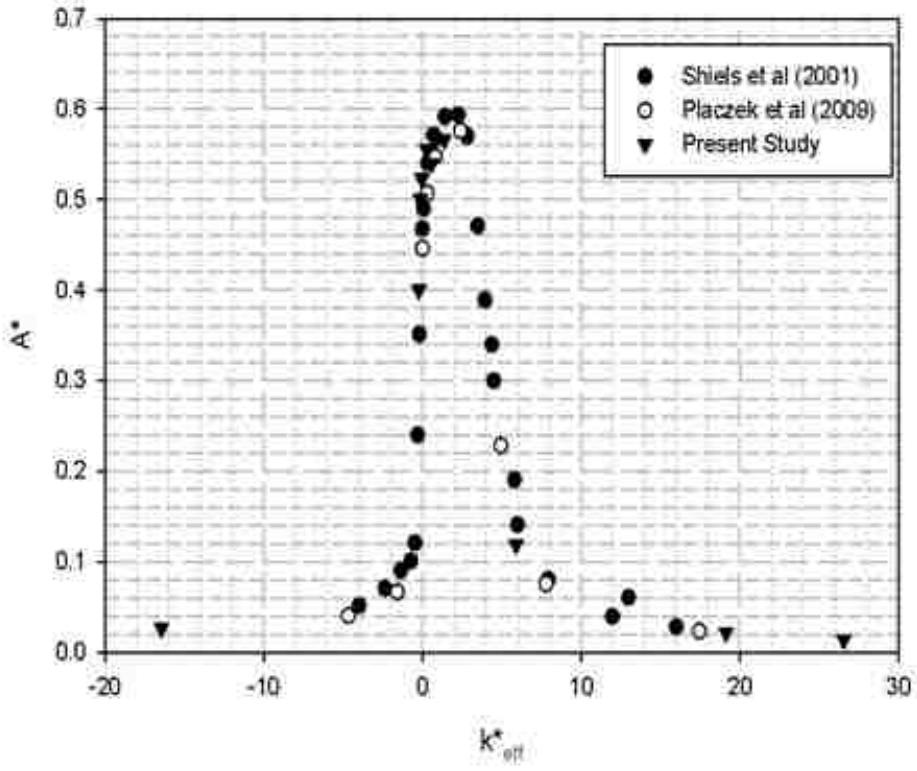

Figure 5.9. Non-dimensional amplitude plotted as a function of effective spring stiffness (k_{eff}^{*}) and it's comparison of with other numerical studies [37, 88]

It can be seen that maximum amplitude is achieved at k_{eff}^{*} value of ~ 0-5 which denotes the existence of resonance in that range of effective stiffness. This is clearly evident from the expression given in Eq (1). In the resonant zone the frequency of oscillation of the cylinder increases from the Strouhal frequency and reaches a steady frequency which is the natural frequency. Also we see that for a *Re* = 100, the maximum displacement achieved is ~ 0.6*d* even when the mass-damping value for the system is zero. This increase in amplitude can be attributed to the lock-in phenomenon where the natural frequency is in phase with the external excitation frequency. Figure 5.10 shows comparison of frequency response with varying effective stiffness. Results are compared with the numerical findings of Placzek *et al* [88] and Shiels *et al* [37] and our results are in good agreement. This proves the validity of our numerical study at zero damping.

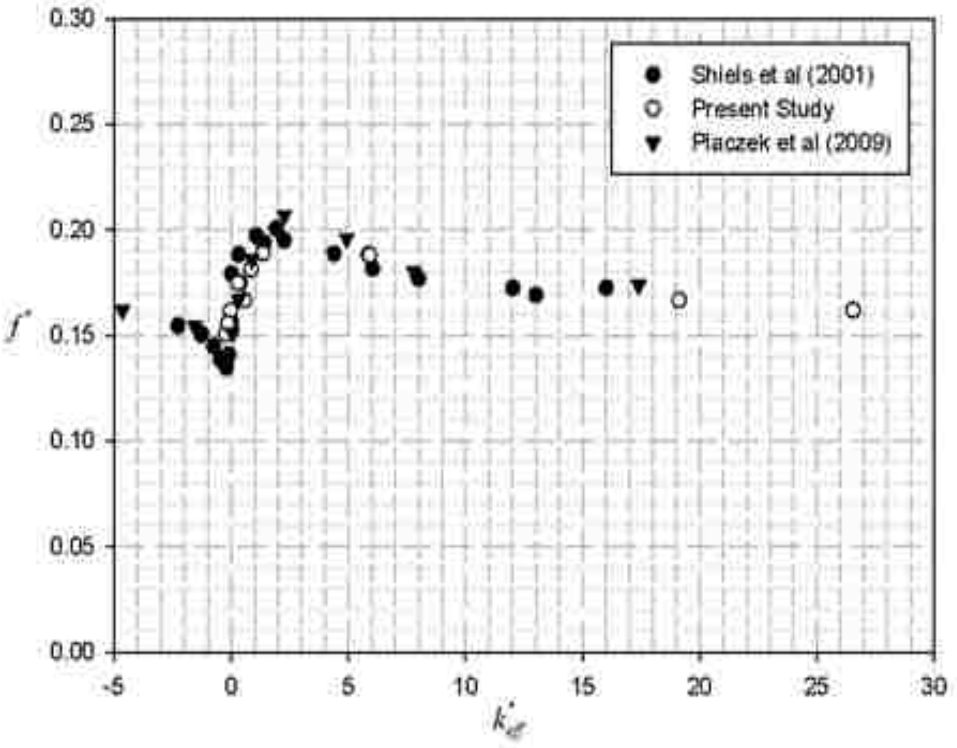

Figure 5.10. Non-dimensional frequency versus effective spring stiffness and its comparison with other numerical studies [37, 88]

To summarize, our simulations, with and without the mass-damping demonstrates that the maximum displacement persists up to a maximum of ~ 0.6*d*. Most notably, the displacement does not increase even if the damping is set to zero. This may be due to the fact that the vortex shedding mode obtained at low *Re* does not give a net energy transfer from fluid to body motion over one cycle, unlike the energy transfer in the 2P mode which is observed at higher *Re* [35]. Figure 5.11 shows the Griffin plot for the laminar regime i.e. *Re* < 200 with the present study plotted at *Re*=100. The results are compared with previous Direct Numerical Simulations [74, 76]. It is seen that as the mass-damping parameter is increased, the displacement reduces to zero which is an expected behavior. Also by extrapolating the data in Figure 5.11 we see that for zero mass-damping the max amplitude obtained is ~ 0.6*d* as seen previously (see Figure 5.9). This shows that irrespective of the absence of damping, the maximum displacement reached for a laminar flow is ~0.6*d*

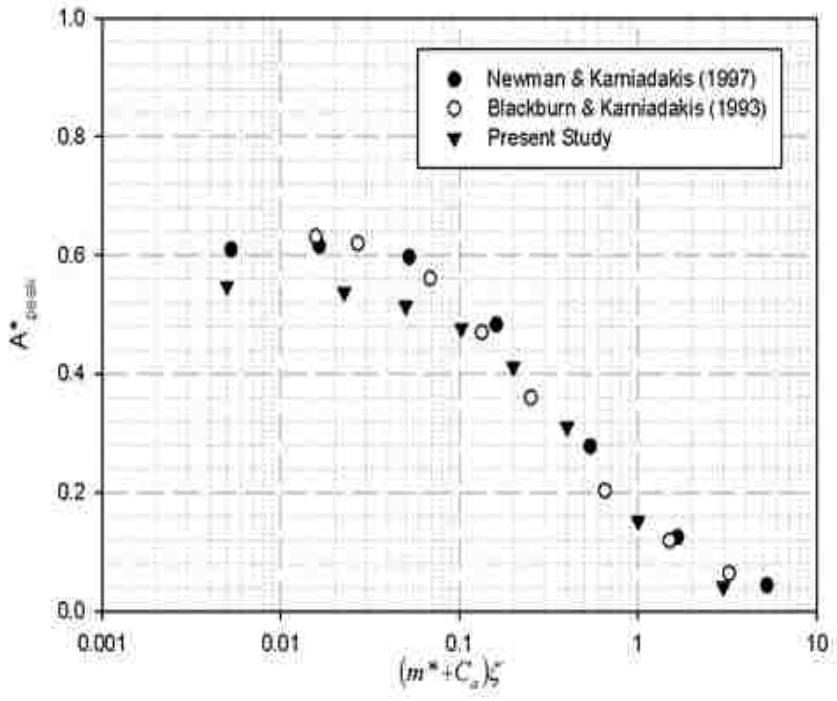

Figure 5.11. Comparison of peak amplitude response at *Re*=100 from present study with DNS at *Re* < 200 [74, 76]

5.1.3 Numerical Simulation of VIV of a Circular Cylinder with Low Mass Damping at a Higher Reynolds Number (1×104 < Re < 3.2×104). In this section a two-dimensional Reynolds-Averaged Navier-Stokes (RANS) equation equipped with *k-ω* Shear Stress Transport (SST) turbulence model is used to solve the phenomenon of VIV in a turbulent flow. The reason for selection of the *k*-ω based SST model is that it accounts for the turbulent shear stress transport and gives highly accurate predictions of the onset and the amount of flow separation under adverse pressure gradients. Also this model performs well in free shear flow and separated flows. Thus the SST model is recommended for high accuracy boundary layer simulations. The numerical result obtained in this study is compared with the results we obtained experimentally. It has been observed that for *Re* > 200, the flow in the wake becomes turbulent and this is followed by the existence of the 2-P mode. The span-wise correlation that exist at higher *Re* is an indicator of the three-dimensionality in the wake and might be related to the response of the cylinder especially the existence of the upper branch [64]. Thus it is important to understand how a system behaves numerically at a higher *Re* in a cross flow. Guilmineau and Queutey [71] studied the effect of initial condition on VIV using the *k-ω* SST model. They used different initial conditions to compare their results with the experimental results of Khalak and Williamson [43]. Depending upon the initial condition used they were able to match the maximum amplitude; however, their simulations were unable to accurately predict the upper branch. Pan *et al* [64] also performed RANS simulations using *k-ω* SST to explain the discrepancies between experiments and RANS simulations.

The range of Reynolds number used in the present study spans from 1×10^4 to 3.2×10^4 for a mass ratio (m^*) of 2.48, a total stiffness (K) of 84.089 N/m and a damping ratio (ζ) of 0.0157. The value of U^* ranged from 4.3 to 12.7. For all simulations the initial condition used was that all cylinders would reach steady state amplitude starting from rest. Table 5.4 list the various values of velocity used in the present simulation and its corresponding *A/d* ratio. Figure 5.12 gives the displacement obtained with the numerical simulation and its comparison with experimental values.

Table 5.4. Velocity and amplitude ratios used in the present simulation

	***U* (*m/s*)**	***A/d***
1	0.16	0.1865
2	0.18	0.524
3	0.2	0.552
4	0.2204	0.6174
5	0.2586	0.663
6	0.3302	0.71
7	0.3745	0.7148
8	0.46018	0.559
9	0.5485	0.0314

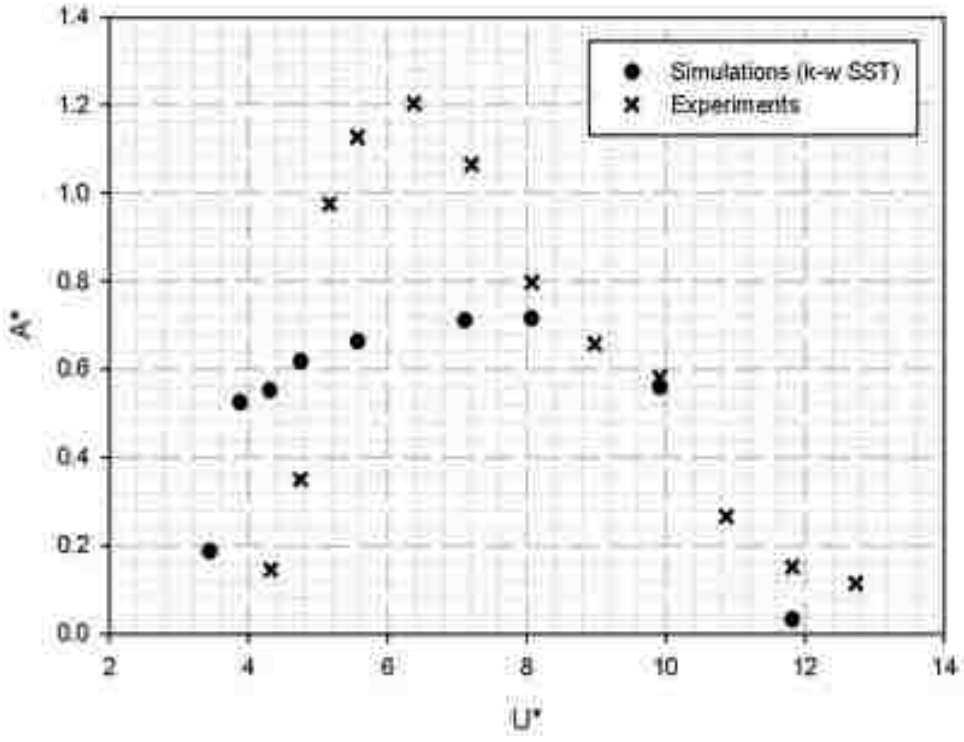

Figure 5.12. Non-dimensional amplitudes obtained from numerical analysis and its comparison with results obtained experimentally

It is seen that the upper branch could not be predicted using the numerical method moreover the transition from the initial to the upper branch in experiments is slightly delayed as compared to the numerical simulations. We attribute the loss of the upper branch in the present study to the two-dimensional assumptions of our simulation. The flow around the cylinder at the flow *Re* is three-dimensional and turbulent-such simulations would be computationally expensive and was not undertaken for the present work. It has been proposed that the existence of the upper branch is due to the irregular behavior of vortex shedding and span wise correlation that exist at higher Reynolds number [64]. In the present simulations we achieve a maximum value of A/d=0.71 which is very similar to values observed elsewhere [64]. In addition, reduction of the mass-damping to zero yielded no change in their results. This shows that the value of maximum amplitude achieved is only a function of the numerical technique used [64]. Figure 5.13 show the frequency response versus the reduced velocity U^*. It is seen that although the upper branch is difficult to predict, the frequency of vibration in the upper and lower branch are in close agreement (see Figure 5.13).

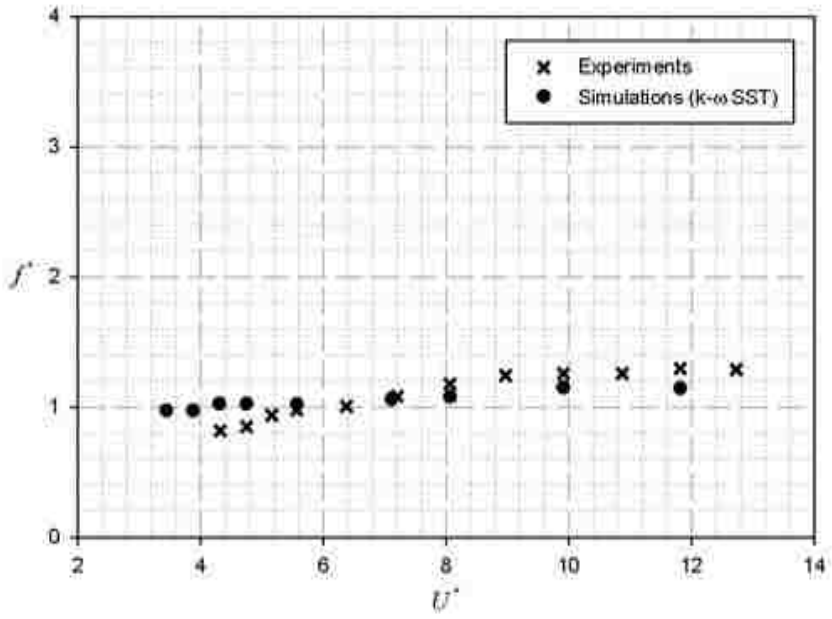

Figure 5.13. Frequency response versus reduced velocity for m^*=2.48 and ζ=0.0157

In the present study, a two-dimensional numerical study is being compared with an experiment in which the flow is inherently three-dimensional. For a three-dimensional simulation, the flow of fluid is always in perfect span wise correlation. Thus we can say from Figure 5.12 and Figure 5.13 that the presence of the upper branch is attributed to the existence of the irregular behavior along the span of the cylinder which exists due to three-dimensionality in a flow. In the frequency response plot (see Figure 5.13), these irregularities are distinctively seen in the initial branch as compared to upper and lower. This may be due to the existence of beat frequencies in the lower branch which causes an increase in the irregularities due to the presence of multiple frequencies that exist along the span of the cylinder. Also the span-correlation is greater at low mas-damping than at higher values of mass-damping.

Vorticity contours were also observed at $U = 0.3302$. This point corresponds to the upper branch as seen in the Figure 5.12. It is seen that although the simulations could not match the displacements seen in experiments, the 2P mode of vortex shedding was still observed in the upper branch. It is seen that the second vortex in each pair is weaker than the first one, as observed in various experiments and simulations. Figure 5.14 shows the existence of the 2P mode in the wake region.

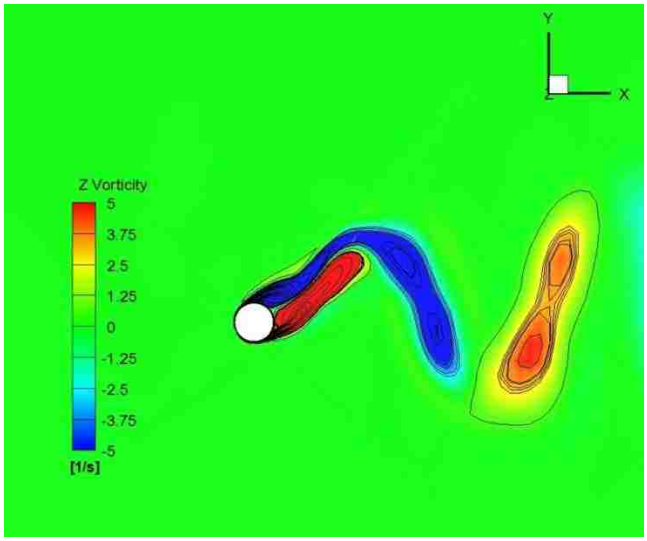

Figure 5.14. 2P mode of vortex shedding in the upper branch with the second vortex being weaker than the first

5.2 RESULTS FROM EXPERIMENTS

Next we discuss results from our experimental investigation to understand the basic physics of the response of an elastically supported cylinder immersed in water. Table 5.5 lists seven different cylinders with varying diameters and mass ratios that were used to study the amplitude and frequency response of a system undergoing VIV.

Table 5.5. Different diameter cylinders used in the present experiment and their respective mass and damping ratios

Cylinders	Diameter m	mass ratio m^*	Damping ratio ζ
1	0.01905	10.75	0.0105
2	0.0222	8.51	0.0113
3	0.0254	6.99	0.012
4	0.03175	5.17	0.0106
5	0.0334	3.925	0.013051
6	0.04826	2.48	0.0138
7	0.09525	0.47	0.023

5.2.1 Experiments for $m^* > m^*_{critical}$. The mass ratios were selected such that the existence of the upper branch would be clearly seen as we keep decreasing the mass ratio. This was done to study the amplitude and the frequency profile for a system with a wide range of mass ratios. We begin by looking at the non-dimensional amplitude versus the reduced velocity for mass ratios of 2.48, 3.925 and 10.75 using the traditional non-dimensional formulation given by Khalak and Williamson [43]. Figure 5.15 shows the existence of the initial branch, the upper branch and the lower branch as defined by Khalak and Williamson [44]. The amplitude response profile is slightly different from the traditional response shown in various literatures because of the presence of end plates. In all our experimental runs mentioned above, there were no end plates used (unless specified). Figure 5.15 and Figure 5.16 show the amplitude and frequency response of three different mass ratios (m^*=10.75, 3.925 and 2.48)

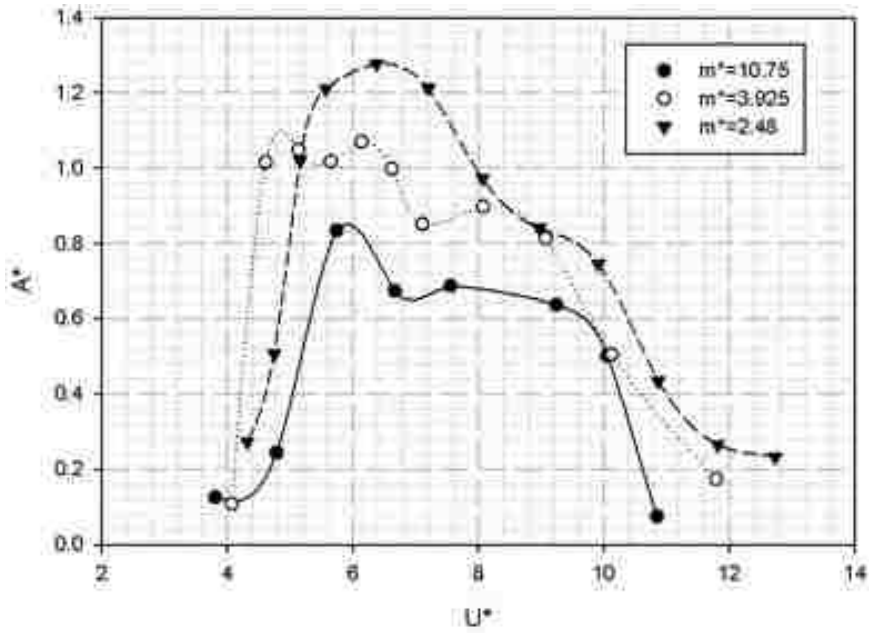

Figure 5.15. Amplitude response showing the traditional three branch response for low mass ratio of 10.75, 3.925 and 2.48

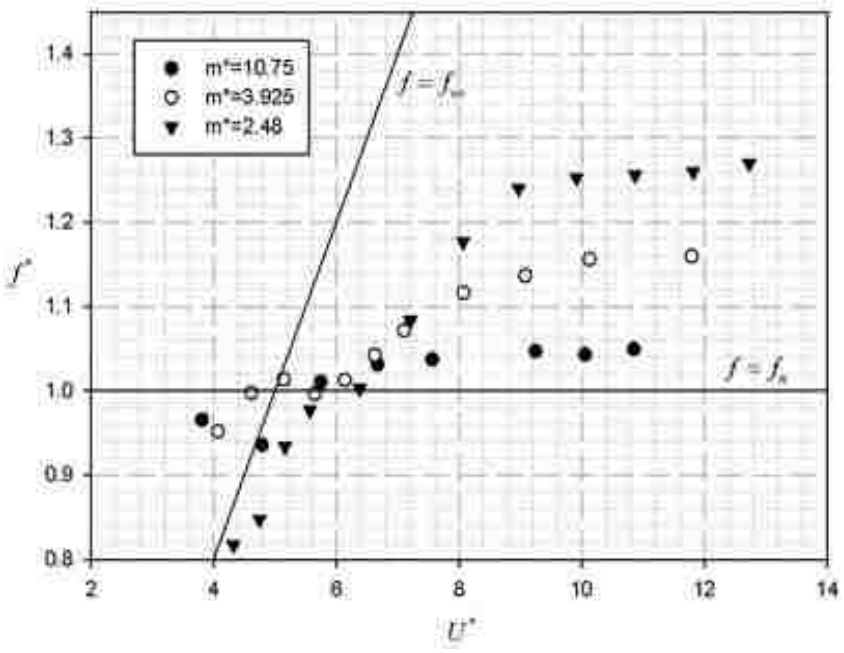

Figure 5.16. Frequency response plotted against reduced velocity showing constant lower branch frequency for *m** of 10.75, 3.925 and 2.48

From Figure 5.15 it is seen that the jump from the initial to upper branch is sudden while the jump from the upper to lower does not show this behavior. Also as the mass ratio is reduced, the maximum amplitude and the span of the entire response envelop keeps increasing. The amplitude keeps increasing until it has reached a max value of ~ 1.25*d*. This is the maximum amplitude that has been reported in any VIV related experiments known to us. As the mass ratio is reduced further, it is seen that the amplitude still remain fairly constant but the width of the upper branch keeps increasing (see Figure 5.15). Looking at the frequency response curve in Figure 5.16 we see a very different behavior at the upper and lower branch. It was always believed that maximum amplitude occurred only when the external exciting frequency is in phase with the natural frequency of the system, which is also popularly termed as the resonance period. But we see from Figure 5.16 that for low mass ratios frequencies, this is not the case. The lower branch remains fairly constant in the upper branch and above the natural frequency. That is the precise reason why for high mass ratios the lock-in frequency appeared very close to the $f=f_n$ line. Figure 5.17 shows constant frequency greater than the natural frequency in the lower branch for m^*=10.75, 3.925 and 2.48

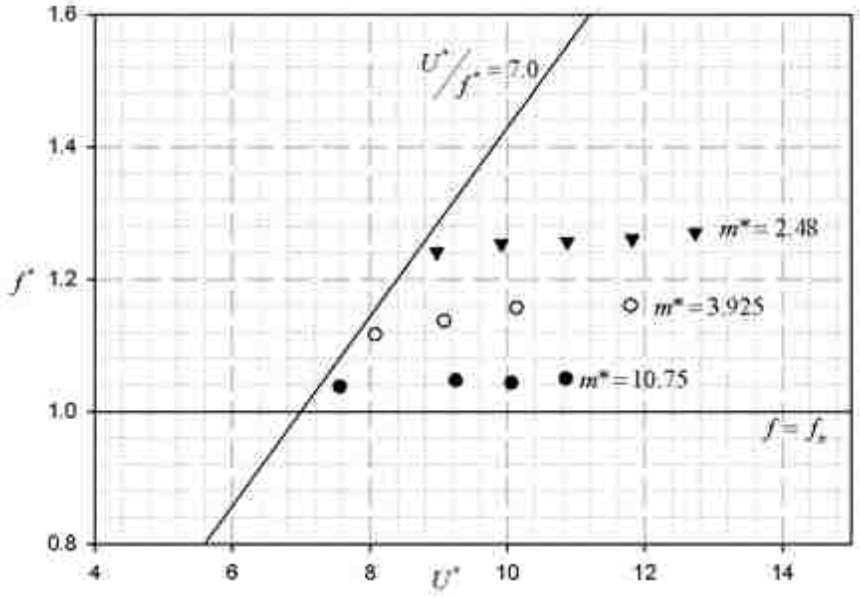

Figure 5.17. Constant lower branch frequency for mass ratios 2.48, 3.925 and 10.75

According to Govardhan and Williamson [59], the value of normalized velocity at the start of the lower branch is given by the relation,

$$U^*/f^* = 5.75 \tag{5.2}$$

In our experiments, we see a slight variation from what is reported in the literature. The lower branch frequency becomes constant for a relation given by $U^*/f^* \approx 7.0$ rather than the one shown in Eq (5.2). This slight deviation can be attributed to the absence of end plates in our case. This is seen as a characteristic behavior for an elastically mounted circular cylinder having low mass-ratio.

5.2.2 Experiments for m*<m*$_{critical}$. In the previous section we see that the amplitude of vibrations is found to be greater in the upper and the lower branch as compared to the initial branch. Thus we are interested in the behavior of the system in these two branches and its transition from upper to lower. Analysis of the frequency response plot (see Figure 5.16) shows that the jump from the initial branch to the upper branch or the start of the upper branch takes place at a $U^* \sim 5.0$ and travels along a straight line until it becomes constant. This constant frequency marks the frequency of the lower branch for a particular mass ratio which can be seen in Figure 5.17. Govardhan and Williamson [59] in their experiments found that if the mass ratio was reduced below 0.54, then the lower branch ceases to exist and the upper branch extends indefinitely. This mass ratio is called the critical mass ratio ($m^*_{critical}=0.54$). Thus for a system with a mass ratio below critical mass, the system always vibrates in the upper branch. For maximum power generation, it is important to have greater amplitudes and frequency of vibration. This was a unique discovery that led us to the design of our system. In the present study, we perform an experiment with cylinder for $m^*=0.47$ having diameter $d=0.09525$ m (3.75 inch) to investigate the existence of critical mass. Figure 5.18 and Figure 5.19 show amplitude and frequency comparison of a system with mass ratios 0.47 and 10.75

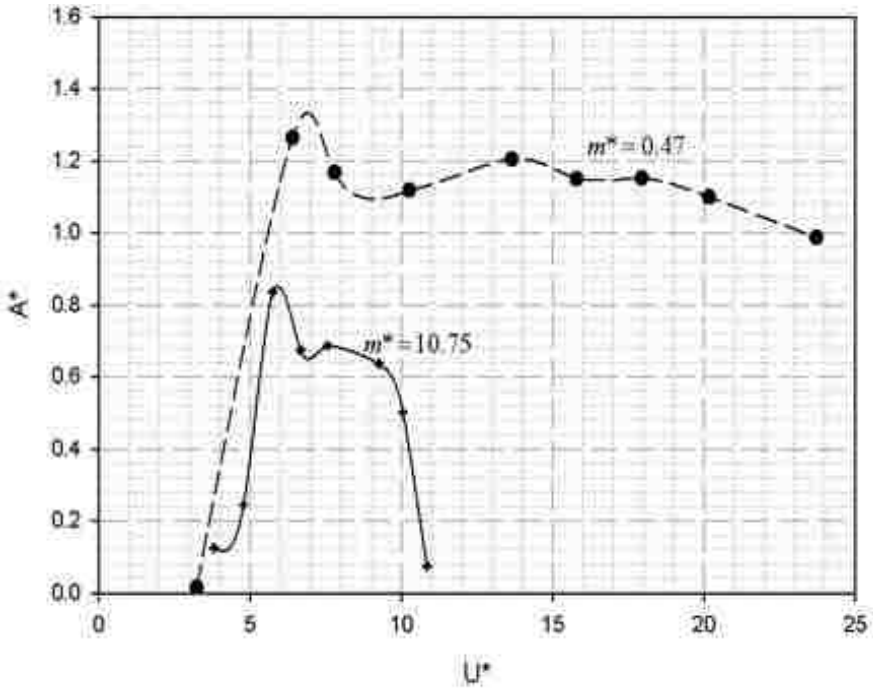

Figure 5.18. Comparison of amplitude response plot for values of m^* greater than and less than the critical value (m^* = 10.75 and 0.47 respectively)

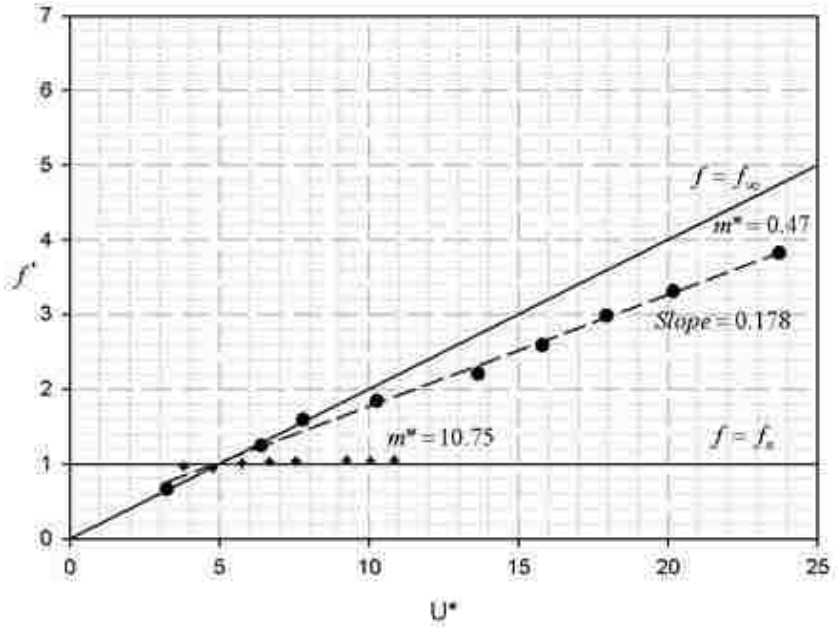

Figure 5.19. Frequency response plot showing constant lower branch frequency for m^* = 10.75 and the extended upper branch for m^* = 0.47

It is seen that the regime of synchronization is large with mass ratio 0.47 as compared to 10.75. For m^*=0.47 the upper branch extends up to a U^* of ~24. At this reduced velocity, the frequency of oscillation is ~ 4 times the natural frequency in water as seen in Figure 5.19. This similar behavior was also observed by Govardhan and Williamson [59]. The line on which the frequency data lie has a slope of 0.178 (see Figure 5.19) and has a positive intercept on the y-axis. The slope of the line defining the start of the lower branch (see Eq (2.4)) is also 1/5.75 ~ 0.178. Since both the lines have equal slope, they are parallel and will never intersect each other. In other words, the lower branch does not exist and the upper branch extends infinitely. Thus it is seen that for a mass ratio of 0.47, the upper branch does not exist which is in agreement with the experiments performed by Govardhan and Williamson [59].

5.2.3 Effect of an End Plate on VIV of Circular Cylinders. In the present section we have studied the VIV response of circular cylinder with and without an end plate. This end plate is rectangular in cross section with 0.0254 m (1 inch) thickness and is made of plexi-glass. The distance between the cylinder end and the end plate was ~ 0.0787 inch (2 mm) and kept constant for all runs. The end plate is unattached to the cylinder but fixed firmly to the bottom wall of the water tunnel test section. The following figure gives a schematic of the end plate arrangement.

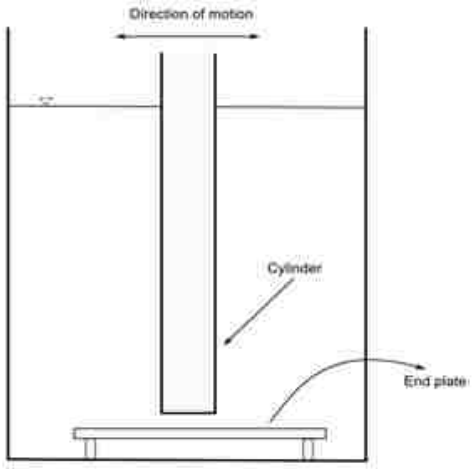

Figure 5.20. Schematic of end plate fixed to the bottom of the test section wall (flow of water is in the direction normal to the page)

Khalak and Williamson [43] in their study showed the effect of end plates on static cylinder and also performed flow visualization using hydrogen bubbles. It was seen that the cylinder with a free end, the shedding of vortex is oblique as compared to cylinder with end control. Also from force measurements it was observed that for parallel shedding, the RMS of lift coefficient was greater than that of cylinder with oblique vortex shedding. Thus for a freely vibrating cylinder it was expected that with an end plate, the amplitude of vibration would be greater as compared to a system without the end plate because of greater lift force. But after the experiments were performed, the results obtained were unexpected. For a system with the end plate, the amplitude of vibration was lower than the one without the end plate for an entire range of the upper and lower branch. The peak amplitude was almost the same for both cases and there was not much difference in the frequency response. Figure 5.21 and Figure 5.22 show the amplitude and the frequency response of a freely vibrating cylinder with and without the end plate.

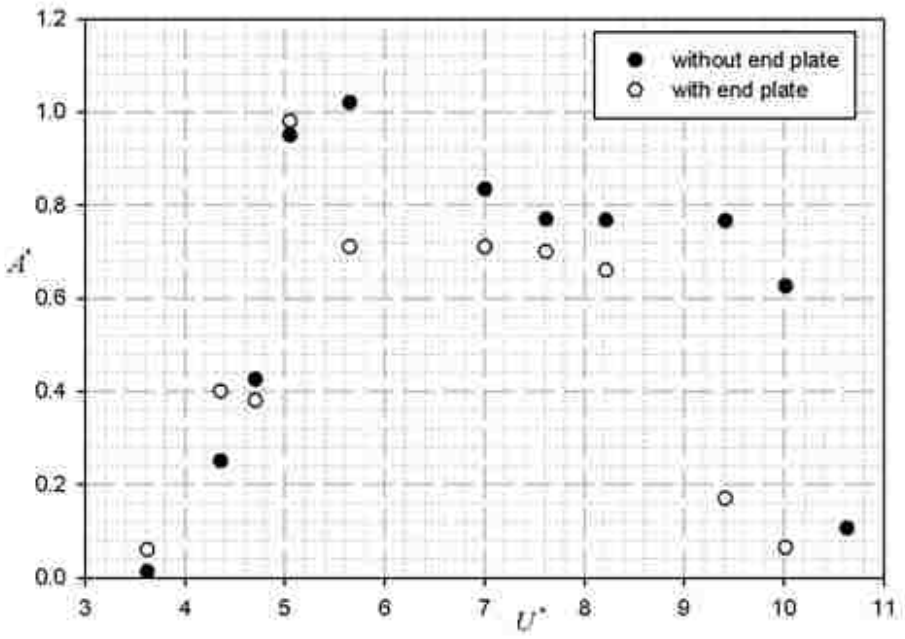

Figure 5.21. Amplitude response of VIV of a cylinder with and without an end plate for m^*=6.99

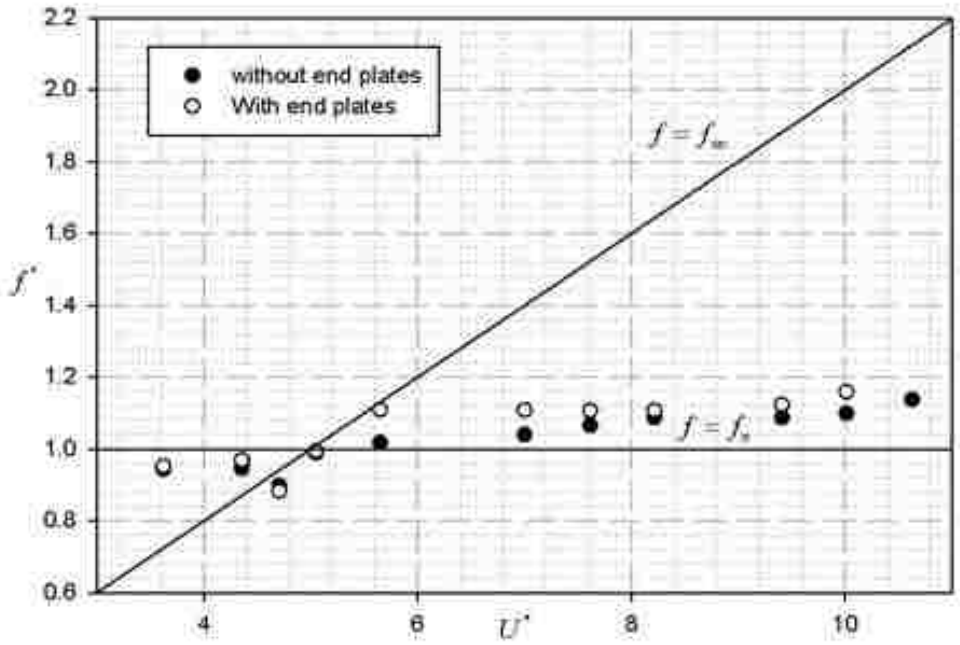

Figure 5.22. Frequency response of VIV of a cylinder with and without an end plate

We observe the displacement time trace at the start of the upper branch. For the case with the end plated attached, it was seen that the displacement time trace showed some irregularities in the peak displacement (see Figure 5.23). The peak displacement was never close to being constant with some variations. This behavior was expected because of the unsteady and transient nature of the problem but when the end plate was removed the result obtained was surprising. The unsteadiness in the displacement time plot disappeared with almost constant peak displacements throughout (see Figure 5.23). This behavior could be attributed to the fact that by removing the end plates, the level of span-wise excitation force is increased thus causing increased amplitude ratios. This peculiar behavior was also reported by Morse *et al* [90]. Figure 5.23 gives the displacement-time trace comparison for a system (m^*=6.99) with and without an end plate connected.

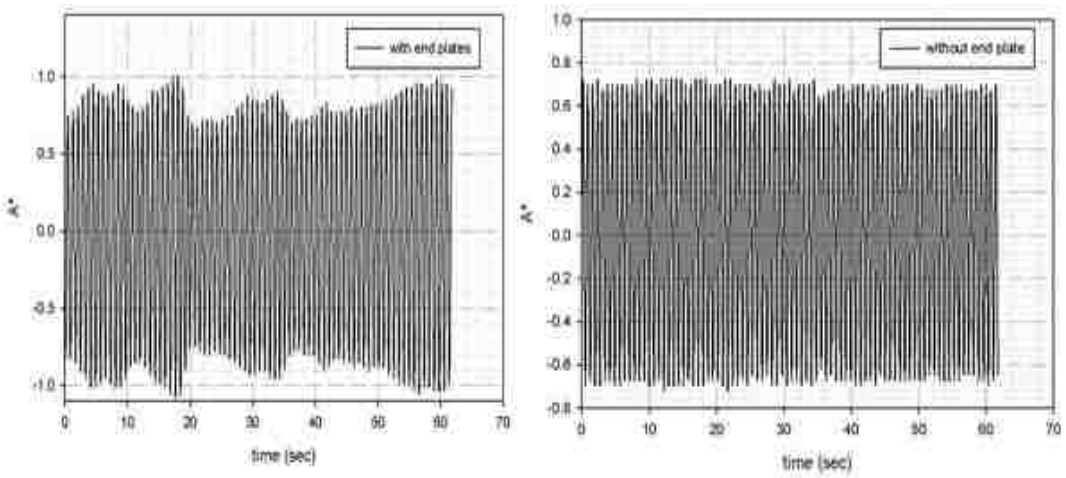

Figure 5.23. Displacement-time trace comparison with and without an end plates

Since there was a change in the amplitude response of the system with m^*=6.99, we found it interesting to check for similar behavior at a mass ratio of 0.47 which is less that the critical mass ratio. Thus similar experiments were also performed for $m^* < m^*_{critical}$. These results were compared with the results obtained without the end plate for m^*=0.47. Figure 5.24 and Figure 5.25 show the comparison of the amplitude and the frequency response, with and without the end plate at m^*=0.47

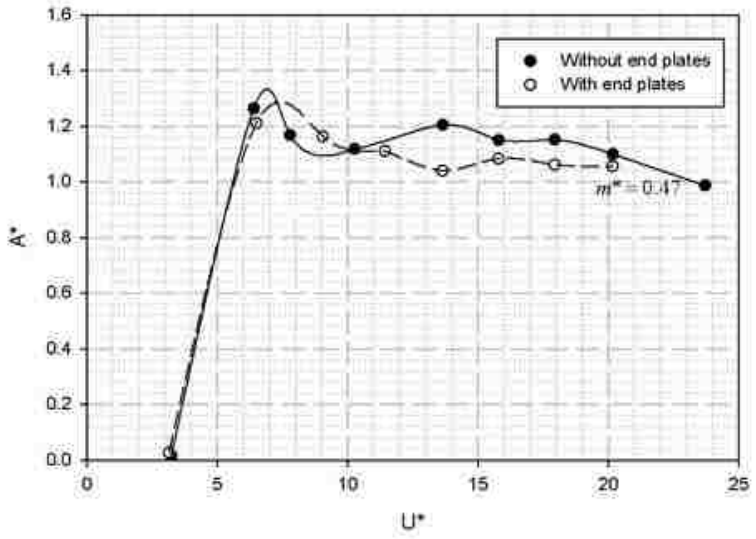

Figure 5.24. Comparison of amplitude response for m^* = 0.47

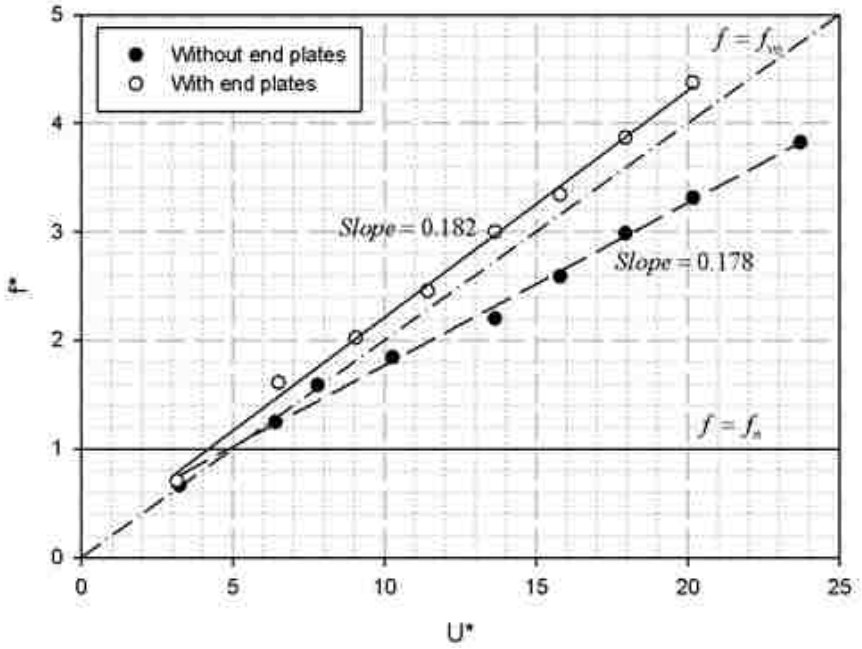

Figure 5.25. Comparison of frequency response for $m^* = 0.47$

From Figure 5.24 it is observed that even at a mass ratio below the critical value, the envelope of the amplitude response for a system without the end plate is greater than that for a system with the end plates. This behavior is similar for $m^* > m^*_{critical}$. Thus we can see that the effect of the end plate is independent of the mass ratio of the system. For the frequency response, the slope of the upper branch line (see Figure 5.25) obtained for the system without the end plate is slightly less than the one obtained with the end plate. Although the slopes of both lines are different, they still do not intersect the line which marks the starting of the lower branch frequency (see Eq (5.2)). Hence we can summarize that the present energy generator will have no end plate present, as this would give higher amplitudes for the upper and the lower branch of amplitude response.

5.3 DESCRIPTION OF THE PROPOSED POWER TAKE-OFF SYSTEM

The type of generator selected for energy harvester described in this study is called as TL-IPM **(**tubular linear interior permanent magnet generator). The architecture is a tubular linear interior permanent magnet generator (TL-IPM) [91] connected to a power converter as shown in Figure 5.26.

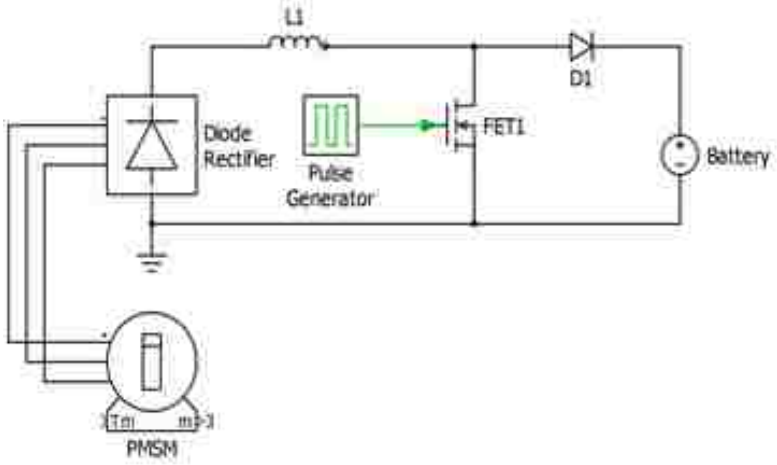

Figure 5.26. Simplified schematic for energy harvesting

A linear generator was chosen to minimize mechanical components, such as gears or cams. It has two main portions: a stator and a translator (also called slider or mover). The translator takes the place of the rotor in a conventional rotating machine and houses the permanent magnets. The translator could either occupy the inner or outer diameter of the tubular structure. For our application, the translator occupies the inner section and the stator occupies the outer diameter. Figure 5.27 shows the planned TL-IPM

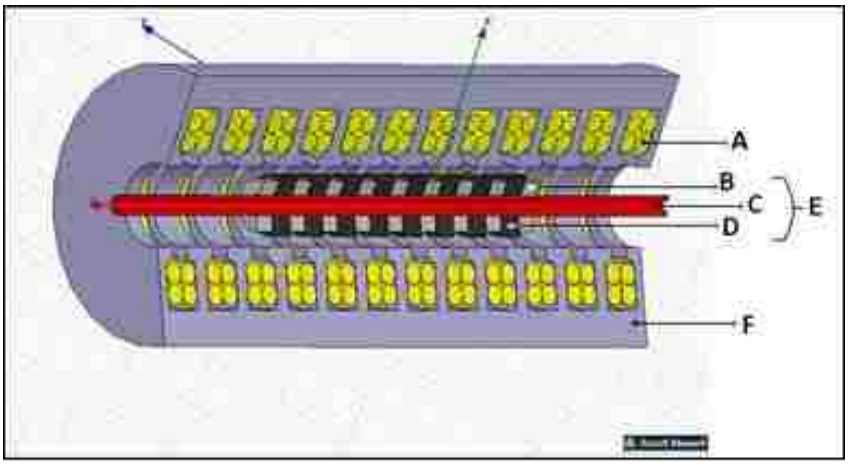

Figure 5.27. Proposed TL-IPM. The parts (labelled) consists of: A. Coil Windings; B. Ferromagnetic Material (e.g. Iron); C. Support Tube; D. Permanent Magnet; E. Translator; F. Stator

There are two topologies of linear generator design, long translator type and long stator types [92]. Following the notation of [91], a Θ type machine has a long stator that completely encloses the translator and a Ξ type machine has a long translator that exits the stator. Given the relatively slow motion of the translator, a better performance (high power density, high efficiency) configuration is preferred. From the efficiency of the machine point of view, the long translator would be the better choice. However, there is a severe mass constraint for the moving portion in the VIV system, so we have chosen the Θ (short translator, long stator) configuration. The coil windings within the stator are supported by sleeves or placed inside slots. Hence, the other 2 variants of the linear generator include an air-cored stator (slotless) and an iron-cored stator (slotted) [93]. Each variant comes with its advantages and drawbacks. The magnetic field produced by the PMs results in significant attraction between the translator and stator which must be withstood by the mechanical tubular structure [94] of the take-off system. Significant structural savings can be made if these cogging forces can be reduced or eliminated, which can be achieved by having a stator which contains no iron (air-cored), which is a simpler and cheaper construction option. In the iron-cored stator, magnetic flux generated by the PMs in translator is more concentrated inside the windings. This results in a significantly higher field density resulting in a higher induced voltage per translator stroke compared to the air-cored configuration [93]. Again, because the mass of the translator (and therefore the available magnetic material) is severely constrained, the slotted variant has been chosen. The main flux direction in the translator is determined by the magnetization of the PMs. With both radial and axial magnetization, ferromagnetic materials are generally required to guide the desired flux paths [95]. Both have been found to produce harmonic content, with the axially-aligned buried magnets producing very low harmonic content with suitable flux levels and radially-aligned buried magnets having slightly more harmonics [30]. To minimize harmonics and cogging forces, the proposed design uses axially-aligned buried magnets, as shown in Figure 5.28

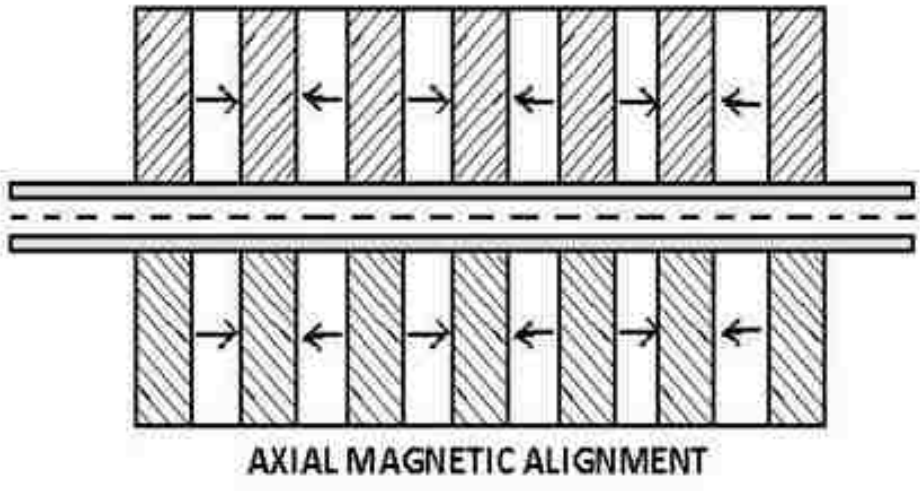

Figure 5.28. Translator with axial magnetic alignment, indicating magnet polarities

We have chosen neodymiumiron boron (NdFeB) magnets because of their high reminisce and coactivity. This design was driven by two main considerations: force vs. displacement and translator mass. Figure 5.29 below shows the dimensioned drawing of the proposed TL-IPM.

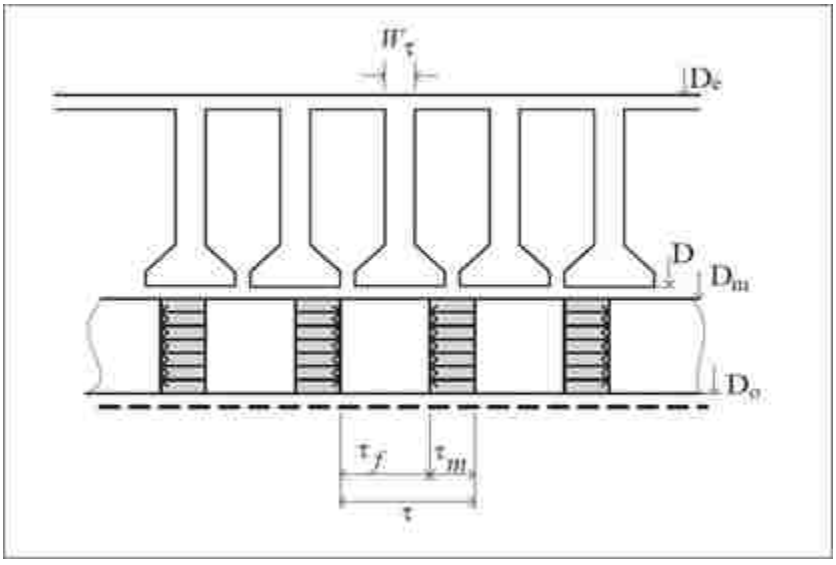

Figure 5.29. Dimensioned drawing of TL-IPM (as adapted from Bianchi *et al*.)

The boost converter is controlled as in a power factor correction circuit. The current is proportional to the rectified voltage, and the proportionality constant (conductance, G=1/R) determines the effective damping that the machine provides. This is conceptually similar to the resistor emulation approaches in [64, 96], the emulated resistance R_{em} of a boost converter in discontinuous conduction mode is

$$R_{em} = \frac{2LT}{t_{on}^2}\left(\frac{V_{out} - V_{in}}{V_{out}}\right) \tag{5.3}$$

where L is the inductance, T is the switching period, t_{on} is the on-time of the controlled switch, and V_{out} and V_{in} are the output and input voltages, respectively. The input power is then V_{in}^2 / R_{em} which is equivalent to a damper in the mechanical system. The optimal value of R_{em} is unknown a priori. A maximum power point tracking technique, as used for solar power [97], will be used to determine the optimal R_{em}. The most promising approach is perturb and observe.

5.4 PRELIMINARY RESULTS

From the above numerical simulations and experiments it is seen that even for *Re* number as low as *Re*=100 there is a possibility of power output. VIV based generator is known to operate in slow moving streams where other devices like water turbines cannot operate. This is the major advantage that a VIV based energy generator holds over all other types of energy harvesters. The average power and the peak force acting on a cylinder for the proposed system are given by the following expression, where *C* is the damping constant in *N-s/m, f* is the frequency of vibration and *A* is the amplitude of vibration of the cylinder.

$$F_{Peak} = AC\pi f \tag{5.4}$$

$$P_{avg} = F_{Peak}^{2} \Big/ 2C \tag{5.5}$$

Table 5.6 gives a list of all the different mass ratios and the damping constants used in the experiments to give an estimate of power that could be generated.

Table 5.6. Estimate of power output in Watts from present experimental runs

mass ratio	**Damping Ratio**	***frquency ratio***	***Amplitude ratio***	**Power**
m*	ζ	***f****	A^*_{max}	***W***
10.75	0.0105	1.102	0.8348	0.00046
8.309	0.0093	1.1	0.8075	0.00028
6.69432	0.01064	1.115	0.8683	0.00131
5.1706	0.00852	1.006	1.002	0.00131
3.925	0.01244	1.159	1.107	0.00294
2.48	0.01562	1.29	1.277	0.0117
0.47	0.023	3.82	1.099	0.316

It should be realized that the power output is low mainly due to the size constraints of the cylinder size used in the present prototype. Also if the mass ratio can be reduced below the critical value of 0.54, the frequency of vibration can reach up to thousand times the natural frequency thus increasing the power output tremendously.

6. CONCLUSION AND FUTURE WORK

6.1 SUMMARY

The main objective of the current study is to derive design guidelines for a VIV generator by optimizing the VIV process. The vortex based energy harvesting system mentioned in the present study is expected to be more robust and modular than VIVACE. To do this, a computational model was developed in ANSYS 13.0 to derive the initial design guidelines. This model was validated for a number of *Re* using both, experiments as well as simulations. To begin with, a flow over a stationary cylinder was first validated in the range of $50<Re<200$ when the flow in the wake is still laminar and two-dimensional. These results were validated with other experiments and simulations. This was done to check for the accuracy of our simulations when no mesh motion was employed. Simulations were then performed for VIV of cylinders at a low Re to understand the basic phenomenon of VIV such as the lock-in phenomenon, effect of damping, maximum amplitudes, and the existence of beat frequencies prior to lock-in. In these simulations the motion of the cylinder in a cross flow were not known a priori and the response was governed by flow of fluid and the system characteristics such as the mass, spring stiffness and the damping constant. The results were compared with the experimental findings of P. Anagnostopoulos and P.W Bearman [89]. The VIV response was also studied at $Re=100$ with zero structural damping and results were validated with numerical study of Shiels *et al* [37] who used a high-resolution viscous-vortex method and with Placzek *et al* [88] who used the finite volume method. These results were then plotted using the new effective stiffness formulation provided by Tony Leonard and Anatol Roshko's group at Caltech. The numerical findings from the present study showed good agreement with the experiment as well as other numerical studies. Simulations were also performed for higher *Re* ($1\times10^4<Re<3.2\times10^4$) flow using the k-ω SST turbulence model. The results from the numerical study was compared with our experiments at $m^*=2.48$ and $\zeta=0.0157$. The following are the findings from the present numerical study:

(a) There is an absence of the upper branch as well as the 2-P mode of vortex shedding in VIV of circular cylinders at low *Re* flows ($Re<200$)

(b) Beating behavior of frequencies is observed at vibrating frequencies lower than the systems natural frequency.

(c) For low *Re* at lock-in region, the frequency ratio is close to unity which is not the case at higher *Re* and low mass ratio.

(d) At low values of mass-damping and at *Re*=100, the maximum amplitude reached is ~0.6*d*. This is true even if the structural damping was reduced to zero.

(e) The maximum amplitude reached at higher *Re* ($1\times10^4<Re<3.2\times10^4$) using the *k*-$\omega$ SST turbulence model is ~ 0.7*d* whereas in the experiments the max displacement reached was 1.2*d*. Thus the maximum amplitudes reached in experiments were higher than that obtained from simulations.

(f) Vorticity contours in the wake region showed 2P mode in the wake region at *Re* ~ 18000. This signifies the presence of the upper branch. This absence of amplitude difference between simulations and experiments in the upper branch is attributed to the span-wise correlation and random disturbances that is defined by the three-dimensionality in a flow.

Based on the preliminary CFD design and guidelines, an experimental unit was also built to study the response of VIV of circular cylinders and to estimate the amount of power that could be generated from a single cylinder prototype. Various experiments were performed using different diameter cylinders having different mass ratios. The mass ratios ranged from 0.47 to 10.75. The following is a summary of the findings from the experimental studies

(a) As the mass ratio is reduced the span of the upper branch kept increasing. Six different mass ratios ($m^*>m^*_{critical}$) were used to study the amplitude response and the frequency response of the system. It was seen that irrespective of the mass ratio and the damping of the system, the maximum amplitude reached in the upper branch was never greater than ~1.2*d*

(b) Although there was no difference in the maximum amplitudes, the frequency response showed remarkable increase in the frequency ratio at the lower branch. It was seen that as the mass ratio was reduced, the lower branch frequency which is almost constant for a particular mass ratio kept on increasing. Thus in the lock-in

region, the frequency of oscillation was much above the natural frequency of vibration.

(c) The critical value for a mass ratio below which the lower branch ceases to exist is 0.54. At this mass ratio the upper branch continues to extend infinitely. Experiments were thus performed at a mass ratio of 0.47 which is below the critical mass ratio value. It was seen that the amplitude in the upper branch continues to grow along a straight line having a constant positive slope. This slope was equal to the slop of the line that defines the start of the lower branch given by Govardhan and Williamson. Thus this proves that for a mass ratio of 0.47 the frequency in the upper branch does not intersect the line which marks the beginning of the lower branch. Thus the upper branch extends infinitely. This finding is very unique because with such a VIV generator having a mass ratio less than critical, the amplitude obtained will always be maximum and thus the power output.

(d) Experiments were also performed to understand the effect of end plates. It was seen that without an end plate the max amplitudes obtained was very much stable with little variation as compared to a system with an end plate. Also the amplitudes obtained without the end plates were greater as compared to the case with an end plate.

(e) There was almost no variation in amplitude for a system at m^*=0.47 with and without the presence of an end plate. The maximum amplitude continued to be ~1.0*d*. The only difference that was seen was that the slope of the line defining the frequency of the upper branch was slightly greater than the one stated by Govardhan and Williamson.

6.2 FUTURE WORK

Current study includes numerical as well as experimental study of VIV of circular cylinders for a wide range of Reynolds number but with a single cylinder arrangement. The future work on VIV based electrical generator could include the following:

- **Fluid Dynamics.** Although we were unable to predict the maximum displacements in the upper branch using the *k-ω* SST turbulence model at high Reynolds number, it could very well approximate the frequencies of oscillations. Also the different modes of vortex shedding at the lower (*2S* mode) and the upper branch (*2P* mode) could be well predicted. In the future, this turbulence model could certainly be used to investigate the behavior of multi-cylinder arrangements. To obtain a large amount of power it would be necessary to have a VIV generator with a multi cylinder arrangement system in the near future. Future work in numerical analysis would include simulation of multi cylinder arrangement i.e. tandem and in-line arrangement. It would be important to study the effect of one cylinder in the wake region of another. This wake interference can be used to place the cylinders in such an arrangement that vortex shedding from the cylinder in the upstream will either enhance the vibration of other cylinders placed in its wake or have null effect. The schematic of few different arrangements possible is given in Figure 6.1

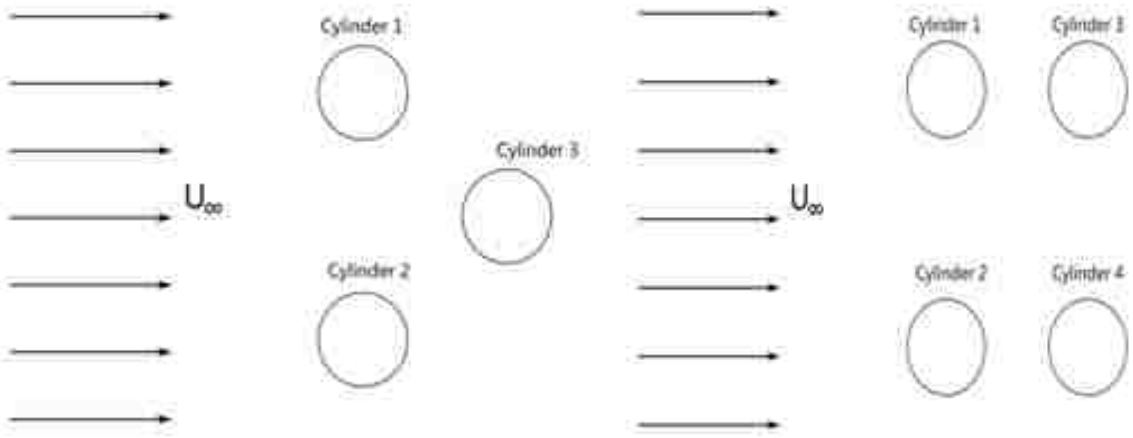

Figure 6.1. Positioning of cylinders for multi cylinder arrangement

In the above schematic arrangement of cylinders, the distance between the cylinders can be varied in the horizontal as well as the vertical direction to figure out the best possible arrangement for maximum power output.

- **Integration of power unit with the current set-up.** The current experimental set-up did not include the power take-off system (PTO). Future work would include the integration of the mechanical system with the electrical generator. Future work would also include building a VIV energy generator module with multi-cylinder arrangements for maximizing the power output. Forces of attraction between the translator and the stator due to the presence of magnets on the translator are very high. Preventing the magnets from clinging to the inner surface of the stator would thus be a challenging task. Future work could also include the design of a linear rail system that would coincide the axis of the magnets with the axis of the stator thus minimizing the forces of attraction.

APPENDIX A.

VIV EXPERIMENTAL SET-UP SCHEMATIC

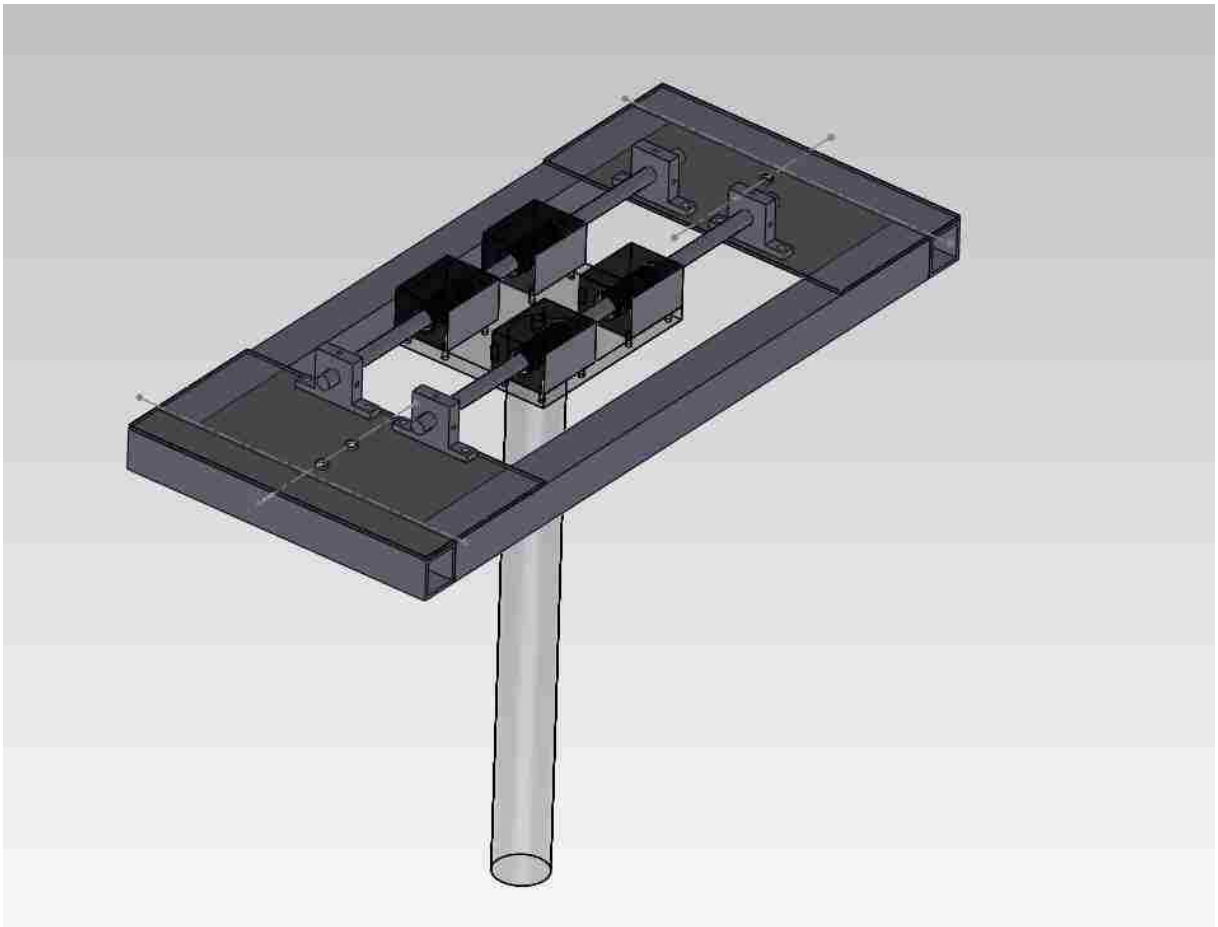

Figure A – 1. VIV schematic

APPENDIX B.

CYLINDER TRACKING CODE

```
clc;
clear;
D=dir('C:\Users\VMLXB6\Desktop\Test run 1\*.jpg');
num_of_files=numel(D);
stacks=cell(1,numel(D));
Z=zeros(1,num_of_files);
for i=1:numel(D)
   P=imread(D(i).name);
   % P=im2double(P);-------> We are finding the minimum anyways
   % P=rgb2gray(P); -------> Image already in grey scale
   stacks[4]=P;
   A=stacks[4];
   B=A(41,:);
   position = min_funct(B);
   Z(1,i)=position;

end
disp=zeros(1,num_of_files);    % Pre-allocation of memory
time=zeros(1,num_of_files);
disp(1)=0;
time(1)=0;
% first=Z(1,1);

for j=1:num_of_files
   disp(j)= (200-Z(1,j))*0.0258;
   time(j)=(j-1)/60;
end

plot(time,disp,'-')
figure;

[F,X]=FFT(disp,time);

semilogy(F,X)


amplitudes=finding_amplitudes(disp);

sorted_amplitudes=sorting(amplitudes);

total_average = sum(sorted_amplitudes)/length(sorted_amplitudes)

top_10=0.1*length(sorted_amplitudes);

top_20=0.2*length(sorted_amplitudes);

for z=1:top_10
   filter_10(z)=sorted_amplitudes(z);
end

for y=1:top_20
   filter_20(y)=sorted_amplitudes(z);
end


top_10_average = sum(filter_10)/length(filter_10)
```

```
top_20_average = sum(filter_20)/length(filter_20)


%%%%%%%%%%%%%%%%%%%%%%%%%%%%%%%%%%%%%%%%%%%%%%%%%%%%%%%%%%%%%%%%%%%%%%%%%%%%
function [disp]=finding_amplitudes(A)

n=length(A);

if A(1,2) > A(1,1)
   direction=1;      % If direction is 1 then curve starts going up ward
else
   if A(1,2) < A(1,1)
      direction=2;   % If direction is 1 then curve starts going downward
   end
end

p=1;

if direction ==1      % Curve starts Going up from begining
   flag=1;

   for i=2:n-1

      if flag==1    % It is going up

         if A(1,i+1) < A(1,i)
         record(p)=A(1,i);
         p=p+1;
         flag=0;
         end

      end

      if flag==0    % It is going down
         if A(1,i+1) > A(1,i)
            record(p)=A(1,i);
            p=p+1;
            flag=1;
         end
      end
   end

end


if direction ==2      % Curve starts Going Down from beginning
   flag=0;

   for i=2:n-1

      if flag==0    % It is going down

         if A(1,i+1) > A(1,i)
         record(p)=A(1,i);
         p=p+1;
```

```
            flag=1;
            end

        end

        if flag==1    % It is going up
            if A(1,i+1) < A(1,i)
                record(p)=A(1,i);
                p=p+1;
                flag=0;
            end
        end
    end

end


for j=1:length(record)/2

    amplitudes(j)=abs(record(j+1)- record(j))*0.5;
end

disp=amplitudes;

disp;

%%%%%%%%%%%%%%%%%%%%%%%%%%%%%%%%%%%%%%%%%%%%%%%%%%%%%%%%%%%%%%%%%%%%%%%%%%%%
function [F,Y]=FFT(x,t)

dt=1/60; %Time step size

N=length(t);
X=abs(fft(x,N));
for i=1:length(X)/2
    Y(i)=X(i);
end

length(X)
length(Y)

F=[0:(N/2)-1]/(N*dt);

length(F)


%%%%%%%%%%%%%%%%%%%%%%%%%%%%%%%%%%%%%%%%%%%%%%%%%%%%%%%%%%%%%%%%%%%%%%%%%%%%

function [position] = min_funct(x)

n=length(x);

p=x(1);

for i=2:1:n
    if x(i)< p;
        p=x(i);
```

```
        index=i;
    end
end

position=index;

%%%%%%%%%%%%%%%%%%%%%%%%%%%%%%%%%%%%%%%%%%%%%%%%%%%%%%%%%%%%%%%%%%%%%%%
function [sorted]=sorting(amplitudes)

for n=1:length(amplitudes)-1

for k=1:length(amplitudes)-1

    if amplitudes(k)<amplitudes(k+1)

        swap=amplitudes(k+1);
        amplitudes(k+1)=amplitudes(k);
        amplitudes(k)=swap;

    end
end

end

sorted=amplitudes;
```

APPENDIX C.

DAMPING TEST

```
clc;
clear;

D=dir('C:\Users\VMLXB6\Desktop\Test Run 1\Damping Test\*.jpg');
num_of_files=numel(D);
stacks=cell(1,numel(D));
Z=zeros(1,num_of_files);
for i=1:numel(D)
   P=imread(D(i).name);

   stacks[4]=P;
   A=stacks[4];
   B=A(35,:);
   [value,position] = min_funct(B);
   Z(1,i)=position;
   % L(1,i)=value;

end

disp=zeros(1,num_of_files);    % Pre-allocation of memory
time=zeros(1,num_of_files);
disp(1)=0;
time(1)=0;
first=Z(1,1);

for j=1:num_of_files
   disp(j)= (first-Z(1,j))*0.0258;
   time(j)=(j-1)/60;
end
plot(time,disp,'-')

[avg_c, avg_zeta]=damping_const(disp);
%%%%%%%%%%%%%%%%%%%%%%%%%%%%%%%%%%%%%%%%%%%%%%%%%%%%%%%%%%%%%%%%%%%%%%%%%%%%%%%
function [avg_damping,avg_zeta]=damping_const(A)

spring_k = 84.089;
mass = 1.6377;
n=length(A);
for start=1:n
   if A(1,start)~= A(1,start+1)
      break;
   end
end
if A(1,start+1) >= A(1,start)
   direction=1;       % If direction is 1 then curve starts going up ward
else
   if A(1,start+1) < A(1,start)
      direction=2;   % If direction is 2 then curve starts going downward
   end
end
p=1;
if direction ==1      % Curve starts Going up from begining
   flag=1;
   for i=start:n-1
      if flag==1    % It is going up
         if A(1,i+1) < A(1,i)
```

```
            record(p)=A(1,i);
            p=p+1;
            flag=0;
            end
        end
        if flag==0    % It is going down
            if A(1,i+1) > A(1,i)
              record(p)=A(1,i);
              p=p+1;
              flag=1;
            end
        end
    end
end
if direction ==2      % Curve starts Going Down from begining
    flag=0;
    for i=start:n-1
        if flag==0    % It is going down

            if A(1,i+1) > A(1,i)
            record(p)=A(1,i);
            p=p+1;
            flag=1;
            end

        end

        if flag==1    % It is going up
            if A(1,i+1) < A(1,i)
              record(p)=A(1,i);
              p=p+1;
              flag=0;
            end
        end
    end
end
count=1;
for j=1:1:(length(record)-2)
     if record(j)~=0 && record(j+2)~=0
    log_decrement(count) = log(record(j)/record(j+2));
    count=count+1;
     end
end
 zeta=zeros(1,length(log_decrement));
 length(log_decrement);
for k=1:length(log_decrement)

    zeta(k)=log_decrement(k)/sqrt((4*pi*pi)+(log_decrement(k))^2);
    C(k)=2*zeta(k)*sqrt(spring_k*mass);
end
avg_damping=mean(C)
avg_zeta=mean(zeta)


%%%%%%%%%%%%%%%%%%%%%%%%%%%%%%%%%%%%%%%%%%%%%%%%%%%%%%%%%%%%%%%%%%%%%%%%
```

```
function [value,position] = min_funct(x)

n=length(x);

p=x(1);

for i=2:1:n
   if x(i)< p;
      p=x(i);
      index=i;
   end
end

value = p;
position = index;

%%%%%%%%%%%%%%%%%%%%%%%%%%%%%%%%%%%%%%%%%%%%%%%%%%%%%%%%%%%%%%%%%%%%%%%%%%%%
```

APPENDIX D.

RUNGE-KUTTA 4^{th} ORDER NUMERICAL SCHEME

```
#include "cfx5ext.h"
dllexport(RUNGEKUTTA)
C----------------------------START OF MAIN SUBROUTINE-----------------
      SUBROUTINE RUNGEKUTTA (
     &  NLOC, NRET, NARG, RET, ARGS, CRESLT, CZ, DZ, IZ, LZ, RZ)
      implicit none
C     # include"parallel_partitioning.h"
C GLOBAL PARAMETERS
C ARGUMENT LIST
C-----------------------GLOBAL LIST OF VARIABLES--------------
      INTEGER NLOC, NARG,NRET
      CHARACTER CRESLT*(*)
      REAL ARGS(NLOC,NARG),RET(NLOC,NRET)
      INTEGER IZ(*)
      CHARACTER CZ(*)*(1)
      DOUBLE PRECISION DZ(*)
      LOGICAL LZ(*)
      REAL RZ(*)

C EXTERNAL ROUTINES

C LOCAL PARAMETERS & VARIABLES
C INTEGER ILOC,NCLOOP
      REAL DISPLACEMENT, VELOCITY,B,A,acct,blah
      DATA A/0.0/
      REAL Y(2), MASS, K, C,DX,FORCE
C MASS OF THE SYSTEM
      DATA MASS/1.85/
C SPRINF STIFFNESS
      DATA K/65.0/
```

```
C DAMPING CONSTANT
      DATA C/0.0175/
      INTEGER I


C.....STACK POINTERS-----------------------------
C.....INITIALIZE RET() TO ZERO--------------------
C      CALL SET_A_0(RET,NLOC*NRET)
C-------------------------INPUT FROM CFX-------------------------
C
C TIME STEP
      DX = ARGS(1,1)
C Lift FORCE
      FORCE = ARGS(1,2)
C Accumulated time step
      acct = ARGS(1,3)
      OPEN(9, FILE='test.TXT', ACTION='WRITE',
     &  STATUS='UNKNOWN', position='REWIND')
      WRITE(9,*) acct
      CLOSE(9)
      IF(acct.EQ.1)THEN
      Y(1) = 0.0;
      OPEN(7, FILE='displacement.TXT', ACTION='WRITE', STATUS='UNKNOWN')
      WRITE(7,*) Y(1)
      CLOSE(7)
      Y(2) = 0.0;
      OPEN(8, FILE='velocity.TXT',ACTION='WRITE', STATUS='UNKNOWN')
      WRITE(8,*) Y(2)
      CLOSE(8)
      OPEN(9, FILE='acct.TXT', ACTION='WRITE',
     &  STATUS='UNKNOWN', position='REWIND')
```

```
      WRITE(9,*) acct
      CLOSE(9)
      blah=0.0
      ELSE IF(acct.GE.1)THEN
      OPEN(7, FILE='displacement.TXT',ACTION='READ',STATUS='UNKNOWN')
      READ(7,*) Y(1)
      CLOSE(7)
      OPEN(8, FILE='velocity.TXT', ACTION='READ', STATUS='UNKNOWN')
      READ(8,*) Y(2)
      CLOSE(8)
      OPEN(9, FILE='acct.TXT', ACTION='READ',
     &  STATUS='UNKNOWN', position='REWIND')
      READ(9,*) blah
      CLOSE(9)
      ENDIF
C-----------------------CALLING SUBROUTINE RK4--------------------
      IF(blah.ne.acct)then
        CALL RK4(Y,DX,MASS,K,C,FORCE)
        OPEN(9, FILE='acct.TXT',ACTION='WRITE', STATUS='UNKNOWN',
     &      position='rewind')
        WRITE(9,*) acct
        CLOSE(9)
      endif
      DO I=1,NLOC
      RET(I,1)=Y(1)
      END DO
C-----------------------END OF MAIN SUBROUTINE--------------------
      END SUBROUTINE RUNGEKUTTA
C-----------------------CALLING FUNCTION F1-----------------------
      REAL FUNCTION F1(XT,DISP1,VEL1)
```

```
      IMPLICIT NONE
      REAL XT, DISP1, VEL1, RET
      F1 = VEL1
      RETURN
      END FUNCTION F1
C-----------------------CALLING FUNCTION F2----------------------
      REAL FUNCTION F2(XTT,DISP2,VEL2,K, MASS,C,FORCE)
      IMPLICIT NONE
      REAL XTT, DISP2, VEL2, K, MASS,C,FORCE
      F2 = -(K/MASS)*DISP2 + (FORCE)/MASS - (C/MASS)*VEL2
      RETURN
      END FUNCTION F2
C
C---------------------------SUBROUTINE RK4--------------------------
      SUBROUTINE RK4(Y,DX,MASS,K,C,FORCE)
      IMPLICIT NONE
C     INTEGER I
      REAL Y(2),X,DX,XH,Y1,Y2,DY1,DY2,
     &     DY10,DY20,DY11,DY21,DY12,DY22,DY13,DY23,VALUE,FORCE
      REAL K,C, MASS, F1, F2
C     DX = (B-A)/N
      X= 0.0
C     DO 1 I = 0,N-1
      XH = X+.5*DX
      Y1 = Y(1)
      Y2 = Y(2)
      DY10 = F1(X,Y1,Y2)*DX
      DY20 = F2(X,Y1,Y2,K,MASS,C,FORCE)*DX
      DY11 = F1(XH,Y1+.5*DY10,Y2+.5*DY20)*DX
      DY21 = F2(XH,Y1+.5*DY10,Y2+.5*DY20,K,MASS,C,FORCE)*DX
```

```
      DY12 = F1(XH,Y1+.5*DY11,Y2+.5*DY21)*DX
      DY22 = F2(XH,Y1+.5*DY11,Y2+.5*DY21,K,MASS,C,FORCE)*DX
      DY13 = F1(X+DX,Y1+DY12,Y2+DY22)*DX
      DY23 = F2(X+DX,Y1+DY12,Y2+DY22,K,MASS,C,FORCE)*DX
      DY1 = (DY10 + 2.*DY11 + 2.*DY12 + DY13)/6.
      DY2 = (DY20 + 2.*DY21 + 2.*DY22 + DY23)/6.
C
C.................Y(1) = DISPLACEMENTS.....................................
C
      Y(1) = Y(1) + DY1
      OPEN(9, FILE='test.TXT', ACTION='WRITE',
     &  STATUS='UNKNOWN', position='append')
      OPEN(7,FILE = 'displacement.TXT', ACTION = 'WRITE',
     &   POSITION='REWIND', STATUS ='UNKNOWN')
      WRITE(7,*) Y(1)
      CLOSE(7)
      Y(2) = Y(2) + DY2
      OPEN(8, FILE = 'velocity.TXT', ACTION = 'WRITE',
     &   POSITION='REWIND', STATUS ='UNKNOWN')
      WRITE(8,*) Y(2)
      WRITE(9,*) Y(1),' ',Y(2)
      CLOSE(8)
      close(9)
C--------------------------END OF SUBROUTINE RK4--------------------
      END SUBROUTINE RK4
```

BIBLIOGRAPHY

[1] R. Tol, "Estimates of the damage costs of climate change: Benchmark Estimates," *Environmental and Resource Economics*, vol. 21, pp. 47-73.

[2] S. Fankhauser and R. Tol, "The social costs of climate change: The IPCC second assessment report and beyond," *Springer*, vol. vol (1), pp. 385-403.

[3] R. Newell, "Annual Energy Outlook 2010 Reference Case," *The Paul H.Nitze School of Advanced International Studies, Washington, D.C*.

[4] "US Bureau of the Census (USBC). ," *Statistical Abstract of the United States.US government*.

[5] Shaifee and Topal, "When will fossil fuel reserves be diminished," *Energy Policy*, vol. 37, pp. 181-189.

[6] S. Meninger, J. O. Mur-Miranda, R. Amirtharajah, A. Chandrakasan, and J. Lang, "Vibration-to-electric energy conversion," *IEEE Transactions on Very Large Scale Integration (VLSI) Systems*, vol. 9, pp. 64-76, Feb. 2001.

[7] R. Bedard, "Overview of Wave and Current Energy:," *Resource, Technology, Environmental and Business Issues*.

[8] http://www.usbr.gov/lc/hooverdam, "US Gov hoover dam," November 2011.

[9] http://www.energetech.com/, "Oscillating Water Column," 2011.

[10] http://ocsenergy.anl.gov/, "Oscillating Water Column," November 2011.

[11] http://www.pelamiswave.com/. "Pelamis Wave Energy," 2011.

[12] http://www.oceanpowertechnologies.com/, "Ocean Power Technologies," November 2011.

[13] http://www.physics-edu.org/tech/ocean_wave_power_plants.htm., "Wave Energy Power Plants," November 2011.

[14] A. S. Bahaj, "Experimental verification of numerical predictions for the hydrodynamic performance of horizontal axis marine current turbines," *Renewable Energy*, vol. 32, pp. 2479-2490.

[15] "Proceedings of the Hydrokinetic and Wave Energy technologies technical and environmental issues workshop."

[16] "Marine turbine," accessed on November 2011,

[17] R. H. J. Willden and J. M. R. Graham, "Numerical prediction of VIV on long flexible circular cylinders," *Journal of Fluids and Structures*, vol. 15, pp. 659-669.

[18] M. Bernitsas and K. Raghavan, "VIVACE (Vortex Induced Vibration for Aquatic Clean Energy): A New concept in generation of clean and renewable energy from fluid flow," *Proceedings of OMAE2006, 25th International OMAE Conference*.

[19] M. Bernitsas and K. Raghavan, "Converter of Current/Tide/Wave Energy," U.S. Patent 60/628,252,

[20] M. Bernitsas and K. Raghavan, "Fluid motion energy converter," U.S. Patent

[21] M. Bernitsas and K. Raghavan, "VIVACE(Vortex Induced Vibration Aquatic Clean Energy): A New Concept in Generation of Clean and Renewable Energy from Fluid Flow," *Journal of Offshore Mechanics and Arctic Engineering*.

[22] "Vortex Hydro Energy," accessed on 2011,

[23] P. Anagnostopoulos and P. W. Bearman, "Response Characteristics Of a Vortex-Excited Cylinder at Low Reynolds Numbers," *Journal of Fluids and Structures*, vol. 6, pp. 39-50.

[24] D. Shiels, A. Leonard, and A. Roshko, "Flow-Induced Vibrations of a Circular Cylinder At Limiting Structural Parameters," *Journal of Fluids and Structures*, vol. 15, pp. 3-21.

[25] A. Placzek, J. Sigrist, and A. Hamdouni, "Numerical simulation of an oscillating cylinder in a cross-flow at low Reynolds number: forced and free oscillations," *Computers and Fluids*, vol. 38, pp. 80-100.

[26] T. Sarpkaya, "Vortex-induced oscillations. A selective review," *ASME Journal of Applied Mechanics*, vol. 46.

[27] O. M. Griffin and S. E. Ramberg, "Some recent studies of vortex shedding with application to marine tubulars and risers," *ASME Journal of Energy Resources Technology*, vol. 104.

[28] P. W. Bearman, "Vortex shedding from oscillating bluff bodies," *Annual Review of Fluid Mechanics*, vol. 16.

[29] G. V. Parkinson, "Phenomena and modeling of flow-induced vibrations of bluff bodies," *Progress in Aerospace Science*, vol. 26.

[30] C. H. K. Williamson and R. Govardhan, "Vortex-induced vibrations," *Annual Review of Fluid Mechanics*, vol. 36.

[31] J. H. Lienhard, "Synopsis of Lift ,Drag and Vortex Frequency Data for Rigid Circular Cylinders," *Washington State University, College of Engineering, Research Division Bulletin 300*.

[32] C. H. K. Williamson, "2-D and 3-D aspect of the wake of a cylinder, and their relation to wake computations,," *Lectures in Applied Mathematics,*, vol. 28, pp. 719-751.

[33] C. Norberg, "Flow around a circular cylinder: Aspects of fluctuating lift," *Journal of Fluids and Structures*, vol. 15, pp. 459-469.

[34] C. H. K. Williamson and A. Roshko, "Vortex formation in the wake of an oscillating cylinder," *Journal of Fluids and Structures*, vol. 2, pp. 355-381, July 1988.

[35] A. Khalak and C. H. K. Williamson, "Motions, forces and mode transitions in vortex-induced vibrations at low mass-damping," *Journal of Fluids and Structures*, vol. 13, pp. 813-851, October 1999.

[36] Leonard A and R. A., "Aspects of flow induced vibrations," *Journal of Fluids and Structures*, vol. 15, pp. 415-25.

[37] D. Shiels, A. Leonard, and A. Roshko, "Flow induced vibration of a circular cylinder at limiting structural parameters," *Journal of Fluids and Structures*, vol. 15, pp. 3-21.

[38] J. T. Klamo, A. Leonard, and A. Roshko, "On the maximum amplitude for a freely vibrating cylinder in cross-flow," *Journal of Fluids and Structures*, vol. 21, pp. 429-434, 2005.

[39] J. Klamo, A. Leonard, and A. Roshko, "The effects of damping on the amplitude and frequency response of a freely vibrating cylinder in cross-flow," *Journal of Fluids and Structures*, vol. 22, pp. 845-856.

[40] G. V. Parkinson, "Phenomena and modelling of flow-induced vibrations of bluff bodies," *Progress in Aerospace Science*, vol. 26, pp. 169-224.

[41] C. C. Feng, "The measurement of vortex induced effects in flow past stationary and oscillating circular and D-section cylinders," Masters Thesis, University of British Columbia, 1968.

[42] A. Khalak and C. H. K. Williamson, "Investigation of relative effects of mass and damping in vortex-induced vibration of a circular cylinder," *Journal of Wind Engineering and Industrial Aerodynamics*, vol. 69-71, pp. 341-350, July-Oct. 1997.

[43] A. Khalak and C. H. K. Williamson, "Dynamics of a Hydroelastic Cylinder with Very Low Mass and Damping," *Journal of Fluids and Structures*, vol. 10, pp. 455-472, July 1996.

[44] A. Khalak and C. H. K. Williamson, "Fluid forces and dynamics of a hydroelastic structure with very low mass and damping," *Journal of Fluids and Structures*, vol. 11, pp. 973-982, November 1997.

[45] D. Brika and A. Laneville, "Vortex-induced vibrations of a long flexible circular cylinder," *Journal of Fluid Mechanics*, vol. 250, pp. 481-508, May 1993.

[46] D. Brika and A. Laneville, "An experimental study of the aeolian vibrations of a flexible circular cylinder at different incidences," *Journal of Fluids and Structures*, vol. 9, pp. 371-91.

[47] C. Scruton, "On the wind-excited oscillations of stacks, towers and masts," *Proceedings Symposium on Wind Effects on Buildings and Structures*, pp. 798-836.

[48] B. J. Vickery and R. D. Watkins, "Flow-induced vibrations of cylindrical structures," In: Proceedings 1st Australian Conference on Hydraulics and Fluid Mechanics," pp. 213-241.

[49] J. D. Smith, "An experimental study of the aeroelastic instability of rectangular cylinders," Thesis, University of British Columbia 1962.

[50] R. E. D. Bishop and A. Y. Hassan, "The lift and drag forces on a circular cylinder oscillating in a flowing fluid," *Proceedings of the Royal Society of London*, vol. Series A 277, pp. 51-75.

[51] T. Sarpkaya, "A critical review of the intrinsic nature of vortex-induced vibrations," *Journal of Fluids and Structures*, vol. 19, pp. 389-447.

[52] G. H. Koopmann, "The vortex wakes of vibrating cylinders at low Reynolds numbers," *Journal of Fluid Mechanics*, vol. 28, pp. 501-512.

[53] O. M. Griffin, "The unsteady wake of an oscillating cylinder at low Reynolds number," *ASME Journal of Applied Mechanics*, vol. 38, pp. 729-738.

[54] T. L. Morse and C. H. K. Williamson, "Employing controlled vibrations to predict fluid forces on a cylinder undergoing vortex-induced vibration," *Journal of Fluids and Structures*, vol. 22, pp. 877-884.

[55] T. L. Morse and C. H. K. Williamson, "Prediction of vortex-induced vibration response by employing controlled motion," *Journal of Fluid Mechanics*, vol. 634, pp. 5-39.

[56] T. L. Morse and C. H. K. Williamson, "Steady, unsteady and transient vortex-induced vibration predicted using controlled motion data," *Journal of Fluid Mechanics*, vol. 649.

[57] R. Govardhan and C. H. K. Williamson, "Resonance forever: existence of a critical mass and an infinite regime of resonance in vortex-induced vibration," *Journal of Fluid Mechanics*, vol. 473, pp. 147-166, 2002.

[58] R. Govardhan and C. H. K. Williamson, "Critical mass in vortex-induced vibration of a cylinder," *European Journal of Mechanics - B/Fluids*, vol. 23, pp. 17-27, 2003.

[59] R. Govardhan and C. H. K. Williamson, "Modes of Vortex formation and frequency response of a freely vibrating cylinder," *Journal of Fluid Mechanics*, vol. 420, pp. 85-130.

[60] T. L. Morse and C. H. K. Williamson, "The effect of Reynolds number on the critical mass phenomenon in vortex-induced vibration," *PHYSICS OF FLUIDS*, vol. 21.

[61] R. Govardhan and C. H. K. Williamson, "Vortex induced vibration of an elastically-mounted sphere," *Journal of Fluid Mechanics*.

[62] F. Flemming and C. H. K. Williamson, ""Vortex induced vibrations of a pivoted cylinder,"" *Journal of Fluid Mechanics*.

[63] R. Govardhan and C. H. K. Williamson, "The effects of two degrees of freedom on vortex-induced vibration," *Journal of Fluid Mechanics*.

[64] Z. Y. Pan, W. C. Cui, and Q. M. Miao, "Numerical simulation of vortex-induced vibration of a circular cylinder at low mass-damping using RANS code," *Journal of Fluids and Structures*, vol. 23, pp. 23-37.

[65] C. Y. Zhou, R. M. C. So , and K. Lam, "Vortex Induced Vibration of an elastic circular cylinder," *Journal of Fluids and Structures*, vol. 13, pp. 165-189.

[66] P. Anagnostopoulos, "Numerical investigation of response and wake characteristics of a vortex excited cylinder in a uniform stream," *Journal of Fluids and Structures*, vol. 8, pp. 367-390.

[67] P. Anagnostopoulos, "Numerical study of flow past a circular excited transversely to the excited stream. Part 1: Lock in zone, Hydroynamic forces and wake geometry," *Journal of Fluids and Structures*, vol. 14, pp. 819-851.

[68] T. K. Prasanth and S. Mittal, "Vortex-induced vibrations of a circular cylinder at low Reynolds numbers," *Journal of Fluid Mechanics*, vol. 594, pp. 463-491.

[69] T. Li, J. Y. Zhang, W. H. Zhang, and M. H. Zhu, "Vortex-Induced Vibration Characteristics of an Elastic Circular Cylinder," *World Academy of Science, Engineering and Technology*, vol. 60, pp. 56-65.

[70] F. L. Ponta and H. Aref, "Numerical experiments on vortex shedding from an oscillating cylinder," *Journal of Fluids and Structures*, vol. 22, pp. 327-344.

[71] E. Guilmineau and P. Queutey, "Numerical simulation of vortex-induced vibration of a circular cylinder with low mass-damping in a turbulent flow," *Journal of Fluids and Structures*, vol. 19, pp. 449-466.

[72] H. Al-Jamal and C. C. Dalton, "Vortex induced vibrations using Large Eddy Simulation at a moderate Reynolds number," *Journal of Fluids and Structures*, vol. 19, pp. 73-92.

[73] M. Tutar and Holdo, "Large Eddy Simulation of a smooth circular cylinder oscillating normal to a uniform flow," *ASME Journal of Fluids Engineering*, vol. 122, pp. 694-702.

[74] H. M. Blackburn and G. E. Karniadakis, "Two- and Three-Dimensional Simulations of Vortex-Induced Vibration of a Circular Cylinder," *Presented at the 3rd Int. Offshore & Polar Engng Conf., Singapore*, vol. 3, pp. 715-720.

[75] H. M. Blackburn, R. Govardhan, and C. H. K. Williamson, "A complementary numerical and physical investigation of vortex induced vibration," *Journal of Fluids and Structures*, vol. 15, pp. 481-488.

[76] D. J. Newman and G. E. Karniadakis, "A direct numerical simulation study of flow past a freely vibrating cable," *Journal of Fluid Mechanics*, vol. 344, pp. 95-136.

[77] D. Lucor, J. Foo, and G. E. Karniadakis, "Vortex mode selection of a rigid cylinder subject to VIV at low mass-damping," *Journal of Fluids and Structures*, vol. 20, pp. 483-503.

[78] D. C. Wilcox, "Turbulence modeling for CFD," *DCW Industries*.

[79] F. R. Menter, "Two-equation eddy-viscosity turbulence models for attached and separated adverse pressure gradient flows," *American Institute of Aeronautics and Astronautics*, vol. 32, pp. 1598-1605.

[80] ANSYS, "CFX 12.0.1 User's guide," ANSYS INC., 2010.

[81] "" ANSYS-CFX 12.0: Theory Guide"," 2009.

[82] H. K. Versteeg and W. Malalasekera *An introduction to Computational Fluid Dynamics: The Finite Volume Method*: Harlow, Essex, England : Longman Scientific & Technical ; New York : Wiley, 1995., 1995.

[83] A. Placzek, J. F. Sigrist, and A. Hamdouni, "Numerical simulation of an oscillating cylinder in a cross-flow at low Reynolds number: Forced and free oscillations," *Computers and Fluids*, vol. 38, pp. 80-100.

[84] H. Persillon and M. Braza, "Physical analysis of the transition to turbulence in the wake of a circular cylinder b three-dimentional Navier-Stokes simulation.," *Journal of Fluid Mechanics*, vol. 365, pp. 23-88.

[85] A. Roshko, "On the development of turbulent wakes from vortex streets," California Institute of Technology.

[86] C. Norberg, "Fluctuating lift on a circular cylinder: review and new measurements," *Journal of Fluids & Structures*, vol. 17(1), pp. 57-96.

[87] U. Fey, M. Konig, and H. Eckelmann, "A new Strouhal-Reynolds-number relationship for the circular cylinder in the range $47<Re<20x10^5$," *Phys Fluids*, vol. 10(7), pp. 1547-9.

[88] J.-F. S. Antoine Placzek, Aziz Hamdouni, ""Numerical simulation of an oscillating cylinder in a cross-flow at low Reynolds number: Forced and free oscillations,"" *Computers & Fluids*, vol. 38, pp. 80-100.

[89] P. Anagnostopoulos and P. W. Bearman, "Response characteristic of a vortex excited cylinder at low Reynolds numbers," *Journal of Fluids & Structures*, vol. 6, pp. 39-50.

[90] T. L. Morse, R. N. Govardhan, and C. H. K. Williamson, "The effect of end conditions on the vortex-induced vibration of cylinders," *Journal of Fluids & Structures*, vol. 24, pp. 1227-1239.

[91] N. Bianchi, S. Bolognani, D. Dalla Corte, and F. Tonel, "Tubular linear permanent magnet motors: an overall comparison," *IEEE Transactions on Industry Applications*, vol. 39, pp. 466-475.

[92] P. Hew Wooi, H. Arof, and Wijono, "Design of a permanent magnet linear generator," *Proc. Strategic Technology, The first International Forum*, pp. 231-234.

[93] L. Szabo, C. Oprea, A. Viorel, and K. A. Biro, "Novel Permanent Magnet Tubular Linear Generator for Wave Energy Converters," *Proc. Electric Machines and Drives Conference,IEEE International*, vol. 2, pp. 983-987.

[94] N. J. Baker, M. A. Mueller, and E. Spooner, "Permanent Magnet air-cored tubular linear generator for marine energy converters," *Proc. Electric Machines and Drives Conference,*, vol. 2.

[95] L. Cheng-Tsung and L. Hsin-Nan, "Development of a schematic scheme for direct driven slotless tubulat linear generator design," *Proc. Power electronics and drive systems,*.

[96] Y. Tan and S. Panda, "Optimized wind energy harvesting system using resistance emulator and active rectifier for wireless sensor nodes," *IEEE Transactions on Power Electronics*, pp. 1-1.

[97] T. Esram and P. L. Chapman, "Comparison of Photovoltaic array maximum power point tracking techniques," *IEEE Transactions on Energy Conversions*, vol. 22, pp. 439-449.

VITA

Varun Michael Lobo was born in Bombay (Mumbai) on the July 3, 1986. He received his bachelors in Mechanical Engineering from the University of Mumbai in 2008. He joined the Process Equipment Division (PED) at Godrej and Boyce, Mumbai as a graduate trainee engineer in 2008. He joined Missouri University of Science and Technology (Missouri S&T) (formerly known as University of Missouri, Rolla) in August 2009 and joined the Hydrodynamics Laboratory at Missouri S&T in 2010. He graduated with a Master's Degree in Mechanical Engineering in August 2012.

Varun Lobo has published two conference papers, at the IEEE Green Technologies Conference (2011) where he won a best paper award and the other at American Society of Mechanical Engineers (ASME) Environmental Sustainability and Fuel Cell Technology conference (2011). He has been an ASME member since 2010.